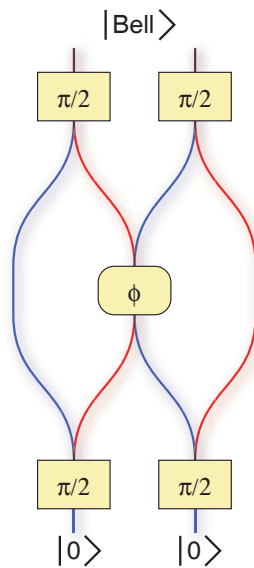# Entanglement with quantum gates in an optical lattice

Olaf Mandel

Dissertation der Fakultät für Physik
der
Ludwig-Maximilians-Universität München

$|\text{Bell}\rangle$

| $\pi/2$ | $\pi/2$ |

ϕ

| $\pi/2$ | $\pi/2$ |

$|0\rangle$ $|0\rangle$

Munich, February 2005

1ˢᵗ reviewer: Prof. Theodor W. Hänsch
2ⁿᵈ reviewer: Prof. Khaled Karrai

Viva-voce on April 22ⁿᵈ, 2005

Version of April 26ᵗʰ 2005, for archiving in the library of the Ludwig-Maximilians-Universität München.

Zusammenfassung

Das Konzept eines „Quantencomputers" hat in den letzten Jahren viel Aufmerksamkeit errungen. Viele Forschungsgruppen weltweit befassen sich mit den außergewöhnlichen Möglichkeiten von Quantencomputern und mit ihrer Realisierung. Aktuelle Grundlagenexperimente arbeiten an den einzelnen Bausteinen eines solchen Rechners.

Den Anfang nahm das Konzept, quantenmechanische Systeme zur Berechnung komplexer Probleme zu verwenden, 1982 mit Feynmans Vorschlag des Quantensimulators. Dieser stellt ein gut kontrollierbares System aus miteinander wechselwirkenden Quantensystemen dar. Das Ziel ist es, ein im Labor nicht beherrschbares Ziel-System auf den Quantensimulator abzubilden. Aus dem Verhalten des Quantensimulators läßt sich dann auf das Verhalten des Ziel-Systems schließen. Eine quantenmechanische Messung am Quantensimulator ist somit vergleichbar zu dem Durchlauf einer numerischen Simulation des Ziel-Systems. Der entscheidende Unterschied besteht darin, dass eine numerische Simulation häufig nur unter sehr starken Vereinfachungen durchführbar ist, die dann die praktische Bedeutung des Ergebnisses in Frage stellen. Nur sehr kleine Quantensysteme können ohne Vereinfachungen auf heutigen Computern berechnet werden.

In dieser Arbeit wird ein System bestehend aus einzelnen Grundzustands-Atomen vorgestellt, das in einem drei-dimensionalen optischen Gitter gespeichert ist. Dabei ist jedes der bis zu 100.000 Atome in einem eigenen Potentialminimum gefangen, isoliert von den anderen Atomen. Dieser Zustand bildet einen hervorragenden Ausgangspunkt für die Realisierung eines Quantensimulators: jedes Atom wird als Informationsträger für ein Spin-$\frac{1}{2}$ System betrachtet. Kaum ein anderes der momentan untersuchten Konzepte hat so viele Informationsträger wie ein Mott-Isolator Zustand in einem optischen Gitter. Wir haben in Vorexperimenten bereits hohe Speicherzeiten und gute Kohärenzzeiten nachgewiesen.

Hier wird dieses System nun um eine wesentliche Grundvoraussetzung für einen Quantensimulator erweitert: man benötigt genau kontrollierbare Wechselwirkungen zwischen den einzelnen Atomen, um die Wechselwirkungs-Terme des Ziel-Systems modellieren zu können. Diese
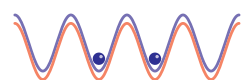
Wechselwirkungen werden im optischen Gitter durch zustandsselektive Fallen-Potentiale realisiert. Wenn die Zustände eines Atoms als $|0\rangle$ und $|1\rangle$ bezeichnet werden, dann gibt es zwei unterschiedliche Potentiale V_0 und V_1, die jeweils nur auf einen der Zustände wirken. Diese beiden Potentiale werden gegeneinander verschoben und erlauben es so, benachbarte Atome miteinander in Wechselwirkung zu bringen.

Da das Verschieben immer entlang einer der drei Gitterachsen stattfindet, ist auch die Wechselwirkung nicht auf ein Atom-Paar beschränkt, sondern alle in einer Gitterachse benachbarten Atom-Paare treten miteinander in Wechselwirkung. Diese inhärente Parallelität hat es uns erlaubt, in nur einer Operation Verschränkung in großen Systemen zu erzeugen. Die Verschränkung wurde mit einem Ramsey-Interferometer gemessen. Eine Sequenz aus einer Wechselwirkung zwischen nächsten Nachbarn erzeugt den Cluster-Zustand, einen maximal verschränktern Zustand.

Neuere Veröffentlichungen schlagen vor, den Cluster-Zustand als Basis für eine neue Art Quantencomputer zu nutzen. Im Gegensatz zu unseren heutigen Computern wäre dieser Quantencomputer keine Touring-Maschine, bei der ausschliesslich die Programmierung die Arbeitsweise bestimmt. Stattdessen müsste die Verschaltung der Quanten-Gates geändert werden, um ein neues Problem zu lösen. Dies ist entfernt vergleichbar zu heutigen FPGAs (Field Programmable Gate Arrays — Frei programmierbare Logikbausteine). Bis diese Quantencomputer gebaut werden dürften zwar noch einige weitere Verbesserungen an der Experiment-Technik notwendig sein, aber die ersten Quantensimulatoren sind jetzt in greifbare Nähe gerückt.

Abstract

The concept of a "quantum computer" has attracted much attention in recent years. Many research groups around the world are studying the extraordinary potential of quantum computers and attempting their realisation. Current fundamental experiments are directed towards the individual building blocks of such a computer.

The concept of using quantum mechanical systems to calculate complex problems was created in 1982 with Feynmans proposal of the quantum simulator. This concept represents a well controlled framework of interacting quantum systems. The intention is to map a different system of interest not mastered in the lab onto the quantum simulator. From the behaviour of the quantum simulator the behaviour of the system of interest can be deduced. A quantum mechanical measurement on the quantum simulator is thus comparable to one run of a numerical simulation of the system of interest. The difference is that a numerical simulation can often only be run under severe simplifications that then challenge the practical relevance of the result. Only very small quantum systems can be calculated on today's computers without simplifications.

In this work a system of ground state atoms stored in a 3D optical lattice is presented. Each of the up to 100,000 atoms is stored in its own potential minimum, isolated from the other atoms. This state is a formidable starting point for the realisation of a quantum simulator: every atom is considered the information carrier of a spin-$\frac{1}{2}$ system. Only very few of the other concepts currently under investigation have as many information carriers as a Mott-Insulator state in an optical lattice. We have already shown in preparatory experiments a long storage time and good coherence times.

Here this system is extended by a major prerequisite for a quantum simulator: controllable interactions between individual atoms are essential in order to model the interaction terms of the system of interest. These interactions are realised by a state-selective in the optical lattice by state-selective trapping potentials. If the states of an atom are called $|0\rangle$ and $|1\rangle$, then there are two distinct potentials V_0 and V_1 that each act on only one of the states. The two potentials are shifted with respect to each other
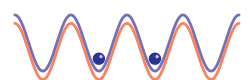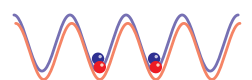
and thus allow bringing neighbouring atoms into contact.

Since the shifting is always performed along one of the three lattice axes, the interaction is not confined to a single pair of atoms, but all pairs of neighbouring atoms along a lattice axis interact. This inherent parallelism has allowed us to create entanglement in large systems in just a single operation. The entanglement has then been measured in a Ramsey interferometer. A sequence of one nearest-neighbour interaction produces the cluster state, a maximally entangled state.

More recent proposals suggest to use a cluster state as the basis for a new kind of quantum computer. As opposed to today's computers, this quantum computer would not be a Touring machine whose working algorithm is only controlled by programming. Instead the wiring of the quantum gates would have to be changed in order to solve a new problem. This is loosely comparable to today's FPGA (Field Programmable Gate Arrays — programmable logic chips). Until these quantum computers are built, quite some improvements on the experimental techniques will be necessary. But the first quantum simulators are now practically within reach.

Contents

1. Introduction

In classical mechanics, the description of n particles scales linearly with n. But in quantum mechanics, the problem grows exponentially, for a set of n spin-$\frac{1}{2}$ particles this would be 2^n variables for the description of the spin alone. This makes numerical simulation of many problems of solid-state-physics, statistical-physics or many-particle-physics, like the Ising or the Heisenberg interactions [1], challenging at best, impossible at worst.

In 1982, Feynman suggested to simulate such complex quantum systems by means of a simpler, experimentally manageable quantum system which he called a *quantum simulator* [2, 3]. This system would have to be very well controlled, so that the measurement result could be taken as an approximation to the result of a calculation. The idea was abstracted to the well known *quantum computer* [4–6], which many groups around the world have since worked on realizing. This work though, presents a system that is well suited to be extended into a quantum simulator. And some simple operations have already been performed with it.

Regular array of qubits

We use ultracold ^{87}Rb atoms to represent one spin. This spin can be any superposition of the two base states $|0\rangle$ and $|1\rangle$ and is called a qubit, translating the dual system with its bit into quantum language. We need to exactly know the quantum state of the single atoms, and we have to ensure that the system does not evolve into an unwanted state. Therefore, each atom is prepared in the lowest energy state, an exactly known state that it cannot leave without external excitation. For an atom cloud, this state is identical to a Bose-Einstein-Condensate (BEC) in which all atoms occupy the same wave function.

We store the qubits in a potential that is a three-dimensional regular lattice of traps. For moderate potential strength, there is tunnel coupling between neighbouring lattice sites and the groundstate of the system is a Superfluid (SF). For strong lattice potentials, the tunnel coupling is reduced and collisions between two atoms stored in the same lattice site become dominant. The ground state in this situation is a Mott-Insulator (MI) with integer atom numbers at each lattice site [7]. In our setup, exactly one atom occupies each position in the lattice.
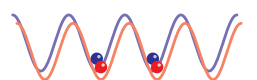
While the qubits are very well stored in such a system and can be easily initialized to any one desired qubit-value, there is more to a quantum simulator: there has to be a controlled spin-dependent interaction between individual qubits. This is needed to simulate the non-local terms in a Hamiltonian or to produce entanglement in the system.

Spin-Dependant Lattices

The lattice potential is formed by a dipole trap, where intensity maxima in an interference pattern in the light field form the lattice sites. When the phase of the interference pattern changes, the intensity maxima move in space, dragging the stored atoms with them. Such a simple approach would not allow to bring neighbouring atoms into contact, as that neighbour is also moved in the same direction.

In our experiment, we have therefore exchanged the simple optical lattice in one axis with a spin-dependent one [8, 9]. It consists of two overlapping interference patterns that can be shifted with respect to each other. The correct choice of wavelength and polarisation makes each of the two lattices couple to a different state of ^{87}Rb. So a qubit $|1\rangle$ can be moved through a lattice of $|0\rangle$ qubits (and vice versa), by phase-shifting the two interference pattern.

But what happens, if the atom is not in the states $|0\rangle$ or $|1\rangle$ but rather in a superposition of those? Let the interference pattern coincide during the creation of the superposition. Then separate the traps for the two states from each other (see fig. 1.1). This delocalises the atom from the initial lattice site i over the two final lattice sites $f1$ and $f2$:

$$|0\rangle_i \rightarrow \frac{1}{\sqrt{2}}(|0\rangle_i + |1\rangle_i) \rightarrow \frac{1}{\sqrt{2}}(|0\rangle_{f1} + |1\rangle_{f2}) \tag{1.1}$$
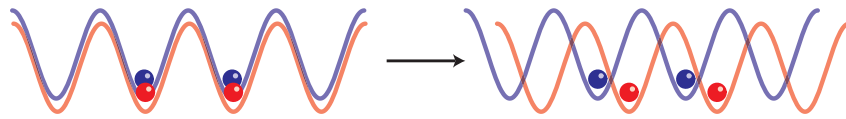
Figure 1.1.: Delocalisation of two atoms. Each atom is in a superposition of $|0\rangle$ (blue) and $|1\rangle$ (red), illustrated as separate spheres. When the spin-dependent traps are separated, the atom becomes delocalised over the two potentials, depending on the atomic state.

Quantum Gates in Lattices

With this shifting approach, it is possible to bring parts of two neighbouring atoms into a common lattice site by moving the spin-dependent potentials relative to each other over one lattice-distance [9]. As there are two atoms in one lattice site, this term of the expanded state has a different energy than the others, leading to a phase-evolution ϕ proportional to the hold time in this common lattice site:

$$
\frac{1}{2}(|0\rangle_i + |1\rangle_{i+1}) \times (|0\rangle_i + |1\rangle_{i+1})
$$
$$
\rightarrow \frac{1}{2}(|0\rangle_i + |1\rangle_{i+1}) \times (|0\rangle_{i+1} + |1\rangle_{i+2})
$$
$$
\rightarrow \frac{1}{2}(|0\rangle_i|0\rangle_{i+1} + |0\rangle_i|1\rangle_{i+2} + e^{-i\phi}|1\rangle_{i+1}|0\rangle_{i+1} + |1\rangle_{i+1}|1\rangle_{i+2}) \qquad (1.2)
$$

This process can be extended to be a trapped atom interferometer as shown in fig. 1.2 on the next page, which is read from the bottom to the top. The position along the shifting-direction is plotted horizontally. Each thick line represents a single atom state in its trapping lattice site. The colour blue (red) of this line encodes the state $|0\rangle$ ($|1\rangle$). Rectangular boxes represent $\pi/2$ microwave pulses that are used to split each atom into two states. The collisional phase shift is shown by oval boxes. Many atoms in parallel are split into two path, are separated in the interferometer and allowed to pick up a phase ϕ. Later, the interferometer-paths join again, and another $\pi/2$-pulse symmetrizes the state. This same sequence is illustrated as an animation in the lower-right corner of every page. The state leaving the interferometer can be examined using a Ramsey sequence.

What makes this atom interferometer special is the kind of interaction happening on the delocalised state of the atoms. The acquired collisional phase ϕ is dependent on more than one particle. It therefore allows to transmit information on the state of spin i to its neighbour spin $i + 1$. This conditional interaction causes the state leaving the interferometer sequence to be maximally entangled for certain values of ϕ. An entangled state will behave differently than a product state in an interferometer: the atom number measured in any given state is always half the total atom number, independent of the alignment of the interferometer. For the product state, the measurement result depends on the alignment of the interferometer.

For two (three) neighbouring atoms, this sequence will generate the famous Bell state (Greenberger-Horne-Zeilinger (GHZ) state) [10]. For
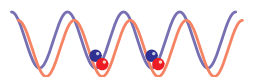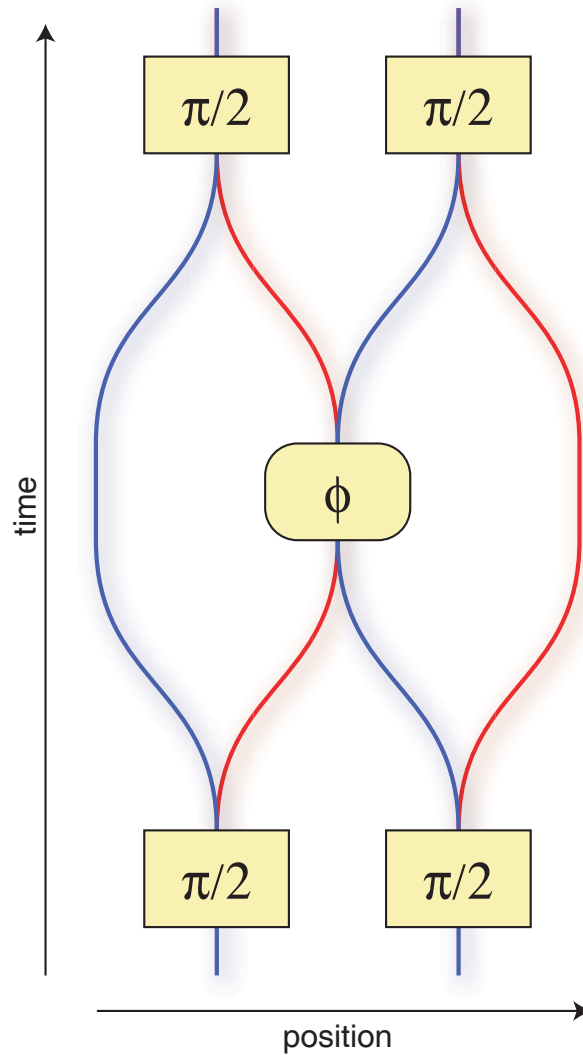
Figure 1.2.: Atom interferometer for two atoms. The graph is read from the bottom to the top. $\pi/2$ microwave pulses act as the beam-splitters. If both atoms end up in the same arm of the interferometer, they pick up a phase-shift ϕ.

higher atom numbers, a cluster state is formed [11]. This state is as maximally entangled as the GHZ state is, but more robust against complete destruction of entanglement.

In this work, measurements of this and other interferometer sequences are presented showing a series of entanglement and disentanglement processes. As the lattice is three-dimensional, and the shifting happens only in one dimension, one run on the experiment creates a large number of realizations of the described 1D-experiment. This work closes by examining the prospects of extending the process to more dimensions, and possible applications.

Overview

The Mott Insulator in an Optical Lattice In this chapter the experimental techniques to creating a BEC are presented. This BEC is just a starting point for preparing a MI, which is covered in the second half of the chapter. The chapter closes with the description of an experiment showing that ultracold collisions produce a completely coherent phase-evolution. This is one of the requirements for quantum gates in an optical lattice.

Quantum Gates in Spin-Dependant Lattices This chapter begins with an introduction to the basic ideas behind quantum information processing, such as qubits. The realization of quantum gates in the optical lattice is discussed in the second part of this chapter. The technique for moving the two spin-dependent lattices is shown, followed by experiments on the creation of massively entangled states in the system.

Outlook The outlook sketches ideas for the next steps along the route to a universal quantum simulator in optical lattices. These include higher dimensional cluster states and gates to not-next neighbours.

Selected publications on this apparatus

The marked publications can be found in appendix B.

- I. BLOCH, M. GREINER, O. MANDEL, T. W. HÄNSCH, and T. ESSLINGER. *Sympathetic cooling of ^{85}Rb and ^{87}Rb*. Phys. Rev. A **64**, 021402–4 (2001).

- M. GREINER, I. BLOCH, O. MANDEL, T. W. HÄNSCH, and T. ESSLINGER. *Exploring phase coherence in a 2D lattice of Bose-Einstein condensates*. Phys. Rev. Lett. **87**, 160405–4 (2001).
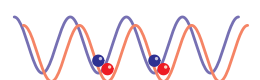
- M. GREINER, O. MANDEL, T. ESSLINGER, T. W. HÄNSCH, and I. BLOCH. *Quantum phase transition from a superfluid to a Mott insulator in a gas of ultracold atoms.* Nature **415**, 39–44 (2002).

⇒ M. GREINER, O. MANDEL, T. W. HÄNSCH, and I. BLOCH. *Collapse and revival of the matter wave field of a Bose-Einstein condensate.* Nature **419**, 51–54 (2002).

⇒ O. MANDEL, M. GREINER, A. WIDERA, T. ROM, T. W. HÄNSCH, and I. BLOCH. *Coherent transport of neutral atoms in spin-dependent optical lattice potentials.* Phys. Rev. Lett. **91**, 010407–4 (2003).

⇒ O. MANDEL, M. GREINER, A. WIDERA, T. ROM, T. W. HÄNSCH, and I. BLOCH. *Controlled collisions for multi-particle entanglement of optically trapped atoms.* Nature **425**, 937–940 (2003).

- M. GREINER, O. MANDEL, T. ROM, A. ALTMEYER, A. WIDERA, T. W. HÄNSCH, and I. BLOCH. *Quantum phase transition from a superfluid to a Mott insulator in an ultracold gas of atoms.* Physica B **329–333**, 11–12 (2003).

- A. WIDERA, O. MANDEL, M. GREINER, S. KREIM, T. W. HÄNSCH, and I. BLOCH. *Entanglement interferometry for precision measurement of atomic scattering properties.* Phys. Rev. Lett. **92**, 160406–4 (2004).

- B. PAREDES, A. WIDERA, V. MURG, O. MANDEL, S. FÖLLING, I. CIRAC, G. V. SHLYAPNIKOV, T. W. HÄNSCH, and I. BLOCH. *Tonks-Girardeau gas of ultracold atoms in an optical lattice.* Nature **429**, 277–281 (2004).

- T. ROM, T. BEST, O. MANDEL, A. WIDERA, M. GREINER, T. W. HÄNSCH, and I. BLOCH. *State selective production of molecules in optical lattices.* Phys. Rev. Lett. **93**, 073002–4 (2004).

2. The Mott Insulator in an Optical Lattice

The experiments described in chapter 3 are conducted in a system of ultracold atoms arranged in an artificial crystal (described in detail in ref. [12]). Each atom has to be in the groundstate of the external potential so that it cannot relax into any other quantum-state. This requirement of all atoms being in the ground state is met by bringing the system into the Bose-Einstein-Condensate (BEC). The creation of such a BEC is described in section 2.1.

The crystal lattice is created by dipole forces of a patterned light field. This potential consists of many lattice sites, each a small trap for ^{87}Rb. For moderate lattice strengths, neighbouring lattice sites are coupled by tunnelling. The dipole trap and its realisation in our experiment are discussed in section 2.2.

In strong lattices, each lattice site can be populated by exactly one atom. This state, the Mott-Insulator (MI), allows to store atoms while suppressing interactions with their neighbours. The MI can be created from a BEC by adiabatically switching on the light crystal, as the MI is as well a groundstate as the BEC is. The distinction between weak and strong lattices and experimental results on the Mott-Insulator state can be found in section 2.3.

One of the basic assumptions for the quantum gates used later on is that collisions between ultracold atoms leave the external state of the two-atom system unchanged. Only the phase of the system is evolving due to the collision. This has been observed in section 2.4, where collisions cause the collapse of a macroscopic matter wave, only to restore the original state after twice that time.

2.1. Creating a Bose-Einstein Condensate

Bose-Einstein-Condensate has been studied in detail since long before its realisation in 1995 [13–15]. For a review of BEC, see ref. [16–21]. In the following you find a short introduction from the experimental point of view.

The critical temperature T_c, at which a thermal gas Bose-condenses, is
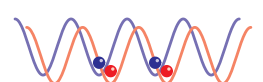
dependent on the density ρ of the gas and its de Broglie wavelength λ_{dB}. For a homogeneous system, the critical temperature is given by:

$$\rho\lambda_{\mathrm{dB}}(T_c) = \rho\left(\frac{2\pi\hbar^2}{mk_{\mathrm{B}}T_c}\right)^{\frac{3}{2}} \approx 2.612\ldots. \tag{2.1}$$

Here m is the atomic mass. For ^{87}Rb in a trap, the critical temperature is typically on the order of a few 100–1000 nK, which means that there has to be a good thermal isolation from the environment. As the thermal capacitance of the dilute atomic gas is negligible, no mechanical contact of any sort can be allowed between the sample and the environment. This leaves as experimental surroundings only an Ultra-High-Vacuum (UHV) chamber where the sample is levitated against gravity. Most experiments use for this purpose electromagnetic atom traps, but BEC was also achieved in purely optical traps [22, 23].

The only connection between the hot environment and the atom cloud in the trap, apart from black-body radiation, are atoms in the background-gas that are at room-temperature. If an atom from the cold sample collides with an atom from the hot background gas, it acquires so much kinetic energy, that it can leave the trap. These collisions therefore have to be suppressed: The lower the background pressure, the longer the trap live-time.

2.1.1. Magneto-Optical Trap

The first cooling stage on the way from a dilute room-temperature ^{87}Rb-gas to a BEC is the Magneto-Optical Trap (MOT) [24–26]. It uses the momentum-transfer from the photons of a laser field to the atoms of a dilute gas to cool down the gas to a temperature of $\approx$100 μK while at the same time holding the atoms isolated from thermal contact to the hot environment.

In essence, in a MOT atoms are slowed down and trapped by the momentum transferred to them when they absorb a photon from one of the cooling lasers. The atom returns to the groundstate by spontaneously emitting a photon in a random direction. Over many cycles, these random emissions cancel out, leaving only the momentum transferred by the absorption process. This momentum acts as a force in the direction of the laser beam.

The cooling laser is red-detuned with respect to an atomic transition, so that for atoms moving in the direction of the beam this detuning gets

reduced and the absorption probability is increased. These atoms are thus decelerated by the momentum transfer. The decelerating force is maximal for that velocity, where the Doppler shift exactly cancels the detuning of the laser. The profile of the velocity-dependent force is Lorentzian in shape. If a second laser beam propagating in the opposite direction is added, the total force on an atom has a linear velocity dependence for slow atoms. This friction force slows down the atom, if it is initially slow enough. This can be extended to a three-dimensional cooling scheme, by adding laser beams from all directions.

This scheme is called an optical molasses, because of its friction forces. But there is no position-dependant force, atoms are not trapped in an optical molasses. A quadrupole type magnetic field together with well chosen circular polarisations of the used light can add this position dependence, as is illustrated in fig. 2.1. The Zeeman splitting changes the transition energy in stronger fields and the polarisation of the laser beams select which sub-level is coupled to which beam.

The level scheme of ^{87}Rb is more complicated than shown in fig. 2.1. The ground state is split by Fine- and Hyperfine-structure (see fig. C.1 on page 110). There is a closed transition $|F = 2\rangle \to |F' = 3\rangle$ that can be used to run the MOT close by. To compensate off-resonant decay into the $|F = 1\rangle$ ground state, another laser on the transition $|F = 1\rangle \to |F' = 2\rangle$ is used to return these atoms to a point where they can decay into the $|F = 2\rangle$ ground state.
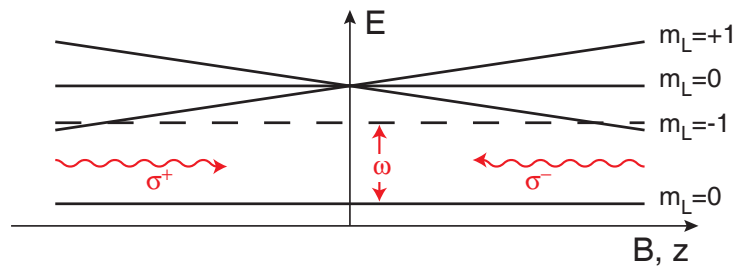
Figure 2.1.: Working principle of a MOT. An atom with an L=1 excited state and an L=0 groundstate is shown in the presence of a quadrupole field. The Zeeman-splitting shifts the $m_L = \pm 1$ states into resonance to light coming from the outside of the trap. The light hitting the atom from the other side is tuned out of resonance. The atom is therefore propelled back to the trap centre.
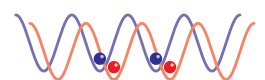
2.1.2. Magnetic Traps

In our experiment, the vacuum in the MOT-chamber has a pressure of $\approx 10^{-9}$ mbar, and is thus in the range of an UHV. This pressure is low enough to have a trap lifetime of a few seconds, limited by collisions with the background gas. While this is not sufficient to actually conduct the experiment, it is long enough to cool atoms heated by a collision down again with the MOT. The pressure has to be this high, as the MOT is loaded from the background gas [27]. Lowering the pressure to get better lifetimes would reduce the loading rate and final atom number of the MOT.

In order to get both a high atom number in the MOT and a long lifetime for the experiment, the apparatus is split into two different UHV chambers. The MOT-chamber is used to collect a high atom number at low trap lifetimes. The atoms are then transferred into a second chamber with a pressure of $\approx 10^{-11}$ mbar, where the experiment can be conducted at a lifetime of 90 s. Before the transport, the sample is loaded from the MOT into a trap made by purely magnetic forces [28–31]. This magnetic trap can be shifted from one chamber to the next, taking the atoms with it [32].

In a magnetic field B, an atom with non-vanishing magnetic moment $g_F \mu_B$ can occupy different states of the magnetic quantum number. Here g_F is the Landé g-factor and μ_B is the permeability of vacuum. Due to Zeeman splitting, the energy of a state with magnetic quantum number m_F is shifted by

$$E = g_F m_F \mu_B B. \tag{2.2}$$

For states with the right sign of $g_F m_F$ the energy decreases for decreasing magnetic field (see fig. C.2 on page 110. In a magnetic gradient, these atoms are subject to a force toward the minimal magnetic field and are therefore called "low-field-seeker". In ^{87}Rb these are the states $|F = 2, m_F = +1\rangle$, $|F = 2, m_F = +2\rangle$ and $|F = 1, m_F = -1\rangle$.

The trap field is generated by two magnetic coils in anti-Helmholtz configuration. They create a quadrupole in the centre between the two coils. The configuration is basically the same as for the MOT, which also needs a magnetic field minimum in the trap centre. But where the Zeeman splitting in the MOT is just used to address the right transition, in the magnetic trap it defines the trap-depths. The gradients in our magnetic trap are therefore roughly one order of magnitude stronger than in our MOT.

The magnetic trap is moved over a distance of 40 cm between the two vacuum chambers by means of a row of partially overlapping coil pairs (see fig. 2.2 on the facing page). At every moment of the transport the

trap is formed by two or three neighbouring coil pairs. The currents in the coils are ramped to move the quadrupole adiabatically from the MOT to the BEC position.

In order for an atom to be stored in the magnetic trap, its magnetic moment has to oriented correctly with respect to the magnetic field. As the magnetic moment is created by the spin of the atom, this orientation can be expressed as a m_F quantum number. If the spin is flipped, the field gradient would repel the atom from the trap centre. An atom with a certain spin orientation would be trapped on one side of the trap, but anti-trapped on the opposite side (see fig. 2.3 on the next page). As long as the magnetic field changes slowly compared to the larmor frequency ω_L, the spin follows changes in the field gradient, so an atom trapped once remains trapped for all locations. Only at the trap centre, where the field reverses orientation, the atomic spin cannot follow and it thus undergoes a Majorana spin flip [33]. The effect is negligible at MOT temperatures, but can become the dominant loss mechanism for colder clouds [34, 35]. To prevent the resulting atom loss, a Ioffe Pritchard trap with a finite magnetic field in the trap centre is used [36, 37]. For the Quadrupole-Ioffe-Configuration (QUIC) type trap [38], the offset is created by a third coil, changing the trap geometry to a parabolic shape.
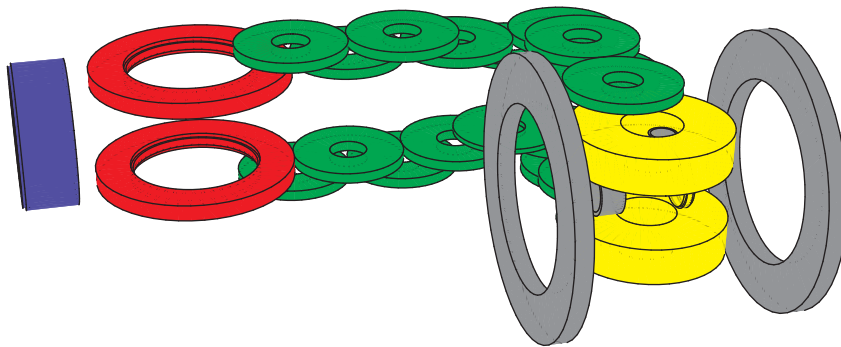
Figure 2.2.: Magnetic coils of the experiment. The vacuum chamber (not shown) is situated in between the coil pairs. The transport starts from red MOT-coils on the left hand side. The transport-coils shown in green connect this trap to the final trap made by the yellow BEC-coils. Shown in grey are additional coils for offset- and gradient-fields. The small compensation coils for the magnetic earth field are not shown.
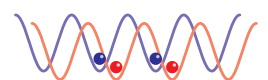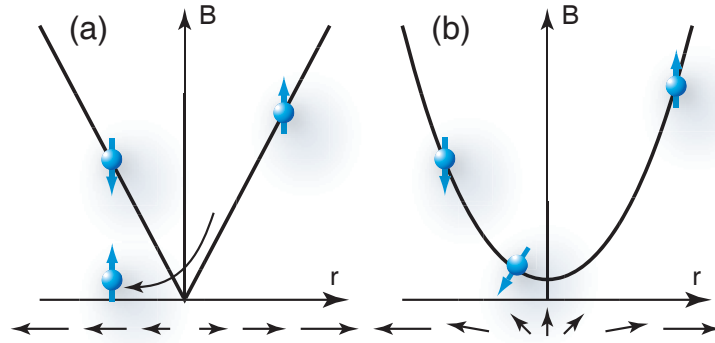
Figure 2.3.: Profile of magnetic traps. The absolute field strength
is plotted over the distance from the trap centre. The arrows
indicate the magnetic field vector. **(a)** Plot of a quadrupole trap
with two trapped and one untrapped atom. The spins of the
atoms are reversed on different sides of the trap to compensate
for the different orientation of the magnetic field. An atom
passing through the magnetic field zero is flipped into an anti-
trapped state. **(b)** Plot of a Ioffe-Pritchard trap. The trap has
no magnetic field zero and thus the atoms can not escape from
the trap centre.

2.1.3. Evaporation

After the atom-cloud has been transferred to a magnetic trap with a long
lifetime, it is at a temperature of $\approx 100\,\mu$K. To bring the system into the
absolute ground state, the phase-space-density $n\lambda_{dB}^3$, a product of density
n and de Broglie wavelength λ_{dB}, has to be larger than a critical value [16].
For the homogeneous case, this is

$$n\lambda_{dB}^3 \gg 2.6. \tag{2.3}$$

For our experiment, this translates to a temperature of a few $100\,$nK.
The last cooling step is done by continuously removing the hottest atoms
from the sample [35, 39–42]. They carry away more than the average
energy and the mean energy per atom of the remaining atoms is thus
reduced. The important prerequisite for this technique is collisions be-
tween the atoms to rethermalise the sample. Only after rethermalisation
are there more above-average-energy atoms. The simplified picture of
discrete steps of cutting off the thermal distribution followed by rether-
malisation is shown in fig. 2.4 on the facing page.

P(v,T)

0.26

0.45

0.68

1.00

v
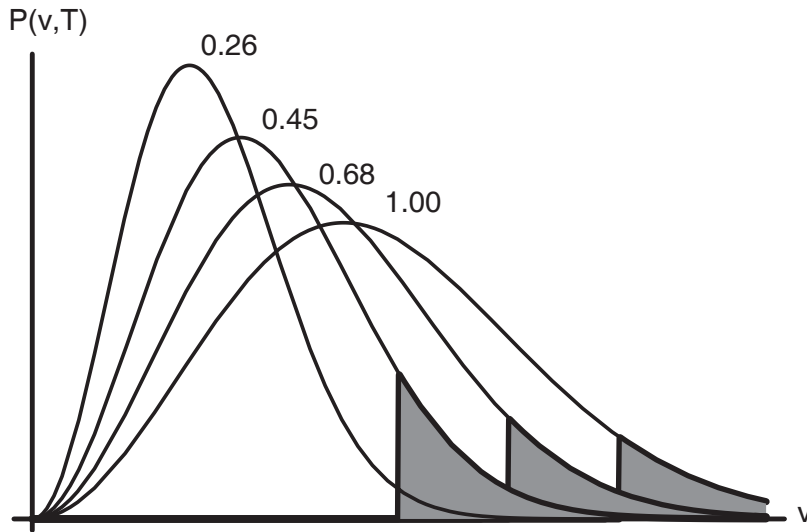
Figure 2.4.: Evaporation in steps. Shown are atom-number distri-
butions over velocity. The back-most at relative temperature 1
is then cut by the shaded area to yield the next curve further
to the front with a temperature of 0.68. This is repeated twice
to give a curve with a relative temperature of 0.26.

2.1.4. Imaging of the Atom Cloud

To measure the atom number, the spatial or momentum distribution and
temperature of the system, an absorption image is used (imaging is dis-
cussed in detail in ref. [21]). The atom cloud is illuminated with resonant
light. Where the atom density is higher, absorption is larger and the beam
caries an imprinted shadow showing the spatial atom distribution. This
shadow is then imaged onto a Charge Coupled Device (**CCD**) camera.
The absorption of the beam I_0 by the cloud is given by the optical density
D:

$$I = I_0 e^{-D}.$$ (2.4)

As the light beam integrates absorption along the beam axis z, only the
column density can be measured. For an atom cloud of density $n(\boldsymbol{r})$ with
a polarisation averaged scattering cross section σ_0, saturation intensity
I_sat and natural line width Γ illuminated by a beam of intensity I and
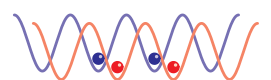
detuning Δ to the transition, the optical density is:

$$D = \frac{2\sigma_0}{1 + I/I_{\text{sat}} + 4\Delta^2/\Gamma^2} \int n(\boldsymbol{r})\mathrm{d}z \tag{2.5}$$

All terms apart from the column density given by the integral are known proportionally factors, so

$$\int n(\boldsymbol{r})dz \propto \log\left(\frac{I}{I_0}\right) \tag{2.6}$$

The BEC is $\approx 30\,\mu$m large, which would be only 6 pixels on one of our cameras. Getting a cloud size of even 20 pix would require a strong magnification. But it is possible to increase the size of the cloud and then image with a much lower magnification. The cloud size is increased by switching off all trap potentials and letting the cloud expand in a Time-of-Flight (TOF) expansion. During the TOF, the atoms that had the largest momentum at the trap switch-off time, are the fastest and thus the farthest from the cloud centre. The TOF acts akin to a Fourier transformation on the sample. The images after a TOF show the momentum space distribution. From it, also the classical temperature can be calculated. An illustration of the imaging process together with a sample image can be seen in fig. 2.5.
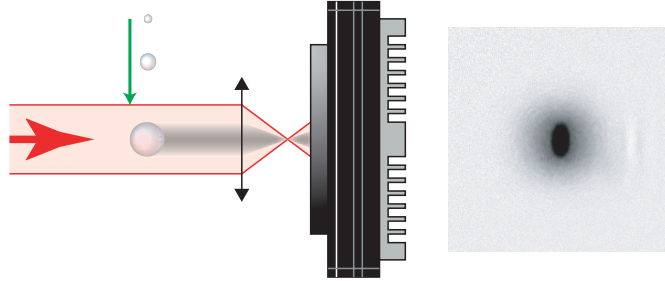
Figure 2.5.: Imaging the cloud of atoms. Shown in the illustration is the TOF-expansion of a cold atom cloud (green arrow). Then a resonant light pulse hits the atoms and projects their shadow on a CCD-camera. Right of that is an example image, partially condensed after 25 ms TOF. The central black spot is the shadow of the BEC. It is optically dense, so the camera detected no light at this point.

2.2. Introduction to Optical Lattices

The goal is to have a regular array of potential wells. Such a potential cannot be created by our magnetic trap, even though there are efforts by other groups to create potential arrays in micro-structured magnetic traps. We use a conservative trap made of structured light fields instead. The structure-size is $\lambda/2$ (where λ is the wavelength of the light).

After introducing this type of trap, called dipole-trap, the basic idea of an optical lattice is introduced. Absorption images of atoms from such a lattice are discussed.

2.2.1. Dipole Traps

Dipole traps are conservative traps for neutral atoms, molecules and even macroscopic particles created by intense laser light [43, 44]. Here we start from the simplified case of a two-level atom with transition frequency ω_0 in a light field of frequency ω. A classical approach is that the electrical field of the laser induces a dipole in the atom, where the phase of the induced dipole depends on the detuning $\Delta = \omega - \omega_0$. From these assumptions, the potential created by the laser field can be calculated. For an introduction into dipole traps using this approach, see refs. [45, 46].

Here, we will use a different motivation, based on the light shift of the atoms groundstate [47]. The unperturbed energy states of an atom are $\mathcal{E}_i$, with i counting the different atomic states $|i\rangle$. Then the energy shifts for the atom in the presence of an light-atom-interaction Hamiltonian $\hat{H}$ are given by:

$$\Delta E_i = \sum_{j(\neq i)} \frac{|\langle j|\hat{H}|i\rangle|^2}{\mathcal{E}_i - \mathcal{E}_j}. \tag{2.7}$$

For dipole traps, the interaction Hamiltonian is given by $\hat{H} = -\hat{\mu}\boldsymbol{E}$, $\hat{\mu} = -e\boldsymbol{r}$ being the electric dipole operator and $|\boldsymbol{E}| = \frac{1}{2}Ee^{-i\omega t} + c.c.$ is the electrical field of the incident laser field. The energies $\mathcal{E}_i$ are expressed using the dressed state approach. The atom and the laser field are combined and that energy is considered.

For a two-level atom with a transition frequency ω_0 and a light field of n photons of frequency ω, the total energy of the ground state is $\mathcal{E}_i = n\hbar\omega$. The excited state has an energy of $\mathcal{E}_j = \hbar\omega_0 + (n-1)\hbar\omega =: n\hbar\omega - \hbar\Delta_{ij}$.
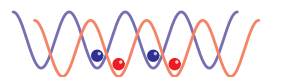
This result also holds for a multi-level atom, so (2.7) becomes:

$$\Delta E_i = \sum_{j(\neq i)} \frac{|\langle j|\hat{\mu}|i\rangle|^2}{\hbar\Delta_{ij}} \left|\tfrac{1}{2}E\right|^2. \tag{2.8}$$

In the matrix element $\mu_{ij} := |\langle j|\hat{\mu}|i\rangle|$ the hyperfine part can be factored out as a c_{ij}:

$$\mu_{ij} = c_{ij}\|\mu\|. \tag{2.9}$$

The reduced matrix element $\|\mu\|$ is still dependent on the fine-structure and can be expressed in terms of the spontaneous decay rate as

$$\|\mu\|^2 = \frac{3\pi\epsilon_0\hbar c^3\Gamma}{\omega_0^3} \tag{2.10}$$

Here ϵ_0 is the electric constant, and c is the speed of light. The transition coefficient c_{ij} is also dependant on the fine-structure but also contains dependences on the light polarisation and possibly the hyperfine-structure. For the case of finestructure splitting only the transition coefficient is given in (3.1).

With these ingredients and $I = \frac{1}{2}\epsilon_0 c|E|^2$, the level shift for an atom in the ground state $|i\rangle$ can be written as:

$$\Delta E_i = \frac{3\pi c^2\Gamma}{2\omega_0^3} I \sum_{j(\neq i)} \frac{c_{ij}^2}{\Delta_{ij}}. \tag{2.11}$$

This Stark shift is inhomogeneous for laser beams, where it is strongest at light-intensity maxima. For $\Delta E < 0$ this means a reduction in energy inside a local intensity maximum, i.e. a conservative trap. With all other factors being positive, this happens for $\Delta_{ij} < 0$, i.e. when the laser is red detuned relative to the nearest/strongest transitions. The trap depth U_{dip} is thus the energy shift ΔE for the light-intensity at the trap centre.

So far, the possibility for atoms to scatter a photon from the beam was neglected. Such an event destroys any coherence present in the system and thus has to have a low probability during the experiment time. The scattering rate Γ_{sc} can be given as:

$$\Gamma_{\mathrm{sc},i} = \frac{3\pi c^2\Gamma^2}{2\hbar\omega_0^3} I \sum_{j(\neq i)} \frac{c_{ij}^2}{\Delta_{ij}^2}. \tag{2.12}$$

Simplifying to a single transition line, the scattering rate Γ_{sc} is proportional to the trap depth U_{dip}:

$$\hbar\Gamma_{\text{sc}} = \frac{\Gamma}{\Delta}U_{\text{dip}}. \tag{2.13}$$

For low scattering rates at a given trap depth, the detuning Δ has to be increased. To keep the trap depth constant, this means increasing the light intensity I also.

2.2.2. Optical Lattice

The artificial crystal used throughout this work is formed by a dipole potential. Red detuned laser light at a wavelength of $\lambda \approx 830\,nm$ traps the atoms in maxima of the light intensity. So the light-field intensity needs to be shaped in a regular 3D pattern of intensity maxima. To this end, interference of different laser beams at the position of the atom cloud is used. Such optical lattices have been widely used before for diffracting atoms [48–50]; cooling [51–55], Bragg spectroscopy [56] and superlattices [57] were studied. The lattice-setup used here is introduced in ref. [58].

To keep the atoms from distributing over too large a distance, the lattice is superimposed with an additional trap. This trap is generated by a dipole laser beam focused at the position of the atom cloud. Perpendicular to the beam axis, this creates a Gaussian intensity profile. For small excursions from the trap centre this is a near harmonic trap. Along the beam axis, the trapping frequency is too low, though: atoms could spread out many $100\,\mu$m. To close the trap in this direction, a second (and later a third) perpendicular laser beam is focussed onto the atom cloud.

If one of these laser beams is now collimated after passing through the atom cloud and retro-reflected on a mirror, the intensity and thus the trap-depth at the trap centre is doubled. But now a standing wave forms, with its first node at the surface of the retro-reflecting mirror. The interference pattern extends back to the atom cloud, producing an intensity modulation with a distance of $\lambda/2$ between intensity maxima. The potential profile along such a beam is shown in fig. 2.6 on the following page.

A 2D or 3D lattice is formed by also retro-reflecting the other laser beams. The standing waves intersect and lattice sites are where all standing waves have an intensity maximum. Consider the oblate traps of one standing wave as parallel planes. Then two perpendicular groups of planes intersecting with each other form an array of cigar-shaped traps
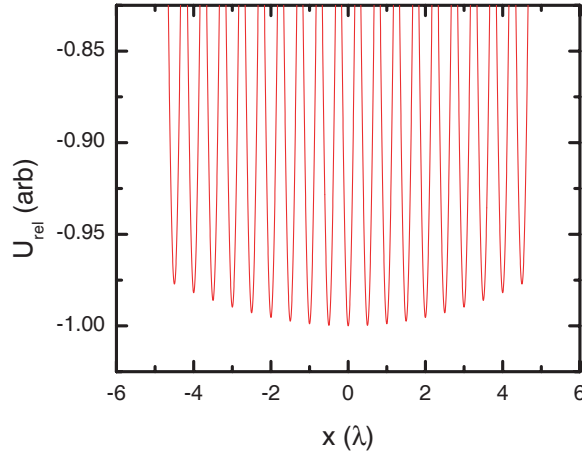
Figure 2.6.: Potential of a 3D dipole lattice. Shown is the potential
depths along one axis as a function of position. The additional
confinement overlapping the lattice structure is created by the
two other lattice beams. This effect is exaggerated by reducing
the beam waist to 20 μmin the plot.

in a regular 2D lattice. A third group of parallel planes divides these 2D
lattice sites into spherical symmetric traps arranged in a 3D lattice.

The lattice beams are generated by lasers on a separate optical table. On
that table, the beams for each of the three axes pass through an Acusto-
Optical Modulator (AOM) that acts as a variable attenuator. Then optical
single-mode fibres are used to transmit the light to the experiment and
also to clean the laser-mode to a Gaussian TEM$_{00}$ mode.

Acoustic noise can modulate the refractive index of the fibre and there
are also drifts in the fibre coupling alignment and in the laser output in-
tensity. These fluctuations of the lattice beam intensity can lead to an
unwanted parametric heating. To suppress fluctuations, the intensity is
measured at the fibre output coupler and an active regulation stabilizes
the intensity to the desired value using the AOM.

The setup on the experiment table is shown in fig. 2.7 on the next page.
The telescope **(a,b)** is used to change the beam diameter on lens **(d)**. This
lens focuses the lattice beam onto the atoms and with the telescope the
waist-size can be selected. We use a beam waist of $\approx$100 μm at the posi-
tion of the BEC (waist as the radius of the $1/e^2$ intensity drop-off). While
the beam is collimated, the polarisation is cleaned by a polarizing beam
splitter **(c)**, which can also be used to superimpose additional beams for

the detection imaging onto the lattice beam. The detection light thus has a different linear polarisation than the lattice light. A mirror **(e)** is used to direct the focus of the lattice beam onto the position of the BEC **(f)** in the magnetic trap. The beam is collimated after the vacuum chamber with lens **(g)**. The polarizing beam splitter **(h)** separates lattice and imaging light. The mirror **(i)** reflects the lattice beam back into the same mode, so the path of the light is reversed. The imaging light passes through **(h)** and the lens **(j)** images the BEC position onto the camera **(k)**.

The lattice depth is usually measured in units of the recoil energy (m is the mass of the atom):

$$E_{\mathrm{R}} = \frac{\hbar^2 k^2}{2m}.$$

With our setup it is possible to produce lattices of up to $45\,E_{\mathrm{R}}$ in all three axes.
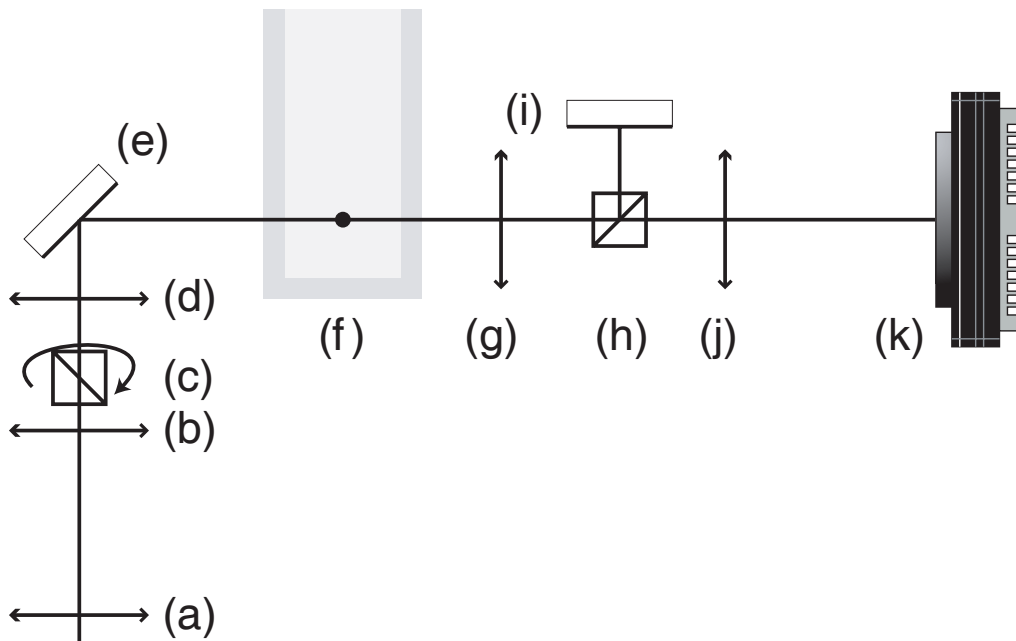
Figure 2.7.: Schematic of the optical setup for a lattice axis. For a description of the labels, see the text.
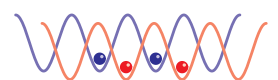
2.2.3. Wannier Functions

There are two prominent wave function descriptions for atoms in a lattice potential. In solid state physics, such systems are often described in terms of Bloch functions (see e.g. [59]). These wave functions are not localised to a lattice site but are infinitely large while having the same periodicity as the lattice potential. The Bloch wave function $\phi_q^{(n)}$ can be written as

$$\phi_q^{(n)} = e^{i\frac{qx}{\hbar}} u_q^{(n)}(x). \tag{2.14}$$

Here q is the quasi momentum in the first Brillouin zone and n denotes the nth Bloch band. The function $u_q^{(n)}(x)$ keeps the periodicity of the lattice potential. The Schrödinger equation for the periodic part of the Bloch function becomes

$$\underbrace{\hat{H}_{\text{B}}}_{\frac{1}{2m}(\hat{p}+q)^2 + V(x)} u_q^{(n)}(x) = E_q^{(n)}(x) u_q^{(n)}(x). \tag{2.15}$$

And the potential can be written as

$$V(x) = -V_0 \cos^2(kx) = -\frac{1}{4}V_0 \left(e^{+i2kx} + e^{-i2kx} - 2 \right), \tag{2.16}$$

which is a cosine with amplitude V_0 and minimum 0.

If $u_q^{(n)}(x)$ is developed as a discrete Fourier sum

$$u_q^{(n)}(x) = \sum_l c_l^{(n,q)} e^{i2lkx}, \tag{2.17}$$

and $\hat{p} u_q^{(n)}(x) \to 2\hbar kl \times u_q^{(n)}(x)$ is used to translate the momentum operator in the Fourier sum, then (2.15) can be rewritten as:

$$\sum_l \sum_{l'} H_{l,l'} c_l^{(n,q)} e^{i2lkx} = \sum_l E_q^{(n)}(x) c_l^{(n,q)} e^{i2lkx} \tag{2.18}$$

with the Hamilton operator in matrix form:

$$H_{l,l'} = \begin{cases} \left(2l + \frac{q}{\hbar k}\right)^2 E_{\text{R}} + \frac{1}{2}V_0 & \text{if } l = l', \\ -\frac{1}{4}V_0 & \text{if } |l - l'| = 1, \\ 0 & \text{else.} \end{cases} \tag{2.19}$$

This form of the Schrödinger equation is solvable if the Hamiltonian is truncated for large l: By requiring a solution for all x the sum over l can

be removed together with the x-dependant exponential. The remainder is an eigenvector problem $\boldsymbol{H}\boldsymbol{c}^{(n,q)} = E_q^{(n)}\boldsymbol{c}^{(n,q)}$. As the components $c_l^{(n,q)}$ become very small for large l, for the ground state a truncation of $-5 \leq l \leq +5$ is sufficient for many applications. The Bloch function $\phi_q^{(n)}$ can be calculated from these resulting eigenvectors. The eigenvalues $E_q^{(n)}$ as a function of the quasi-momentum q are shown in fig. 2.8.

The Bloch states described above are delocalised over the complete lattice. For the description of storing atoms in a single lattice site they are not well suited, though. For that purpose, the Wannier states $w_n(x - x_i)$ are better suited [60]. They are a superposition of Bloch states and describe atoms stored in a single lattice site at position x_i:

$$w_n \propto \sum_q e^{-i\frac{qx_i}{\hbar}} \phi_q^{(n)}(x). \tag{2.20}$$

Especially in strong lattices Wannier functions resemble Gaussian functions. But where Gaussian functions become continuously smaller for larger distances to the trap-centre, Wannier functions have small side-lobes at the position of neighbouring lattice sites (see fig. 2.9 on the next page). This difference becomes crucial in the calculation of the overlap between atoms stored in neighbouring lattice sites. The probability for an atom to tunnel from one lattice site to the next is connected to this overlap (see eq. (2.22)).
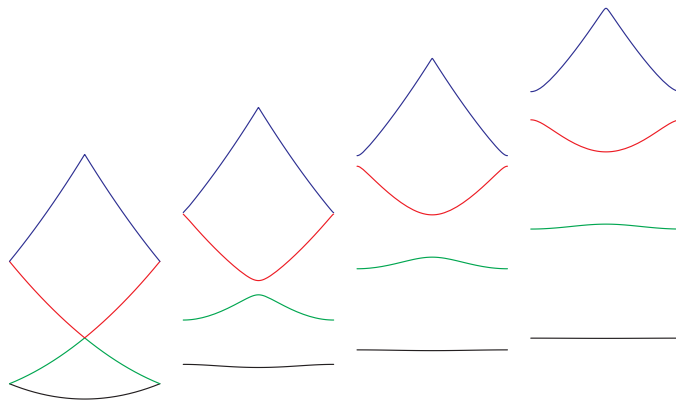
Figure 2.8.: Bloch bands for different lattice strengths. The first 4 bands are plotted for energies of $0\,E_R$, $6\,E_R$, $12\,E_R$ and $18\,E_R$.
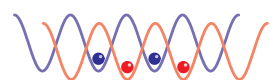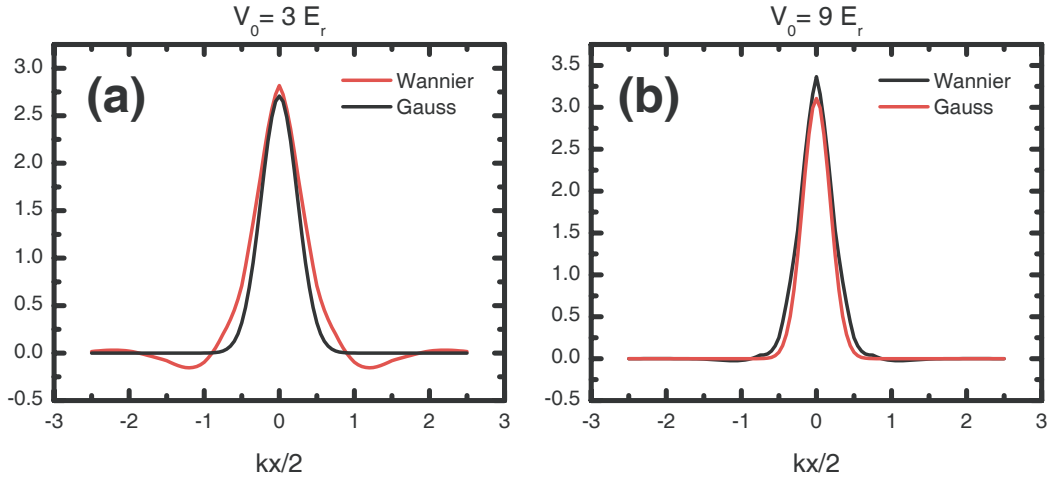
Figure 2.9.: Wannier functions compared to Gaussian functions. The position axis is scaled in units of the lattice spacing. **(a)** For low lattice depths, the Wannier and Gauss functions differ significantly. **(b)** with increasing lattice depths, the difference diminishes.

2.2.4. State Diagnosis in the Optical Lattice

As the lattice spacing is only $\approx 415\,\mathrm{nm}$, resolving individual lattice sites is not possible with our imaging wavelength of $\lambda = 780\,\mathrm{nm}$. Instead, a TOF expansion as for the BEC is used. The Fourier-Transformation during the TOF is identical to the operation that generates the reciprocal lattice in solid state physics. There a simple cubic lattice in real space is connected to a different simple cubic lattice in momentum space.

Let us for this chapter assume that each lattice site contains a small BEC with an initially common phase (for details, see section 2.3.1). Then during the TOF each lattice site is the source of a coherent matter wave, that interferes constructively at the position of reciprocal lattice sites. Phase-differences between neighbouring lattice sites are equivalent to a quasi-momentum in the reciprocal lattice. This quasi-momentum can be seen in absorption images as fig. 2.10 on the facing page, where the system undergoes Bloch-oscillations in a tilted lattice.

The width of the reciprocal lattice peaks also contains important information: as in light-interference from a grating, the more coherent sources interfere with each other, the narrower the interference pattern is. We use this to detect relative changes in the coherence of the system in the MI

experiments of section 2.3.2.

It is also possible to detect the population of higher bands than the ground state. Consider the illustration in fig. 2.11 on the next page: the first three images show the bands of the the lattice potential for different lattice depths. For a vanishing lattice, the quasi-momentum is mapped onto different points of the free particle parabola, dependant on the band the particle was stored in. As the TOF corresponds to a transformation from momentum-space to real space, the momenta of particles from different bands end up in different regions in the absorption image. In solid state physics, these regions are called Brillouin zones.

Experimentally, the mapping is done by switching off the lattice potential adiabatically with respect to the trapping frequency but slowly compared to the tunnelling time [58]. This leaves the atoms in higher bands enough time to map their quasi-momentum onto real momentum, but the system is not returning into the BEC, the new groundstate of the system without a lattice.
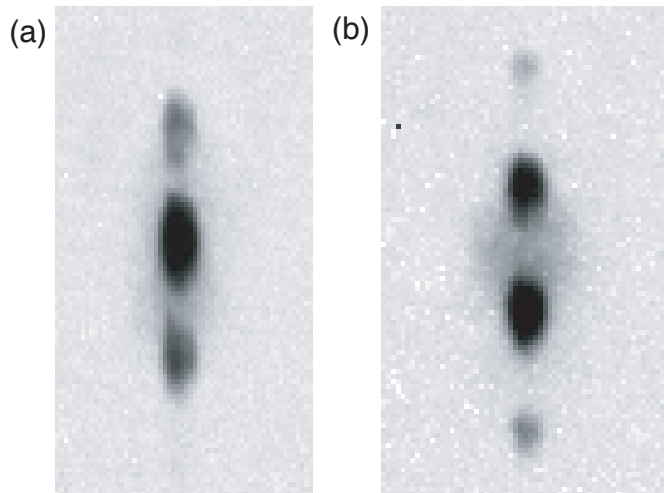
Figure 2.10.: Bloch oscillations in a one-dimensional lattice. The images are taken after a TOF of 15 ms, with the gradient causing a phase ϕ between nearest neighbours of: **(a)** $\phi = 0$ and **(b)** $\phi = \pi$.
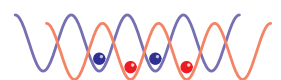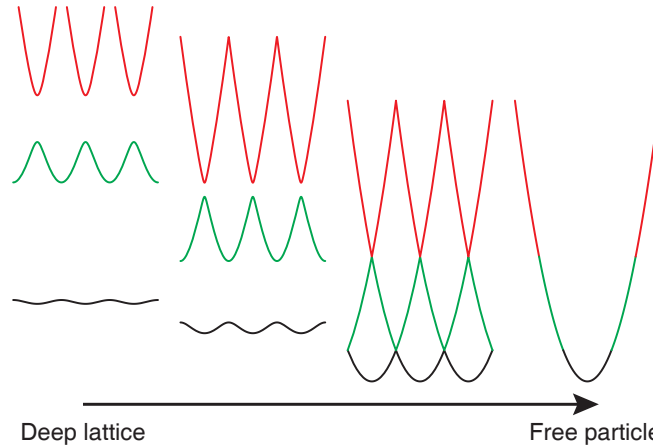
Figure 2.11.: Transition from Bloch bands to Brillouin zones. Shown are the first three bands of the lattice and their evolution to lower lattice-depths. When the lattice vanishes, the quasi-momentum becomes a real space momentum, depending on the former trap level of the particle (colour-coded).

2.3. The Mott-Insulator Phase

In the previous chapter, the optical lattice was introduced as the potential our ^{87}Rb atoms are stored in. Now we want to discuss the ground state of cold bosons in this system: how do atoms distribute in the potential wells? We want to create a situation, were at each lattice position there is one atom. This state, the Mott-Insulator (MI) is introduced here.

2.3.1. The Bose-Hubbard Hamiltonian

In solid state physics, electrons in a regular crystal are described by the Hubbard Hamiltonian. There has been a huge amount of theoretical work invested in understanding this Hamiltonian [61], as it describes conduction in regular metals. While the Hubbard Hamiltonian applies only to fermionic particles, its pendant for bosonic particles, the Bose-Hubbard Hamiltonian [62], has been under scrutiny also. In 1998, it was pointed out [7] that an optical lattice filled with cold atoms can be described by the Bose-Hubbard Hamiltonian. The potential is a lattice of potential wells,

numbered with indices i or j:

$$\hat{H} = \underbrace{-J \sum_{\langle i,j \rangle} \hat{a}_i^\dagger \hat{a}_j}_{\text{Kinetic}} + \sum_i \epsilon_i \hat{n}_i + \underbrace{U \frac{1}{2} \sum_i \hat{n}_i(\hat{n}_i - 1)}_{\text{Interaction}} \qquad (2.21)$$

The kinetic term describes the tunnelling process between neighbouring lattice sites. The sum runs over nearest neighbours only, the creation operator $\hat{a}_i^\dagger$ and the annihilation operator $\hat{a}_i$ create or destroy a particle at lattice site i. The tunnel matrix element J is:

$$J = - \int w_0^\dagger(\boldsymbol{x} - \boldsymbol{x_i}) \left(-\frac{\hbar^2}{2m} \nabla^2 + V_{\text{lat}}(\boldsymbol{x}) \right) w_0(\boldsymbol{x} - \boldsymbol{x_i}) \mathrm{d}^3 x, \qquad (2.22)$$

where $w_0(\boldsymbol{x})$ is the spatial wave function (a Wannier function, see section 2.2.3), h is Planks constant, m is the bosons mass and V_{lat} is the lattice potential.

The second term in (2.21) is the potential energy at the centre of each lattice site. The finite beam waist of each lattice beam forms an additional trap, as can be seen in fig. 2.6 on page 26. Since the atom cloud in our system only occupies the central lattice sites (<50 in each direction), this effect is negligible (the additional confinement is exaggerated in the figure): $\epsilon_i \approx 0$. This term will be neglected for the rest of this discussion.

The interaction term of (2.21) accounts for the collisional energy represented by having $\hat{n} \equiv \hat{a}^\dagger \hat{a}$ atoms in a common lattice site. The interaction energy U is based on S-wave scattering with scattering length a. For $a > 0$, repulsive ($a < 0$, attractive) interaction, putting another atom into a lattice site already occupied by one atom costs (yields) the energy U:

$$U = \frac{4\pi\hbar^2}{m} a \int |w(\boldsymbol{x})|^4 \mathrm{d}^3 x. \qquad (2.23)$$

The (simplified) Bose-Hubbard Hamiltonian features a balance of two different energies, the tunnelling matrix element J and the interaction energy U. Depending on which of the two dominates the Hamiltonian, the system will have two very different ground states, the Superfluid (SF) ($J \gg U$) and the Mott-Insulator (MI) ($J \ll U$). The transition from one to the other happens at a critical ratio $(U/J)_c$ (here: 6×5.8 [62–65], also: 1D, $\langle \hat{n} \rangle = 1$: 3.84 [66]), at which the system will undergo a quantum phase transition from one state to the other [67].
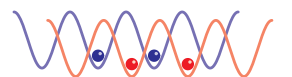
The Superfluid

For $J \gg U$ the system is dominated by tunnelling, interaction is negligible. This leads to a situation where the state of each of the N atoms is spread out over all M lattice sites:

$$|\Psi\rangle \propto \left(\sum_{i=0}^{M} \hat{a}_i^\dagger \right)^N |0\rangle \tag{2.24}$$

After factoring out and observing only one lattice site, this state can be approximated as a coherent state [68, 69]. This is the quantum mechanical description for classical or semi-classical oscillators. A coherent state $|\alpha\rangle$ is defined by its macroscopic amplitude $\alpha \equiv \langle \hat{a} \rangle$. It can be written as:

$$|\alpha\rangle = e^{-|\alpha|^2/2} \sum_{n=0}^{\infty} \frac{\alpha^n}{\sqrt{n!}} |n\rangle. \tag{2.25}$$

A coherent state is thus composed of atom number states $|n\rangle$ following a Poissonian number distribution. While the atom number at a lattice site is not well determined, the state is an eigenstate of the annihilation operator, and thus its macroscopic phase $\arg(\langle \hat{a} \rangle)$ is well defined and can be measured compared to a standard phase [70]. It is this macroscopic phase that allows the wave functions from different lattice sites to interfere with each other during a TOF sequence.

The Mott Insulator

If $J \ll U$ the system is dominated by interactions, tunnelling is negligible. In this case, each of the N atoms is localized to one of the M lattice sites:

$$|\Psi\rangle \propto \prod_{i=0}^{M} \left(\hat{a}_i^\dagger \right)^{N/M} |0\rangle \tag{2.26}$$

This is a single atom number state or Fock state, the atom number is well defined. There is no defined macroscopic phase, as $\langle \hat{a} \rangle = 0$. Without a macroscopic phase, the TOF will not lead to a multiple matter-wave interference pattern, but it will just show the incoherent sum of all Gaussian wave packets.

2.3.2. Realization in our Experiment

In section 2.2.2 the basic setup of the optical lattice was shown. A few additions need to be made, though: A 3D lattice in which three 1D lattices are overlapped without any further precautions cannot be stable. If the polarisations of two such lattice beams match partially, this gives rise to interference between beams from different axes, which creates a superstructure on top of the simple lattice potential. In the extreme case of identical polarisation, every second potential well in the lattice is missing. The result of a configuration with partial interference for a Superfluid (SF) lattice is shown in fig. 2.12.

The obvious solution, to use mutually perpendicular polarisations on all three laser beams reduces this effect strongly, but not perfectly. The polarisation of the lattice beams is not defined to better than 1:1000 due to imperfect polarization cubes. The remaining interference between different axis is enough to change the phase of the wave functions of adjacent lattice wells and to create undesirable fluctuations.

To overcome this residual unwanted interference, the laser beams for
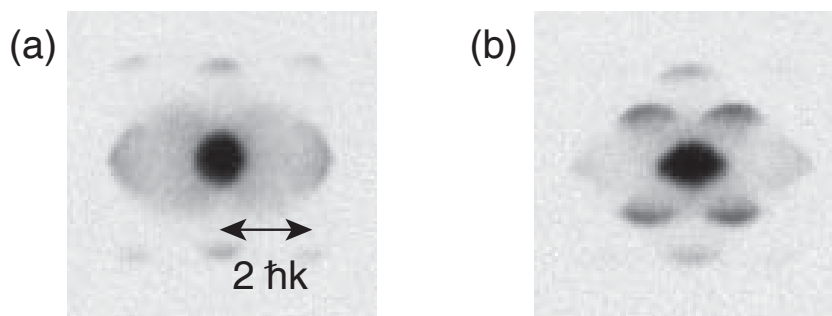
**Figure 2.12.:** Results of interference between different lattice axes. The two lasers that form this 2D lattice interfere with each other and this modulates the depths of the lattice sites. **(a)** Here the modulation is small, showing the interference of a simple-cubic lattice. The distance $2\hbar k$ to the first interference peak is marked in the picture. **(b)** The interference caused every second lattice site do be weaker then its neighbours in this picture. The result is that the system behaves as if it was a tilted lattice with a larger lattice constant, so the reciprocal lattice becomes narrower. The lattice depth was $12\,E_R$ and the images are taken after a TOF of $12\,$ms.
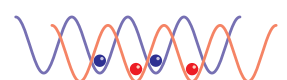
different axes have different optical frequencies with a difference $\delta f > 20\,\mathrm{MHz}$. The interference structures therefore oscillate much faster than the trapping frequency $\delta f \gg \omega_{\mathrm{trap}}$. For the atoms the interference is therefore time-averaged and only the simple lattice remains.

The lattice is loaded with a Mott Insulator by increasing the beam intensity on all three axes in a 80 ms exponential ramp with a 20 ms time-scale [71]. Images taken after loading into lattices of different depths are shown in fig. 2.13. During the loading process, the system starts from a superfluid BEC in a single trap and then becomes distributed over the 3D lattice. For a SF, the TOF shows the reciprocal lattice in a matter-wave interference pattern. The smaller the interference peaks, the larger the coherence length over the lattice. For lattice depths above $U_{\mathrm{lat}} \approx 13\,\mathrm{E_R}$, the system undergoes the phase transition to the MI state. The lattice sites are filled with Fock states now that have no defined phase any more. Opposed to the Superfluid, in this phase the atom number is certain and the phase is undefined. Without a fixed phase relation, the matter waves of different lattice sites can not interfere constructively. Any two lattice sites will have a different interference pattern and the average over all shows only the Gaussian envelope distribution.

Both the Superfluid and the Mott-Insulator are ground states for their respective lattice strengths. The ramp-time given above should allow for
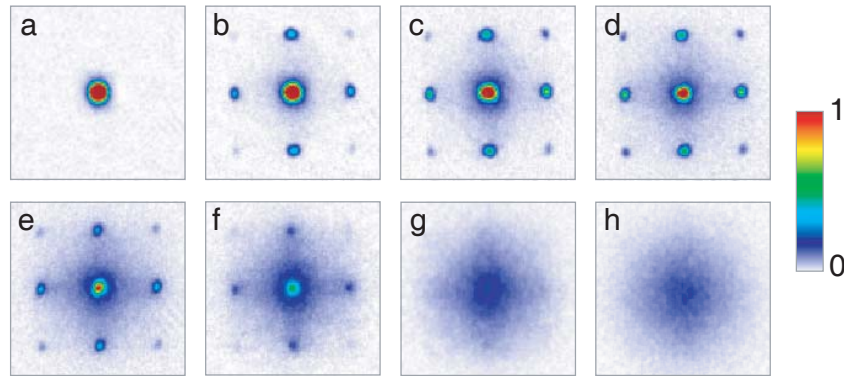

Figure 2.13.: Mott insulator being formed. The atom cloud is shown from the BEC **(a)**, over the stage of superfluid lattices **(b)-(e)** up to the phase-space transition **(f)** into the Mott-Insulator **(g)-(h)**. The absorption images are taken after a TOF of 15 ms. The lattice depth for the images is: **(a)** $0\,\mathrm{E_R}$, **(b)** $3\,\mathrm{E_R}$, **(c)** $7\,\mathrm{E_R}$, **(d)** $10\,\mathrm{E_R}$, **(e)** $13\,\mathrm{E_R}$, **(f)** $14\,\mathrm{E_R}$, **(g)** $16\,\mathrm{E_R}$, **(h)** $20\,\mathrm{E_R}$.

an adiabatic transition from one to the other. So it has to be possible to drive the phase transition in both directions: by lowering the lattice strength slow enough from the MI regime, the system should evolve into the Superfluid phase. This experiment can also be used to distinguish the creation of a Mott-Insulator from a dephased or excited sample: Both show the same behaviour after a simple TOF expansion from the deep lattice, but only the MI is a ground state and can be transferred back to the SF phase. In the experiment, the lattice is ramped as shown in fig. 2.14. The ramp-down time is varied to measure the formation time of the new ground state. The TOF is done from a lattice depth of $9\,E_R$.

The more lattice sites are populated with a coherent state and take part in an interference, the narrower the interference peak will be. Therefore, the width of the central peak in the reciprocal lattice is taken as a measure for coherence. The results together with the widths from an intentionally dephased control experiment are shown in fig. 2.15 on the following page. While a SF forms for the MI, the intentionally dephased samples do not show any signs of a superfluid interference pattern. So the SF is not formed after recondensation from an excited state.

2.4. Coherence of Collisions

Cold collisions are, for bosons, S-wave collisions described by the collision length a. All other partial waves have a non-vanishing angular
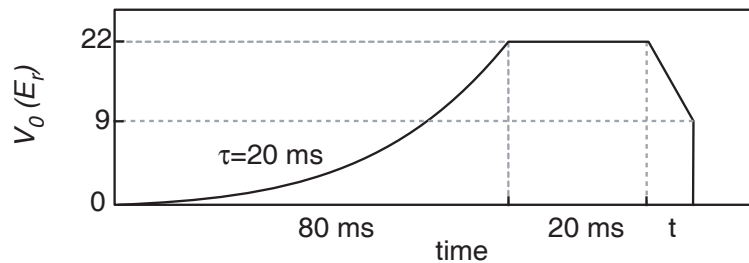
Figure 2.14.: Lattice-ramp used for reverting the Mott phase-transition. The lattice-depth (shown in E_R)is varied over time: In the first 80 ms, the Mott Insulator is created and given 20 ms to stabilize. Then in a variable time t, the lattice is ramped down to a low depth after which the trap is switched off and after a TOF the momentum distribution of the atom cloud is measured.
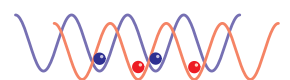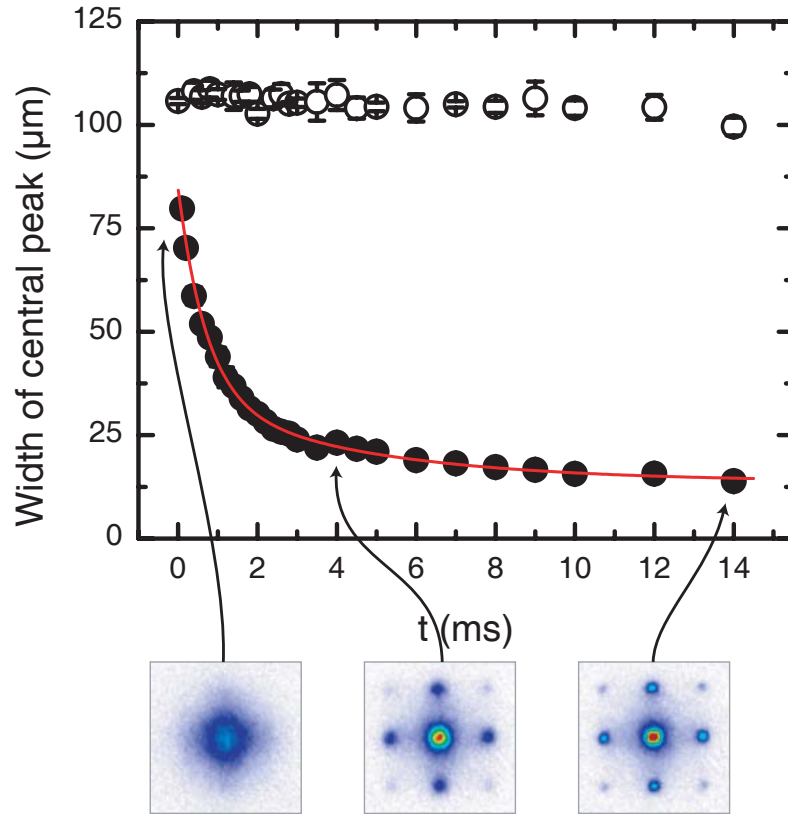
Figure 2.15.: Reappearance of phase-coherence after a phase-transition from a Mott insulator. The graph shows the width of the central interference peak versus the ramp down time t of the lattice. The more lattice sites are coherently adding to the interference, the smaller the interference pattern is. The filled circles correspond to an initial **BEC** that was transferred into the **MI** state and from there back into a superfluid. The solid line is a fit using a double exponential decay ($\tau = 0.94$ ms and $\tau = 10$ ms). For the empty circles, the phase of the initial **SF** was scrambled before reaching the **MI** state. The images show example interference pattern for t=0.1 ms, 4 ms, 14 ms.

momentum. It requires more energy to bring two atoms together during the collision, if there is a centrifugal barrier to overcome (see e.g. [72, 73]). The S-wave collision is described as a phase shift of the two-particle wave function. As there is only this operation on the wave function, a series of many collisions can be described by just one phase evolution, proportional to the interaction time or number of occurred collisions. For ultracold bosons, two-body collisions do not lead to decoherence or losses, but are coherent.

In BECs, collisions are described by the mean field interaction. The granular atomic collisions are a much better description in the few atom regime of one lattice site. One difference of this granular description of interaction opposed to mean field interaction is the collapse and revival of the macroscopic matter-wave-state [74–80] that is driven by atomic collisions.

A harmonic trap is prepared with a coherent atomic state, i.e. a BEC is loaded into a shallow 3D lattice. The coherent state (2.25) is a superposition of Fock states. The eigenenergy of a Fock state is given by the collisional energy of its constituting atoms, $E_n = \frac{1}{2}Un(n-1)$. Here U is the collisional energy of a single atom-pair in the trap, see (2.23). As the coherent state is a superposition of states with different eigenenergies, it features a time-evolution:

$$|\alpha\rangle(t) = e^{-|\alpha|^2/2} \sum_n \frac{\alpha^n}{\sqrt{n!}} e^{-i\frac{1}{2}Un(n-1)t/\hbar} |n\rangle \qquad (2.27)$$

The individual terms in the sum will evolve apart with increasing time, as all the exponentials run at a different frequency $\propto n(n-1)$. The state therefore evolves away from a coherent state, which can be seen e.g. by performing a phase-measuring interference experiment on the state. If the state is not coherent, it has no defined phase and repeated measuring would give an average of $\langle \hat{a} \rangle \to 0$. The case of a coherent state as shown in (2.27) evolving over time is shown in fig. 2.16 on the next page, where the overlap of $\langle \beta | \alpha(t) \rangle$ is plotted. The state $|\beta\rangle \equiv |A, \varphi\rangle$ is a coherent state with the amplitude A and phase φ. During the time-evolution, the initially coherent state is smeared out to a ring in the phase diagram, with a defined amplitude, but uncertain phase. At the time of the collapse, the state has evolved into a superposition of two coherent states $180°$ out of phase. The average phase $\langle \hat{a} \rangle$ is nearly zero.

Later on, the original state is recovered at the revival time $t_{\text{rev}} \equiv h/U$. The argument to the time-dependant exponential in (2.27) shows, why: for $t = t_{\text{rev}}$, it becomes $-i2\pi(\frac{1}{2}n(n-1))$, so the exponential vanishes for
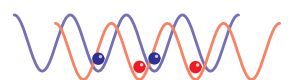
integer n. If n were continuous like in the Jaynes-Cummings model for an atom in a resonator, the revival would be only partial, as the exponential only vanishes for $t = 0$.

In the experiment [12], a coherent state is prepared in each of the lattice-sites and then tunnelling between sites is suppressed by ramping up the lattice (see fig. 2.17 on the facing page). The difference to creating a MI phase is the time scale for going from the shallow to the deep lattice. While in the experiment described in section 2.3.2 the ramp is slow to allow an adiabatic phase transition, the ramp is much faster here so that the system has no time to evolve to the new ground state. The atom-number distribution in each lattice site is still Poissonian as for the SF. The ramp time has to be fast compared to the tunnelling time, but still slow compared to the trapping frequency in each lattice site. Otherwise, excitations from the trap ground state into higher trap states would occur.

The system is allowed to evolve for a variable time t, after which all potentials are switched off and the atom cloud expands freely. The interference pattern characteristic for the SF forms for $t = 0$, because each
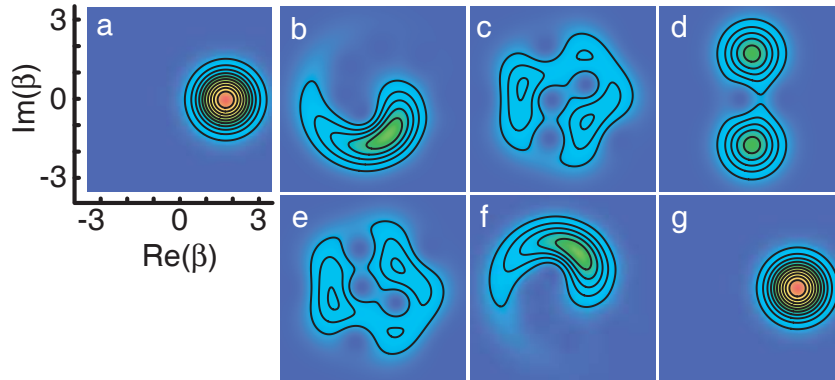
Figure 2.16.: Evolution of a coherent state. The overlap of the coherent state $|\alpha(t)\rangle$ with a test-state $|\beta\rangle$ is shown in a phase space plot. The images show the time-evolution for the times (**a**) $t = 0\,t_{\mathrm{rev}}$, (**b**) $0.1\,t_{\mathrm{rev}}$, (**c**) $0.4\,t_{\mathrm{rev}}$, (**d**) $0.5\,t_{\mathrm{rev}}$, (**e**) $0.6\,t_{\mathrm{rev}}$, (**f**) $0.9\,t_{\mathrm{rev}}$, (**g**) $1\,t_{\mathrm{rev}}$. The individual terms in the sum in (2.25) evolve with different speed and the state is smeared out in the process (**a-c**). At the time of maximum collapse, $|\alpha\rangle$ behaves as a cat-state of two coherent states with exactly opposite phase (**d**). The evolution of $|\alpha\rangle$ then brings all constituents of it together again (**e-g**).
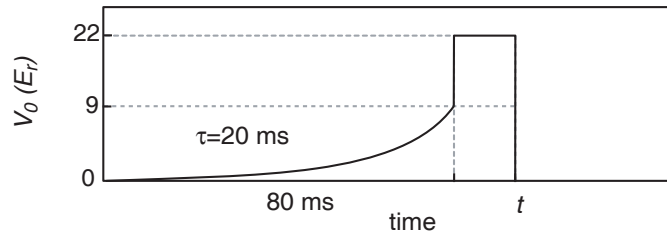
Figure 2.17.: Experimental ramp for the collapse and revival. Shown is the lattice depth in E_R versus time. After a superfluid lattice is loaded, the well height is increased fast and the system evolves with no tunnelling for a variable time t. After that, the trap is switched off and an absorption image is taken after a TOF.

lattice site is superfluid, i.e. each lattice site contains a coherent state. The interference pattern is therefore used to measure the number of atoms in a coherent state N_{coh}.

The coherent fraction of the total atom number N_{coh}/N_{tot} is plotted versus time in fig. 2.18 on the next page. While the system is initially superfluid, the $|\alpha\rangle$ state in each lattice site collapses in its time evolution. At $\frac{1}{2}t_{rev}$ the interference is minimal, showing no remaining coherent state in the system. After that the superfluid state revives to nearly the initial coherence. The system undergoes the collapse and revival cycle five times, before no interference structure can be seen in the images any more.

The interference pattern in the graph is reduced for each cycle. There are several reasons for this:

- The jump, that isolates the individual lattice sites from each other, also causes a compression of the lattice sites. As the atoms cannot redistribute to accommodate, this results in a non-flat chemical potential. This causes a slow broadening of the interference peaks, that introduces errors with our measuring technique of the atom number of the coherent state.

- The density in the lattice sites near the trap centre is slightly larger than for sites near the border of the trap. The collisional energy U is dependant on the density and therefore the revival time t_{rev} is different across the lattice.

The phase-evolution of the individual Fock states $|n\rangle$ depends on the
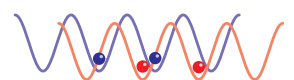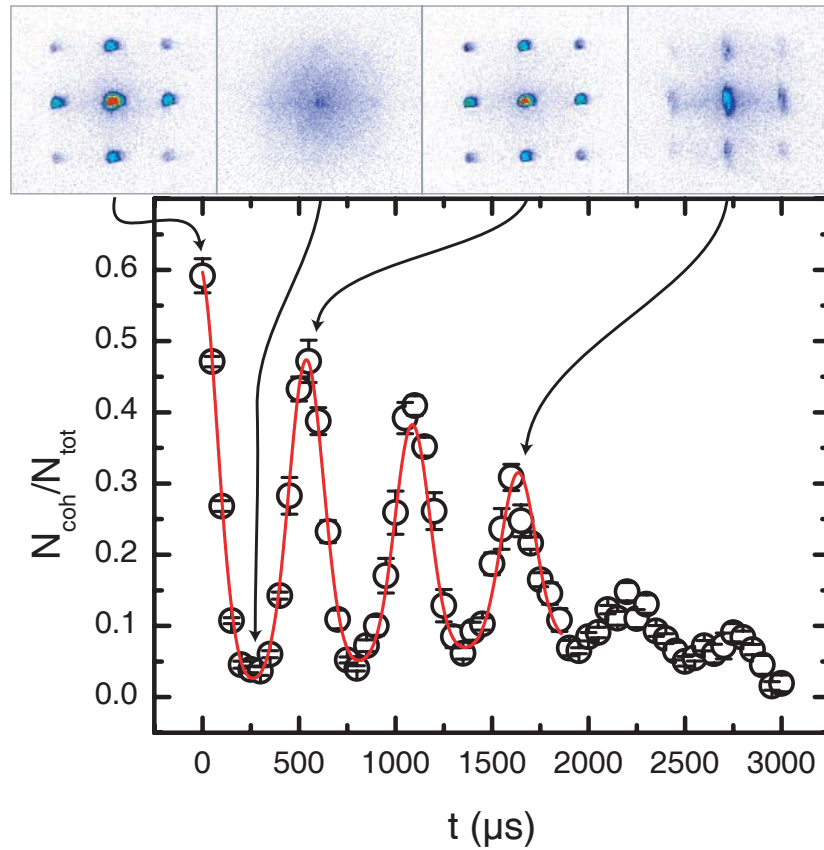
Figure 2.18.: Collapse and revival of a macroscopic matter wave. The fraction of atoms in the interference pattern is plotted over evolution time t. Shown are also example images images of the first cycle and one showing the degradation of the interference later on.

interaction energy U, which is itself dependant on the spatial wave function $w_0(\boldsymbol{x})$. Increasing the lattice-depth compresses the spatial wave function of each lattice site and therefore finally accelerates the phase evolution of the individual Fock states. A measurement, where the lattice depth of the plateau in fig. 2.17 on page 41 is changed and the revival time is measured, is shown in fig. 2.19. As $t_{\mathrm{rev}} \propto 1/U$, not the revival time but the revival frequency is plotted.

In the publication [81] (see also page 97), there is also a discussion about the effects of squeezing of the coherent state on the collapse time. As in the next chapter the properties of squeezed states are not needed, this part is skipped here and the interested reader is referred to the publication.
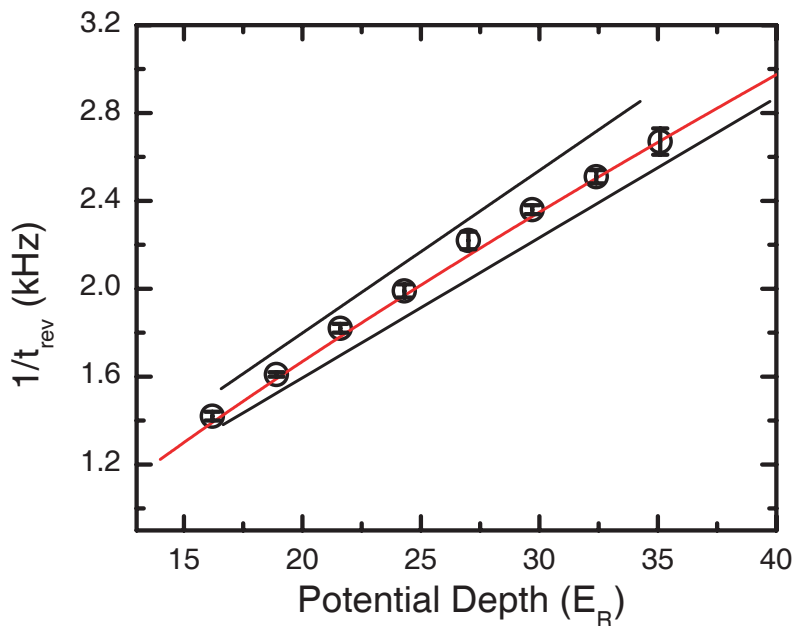
Figure 2.19.: Revival frequency as a function of lattice depth. The points and the red curve are the measured data together with a linear fit. The black curves mark an a priori range of expected results.
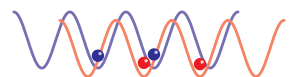
3. Quantum Gates in Spin-Dependant Lattices

Like normal computers, quantum computers work with an inner representation of the data. In a quantum computer the basic representation of information are quantum mechanical states like spins ('qubits'). The computation gates between different elements are linear in each of their input states, i.e. if one of the inputs of a gate is a superposition state, then the output is the superposition of the results of each of the inputs. Apart from applications in simulating quantum-mechanical systems, there exist also algorithms for other problems that cannot be solved polynomially with a classical computer, but they can with a quantum computer [82].

For building a quantum computer, one cannot simply take a classical computer design, replace the information carrier by a quantum mechanical state and call it a quantum computer. Things that go without saying in classical computing have proven to be quite difficult to realize in quantum computers. Optical lattices have been proposed as a means to realize quantum computers [83–86]. The motivation for this proposal becomes apparent if one takes a look a the list of requirements [87] on a system for it to be usable for quantum computing:

1. A scalable physical system with well characterized qubits

2. The ability to initialize the state of the qubits to a single basis state, such as $|000\dots\rangle$

3. Long relevant coherence times, much longer than the gate operation time

4. A "universal" set of quantum gates

5. A qubit-specific measurement capability (i.e. single qubit detection)

Of these the Mott-Insulator (MI), i.e. a regular lattice of ultracold atoms, already fulfils two: The system consists of multi-level atoms where two easily addressable states can be selected to represent the qubit. The number of atoms scales as the volume of the system. In fact, this setup is the
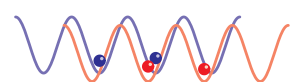
largest collection of isolated qubits realised experimentally, apart from solid state systems. And the system is already initialized to a single state, after loading the lattice with atoms.

Only two points in the list are not yet solved: the coherence time is at the moment on the order of few gate times. There are suggestions on how to use decoherence-free sub-states to improve on this [88]. And individual addressing of qubits is not implemented in our apparatus, though at least a destructive measurement of individual sites should be possible with field gradients and better imaging optics. For a CO_2 lattice this is even possible without a field gradient [89]. Even with the current state of the system, a quantum simulator along the original ideas of Feynman seems feasible (see also chapter 4).

In this chapter, a quantum gate in the lattice is presented that together with the one-particle spin-rotations forms a set of universal quantum gates. The gate is based on a technique to controllably shift and delocalise atoms in the lattice. Several characterisation experiments show the quality of this delocalisation-operation. Based on that, an experimental sequence using the quantum gates is presented, that builds up entanglement in the lattice. The process can entangle a large number of qubits in parallel, limited only by the quality and dimensions of the occupied lattice sites. But first, a short introduction to quantum information processing:

3.1. Classical vs. Quantum Information

In 'classical' computing, a *bit* is the smallest unit of information, having only the two states 0 and 1. Information is encoded by forming binary numbers of arbitrary length, usually multiples of 8 bit. Calculations with this basis are implemented on algorithmic computers, that work on few of these numbers at a time, building up the result of a calculation in small, discrete steps. This makes the system so very versatile and reproducible.

Quantum physical problems on the other hand often are not confined to single basis states, but any superposition of basis states is possible. Hence, a problem with n spin-$\frac{1}{2}$ particles generally needs to be described in a vector-space of size 2^n. Here each of the possible configurations for the individual spins is a separate base-vector. For example, a $2 \times \text{spin}\frac{1}{2}$ system could look like:

$$|\downarrow\rangle|\uparrow\rangle \equiv |0\rangle|1\rangle : \begin{pmatrix} 0 \\ 1 \\ 0 \\ 0 \end{pmatrix}$$
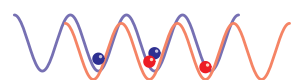
$$\frac{1}{\sqrt{2}}(|0\rangle|1\rangle + |1\rangle|0\rangle) : \frac{1}{\sqrt{2}} \begin{pmatrix} 0 \\ 1 \\ 1 \\ 0 \end{pmatrix}.$$

Even for a small number of spins, a problem containing entanglement or superposition of states can only be computed using simplifying approximations. Here, the qubit is a much more natural unit of information. A qubit can be any superposition state of $|0\rangle$ and $|1\rangle$ and any quantum mechanical spin-$\frac{1}{2}$ system can represent a qubit. The concept of a qubit helps generalize algorithms and results for different realisations of the quantum information.

This same superposition principle can also be used to solve mathematical problems very efficiently: given a n-qubit operation, initialize each input-qubit in a superposition of $|0\rangle$ and $|1\rangle$. Expanding the input state, one finds that it is a superposition of all 2^n possible bit-combinations. When the operation is then run, it produces in just one run a superposition of all possible outputs. Applying an appropriate filter to this output, e.g. projection on a certain sub-space, speeds up the numerical inversion of a mathematical operation immensely. Generally, many operations, that require an exhaustive search on classical computers to solve, are good candidates for implementation on a classical computer.

3.2. Optical Lattices as a Basis for Quantum Information

In our system of a MI stored in an optical lattice, each qubit is represented by one atom. For atoms, the dominant interaction is collisions. To suppress uncontrolled collisions, the atoms are held isolated from each other in different sites of the optical lattice. In the MI, the deep lattice suppresses tunnelling, hence the qubit cannot move or delocalise. The lattice is detuned from the atomic resonance to suppress incoherent scattering of lattice photons. This allows for a mean trap lifetime of few hundred mil-

liseconds to a few seconds, depending on the exact detuning and strength of the lattice laser beams.

Another strong point of using a MI for the basic preparation of our system of isolated single atoms is the initial absence of vacancies in the lattice, as would be present in a loading from a dilute gas. There, the density would have to be reduced, until the *probability* of two atoms occupying the same lattice site is small. This would on the other hand cause a lot of vacancies.

3.2.1. Spin-Dependant Lattices

In order to perform any operations on the trapped qubits, the corresponding qubits have to be brought into interaction. In a system with individually addressable atoms, a light-induced interaction could have been used. There the qubit is transferred from one atom to a photon and this photon then interacts with a second atom via a High-Q cavity. Apart from the facts, that the probability for loosing the photon and with it the qubit is quite large, this process does not scale to higher qubit-numbers. There has also been spin-dependant tunnelling observed [90].

Instead, the atoms are physically shifted from one lattice site to another, to interact with the atom in that trap. This technique was proposed by Dieter Jaksch *et al.* [9]. In the centre of the optical lattice, each lattice site is filled with exactly one atom, initialized by the creation of a MI. The atoms each carry a qubit encoded by the population in two of the magnetic sub-levels of the atomic groundstate. These states are chosen such that they interact differently with lattice-light of different circular polarisations. We call the optical lattice-axis that the shift happens along the *x*-axis or shifting-axis.

Consider the fine-structure of a ^{87}Rb-atom in fig. 3.1 on the facing page. The lattice-laser is detuned between the D1- and D2-line of the atom, so that the lattice is attractive with respect to the D2-line, but repulsive with respect to the D1-line. For circular polarised light, there are two possible transitions for each of the ground-states. One of those ends with the atom in $m_j' = \mp\frac{1}{2}$ for $m_j = \pm\frac{1}{2}$. The optical dipole trap caused by these transitions is the sum of a blue- and a red-detuned dipole trap, and for the right detuning, for ^{87}Rb at 785 nm, these cancel out leaving no trap. The other transition goes to $m_j' = \pm\frac{3}{2}$ where a red-detuned lattice is formed, as there is no D1-line state to provide a blue-detuned 'compensation'-lattice.

The wavelength at which the blue and red components of the dipole-trap cancel can be calculated using (2.11). Here the transition-coefficients
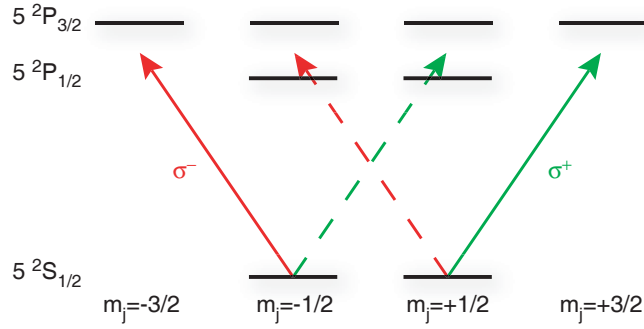
Figure 3.1.: The ^{87}Rb Finestructure for the D1 and D2 lines with $\sigma^{\pm}$ light of the *x*-lattice. Only the solid transitions provide a dipole force, for the dashed ones the contribution from the D1 line cancels out the contribution from the D2 line.

c_{ij} can be expressed in terms of $3j$ symbols, with a renaming of the states $i \rightarrow j = \frac{1}{2}, m_j = \pm\frac{1}{2}$ and $j \rightarrow j', m_j'$ (please note the difference between j and j):

$$c_{j,m_j,j',m_j'} = (-1)^{-j+1-m_j'}\sqrt{2j'+1}\begin{pmatrix} j & 1 & j' \\ m_j & q & -m_j' \end{pmatrix}. \tag{3.1}$$

Here q is the polarisation of the incident light: $q = \pm 1$ for $\sigma^{\pm}$ circular polarized light, $q = 0$ for linear polarized light. When $m_j' = m_j + q$ is fixed, the sum in (2.11) is over $j = \frac{1}{2}, \frac{3}{2}$ only. The resulting expression for ΔE is set to zero and solved for the wavelength. Due to symmetry arguments, $\Delta E_{j,m_j}(q) = \Delta E_{j,-m_j}(-q)$. Figure 3.2 on the next page shows the potential as a function of wavelength λ.

For an atom with only Fine-structure splitting, two circular polarized lattices form the spin-dependent lattice described above. In ^{87}Rb with its nuclear spin $I = \frac{3}{2}$, the atoms show Hyperfine-structure splitting. Each state in this new basis $|f\rangle$ can be written as the sum of the Fine-structure basis states $|j\rangle$, using the respective Clebsch-Gordan coefficients
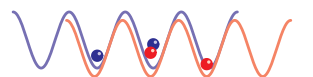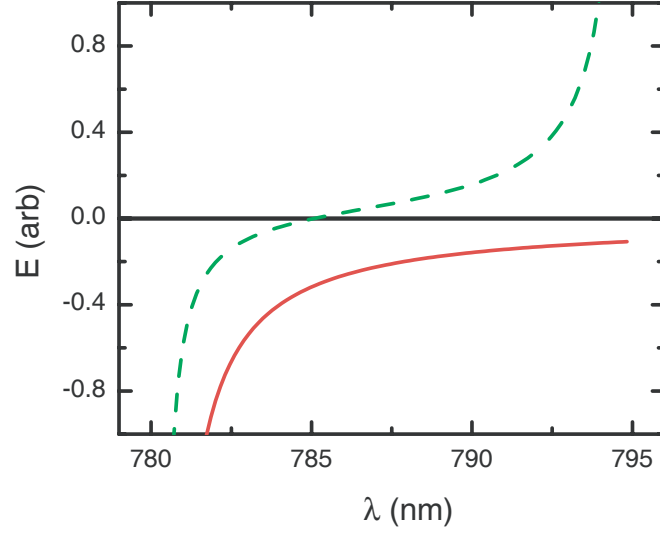
Figure 3.2.: Dipole potential as a function of wavelength. The potential depth for the $|j = \frac{1}{2}, m_j = +\frac{1}{2}\rangle$ state is shown in arbitrary units, the red curve is for σ^- polarized light, the green dashed curve for σ^+ polarization. The resonances for ^{87}Rb are at 780 nm, where both polarisations create an attractive potential and 795 nm that is not affecting a σ^- dipole trap but where a σ^+ dipole trap becomes repulsive. At 785.09 nm the σ^+ dipole trap vanishes.

$C\,{}^{1/2}_{-1/2}\,{}^{3/2}_{-3/2}\,{}^{2}_{-2} = \sqrt{1}$ and $C\,{}^{1/2}_{-1/2}\,{}^{3/2}_{-1/2}\,{}^{1}_{-1} = -\sqrt{\tfrac{1}{4}}$, $C\,{}^{1/2}_{+1/2}\,{}^{3/2}_{-3/2}\,{}^{1}_{-1} = \sqrt{\tfrac{3}{4}}$:

$$|F = 2, m_F = -2\rangle = 1|j = \tfrac{1}{2}, m_j = -\tfrac{1}{2}\rangle \tag{3.2a}$$

$$|F = 1, m_F = -1\rangle = \frac{1}{4}|j = \tfrac{1}{2}, m_j = -\tfrac{1}{2}\rangle$$

$$+ \frac{3}{4}|j = \tfrac{1}{2}, m_j = +\tfrac{1}{2}\rangle \tag{3.2b}$$

While the extremal state $|1\rangle \equiv |F = 2, m_F = -2\rangle$ consists only of one Fine-structure state which is only acted upon by σ^--light, the $|0\rangle \equiv |F = 1, m_F = -1\rangle$ state contains both Fine-structure states, and thus lattices of both polarisations trap it. The potential created by σ^+-polarized light is dominant, though, and the two states do experience different lattices.

The two lattices of σ^+ and σ^- polarized light can be decomposed into two linear polarized beams. A linear polarized beam is the superposi-

tion of two σ-polarized beams, the linear polarisation-axis defined by the phase between the two polarisations. The angle of the linear polarisation thus controls the separation between the $\sigma^{\pm}$ lattices. In our setup, the angle is controlled by an Electro-Optical Modulator (EOM), that works together with a fixed $\lambda/4$ wave-plate to shift the two σ-polarized lattices with respect to each other. The optical setup is detailed in section 3.2.2 and a theoretical description of the potential can be found in appendix A.1.

When initially the lattices coincide and an atom of either $|0\rangle$ or $|1\rangle$ state is stored in a lattice site, shifting the lattices with respect to each other drags the trapped atom along. But if the atom is in a superposition of the two states, then it is either in state $|0\rangle$ trapped in the σ^{+}-lattice or in state $|1\rangle$ in the σ^{-}-lattice. Shifting the lattices apart then delocalises the atom over the two separate lattices.

3.2.2. Optics

The optical setup of a normal lattice axis that does not allow a spin-dependant shifting has been shown in fig. 2.7 on page 27. There the lattice light is superimposed with the imaging light using polarising beam splitter cubes. In the spin-dependant lattice with the polarisation of one lattice beam freely rotatable a polarising beam splitter cannot be used, though. During the use of the spin-dependant lattice, no camera is available on this axis.

Figure 3.3 on the next page shows the optical setup of the shifting axis starting from the experiment chamber **(a)**. The lattice light is focussed onto the atom cloud and lens **(b)** is used to collimate the beam again. After the EOM setup the retro-reflecting mirror **(f,g)** creates the back-reflection and thus the standing wave. The additional lens **(f)** is needed to compensate for the beginning divergence of the laser beam after it was last collimated by **(b)**.

The elements **(c)**,**(d)** and **(e)** are used to turn the polarisation of the reflected beam. The wave plate **(c)** is oriented with one of its axes along the polarisation axis of the incident beam, thus not changing its polarisation (yet). After that follows an EOM **(e)** with the two axes oriented under $45\,^{\circ}$ with respect to the incident beam. The EOM needs to be turned to adjust this angle. For a more stable setup, not the EOM but the polarisation of the beam is rotated using the $\lambda/2$-wave plate **(d)**. In the EOM, decompose the incident polarisation into the $\pm 45°$-basis, giving two new beams with rotated polarisations. Then the phase between these two is varied using
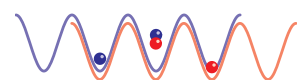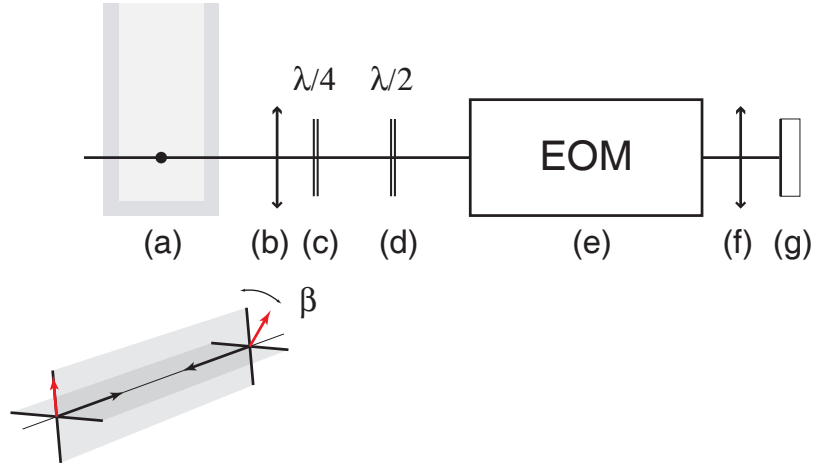
Figure 3.3.: Schematic of the setup for the shifting lattice axis. For a description of the labels, see the text. The inset below the schematic shows the polarisations of the lin-angle-lin lattice at the position of the atom cloud.

the applied voltage. After the reflection on the mirror, the phase-shift is repeated in the EOM, doubling the phase difference. When the laser hits the $\lambda/4$-wave plate **(c)**, it is comprised of two linear polarized beams with a variable phase between them. The wave plate transforms this into two σ-polarized beams with a relative phase given by the EOM phase shift. It is this same phase that is also present in the interference pattern of the two lattices. In a way the optical path length in the EOM directly controls the shifting of the two lattices. Another way to describe this lattice configuration is to rewrite the reflected beam into a linear beam tilted by a variable angle β with respect to the incident beam (hence the name 'lin-angle-lin' lattice). This lin-angle-lin configuration is then converted back into its circular constituents when considering the effect on the atoms.

3.2.3. Single-Particle Operations on a Qubit

As described above, the two base states of a qubit are represented in our ^{87}Rb-atoms by

$$|0\rangle \equiv |F = 1, m_F = -1\rangle \tag{3.3a}$$
$$|1\rangle \equiv |F = 2, m_F = -2\rangle. \tag{3.3b}$$

The MI state is initially prepared with all atoms in the $|0\rangle$ state. The $|1\rangle$ state is populated in our experiment with a microwave pulse of variable length and phase. The microwave frequency is ≈ 6.8 GHz. The Rabi-oscillation [91] driven by the microwave transforms the initial state $|0\rangle$ in a time t to

$$|\psi(t)\rangle = \cos(\Omega_R t)|0\rangle + \sin(\Omega_R t)|1\rangle. \tag{3.4}$$

Pulses are conveniently named after the angle $\Omega_R t$, most common are $\pi/2$- and π-pulses. While a $\pi/2$-pulse prepares (starting from $|0\rangle$) the superposition state $(|0\rangle + |1\rangle)/\sqrt{2}$, a π-pulse exchanges the states $|0\rangle$ and $|1\rangle$.

For this to work reliably, the Rabi-frequency Ω_R needs to be constant at different positions of the trap and for different runs of the experiment. This means, that the sample has to be brought into a homogeneous, well known magnetic field. The sensitivity of the transition-frequency to magnetic field fluctuations can be read from the level scheme (fig. 3.4) to be

$$((g_F m_F)_{\text{final}} - (g_F m_F)_{\text{initial}})\mu_B = -\frac{3}{2}\mu_B \approx -2.1 \frac{\text{MHz}}{\text{Gauss}}. \tag{3.5}$$

As a rough estimate, for a coherence time of $100\,\mu s$, the magnetic field should fluctuate less than $2/(3\mu_B 100\,\mu s) \approx 5$ mG.

To fulfil these requirements, the atoms are not stored in a magnetic trap, as the inhomogeneity of the magnetic field would reduce the coherence time. The only trap the atoms are held in is the optical lattice potential. On the other hand a non-zero magnetic field is required to define the quantization axis of the setup. To control fluctuations of the magnetic field, an active stabilization was chosen, that continuously measures the magnetic
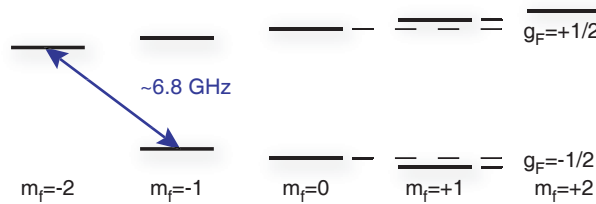
Figure 3.4.: The ^{87}Rb ground state showing the microwave coupling. The g_F factors for F=2 and F=1 are also marked in the sketch.
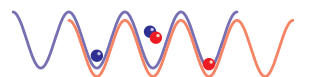
field at a point close to the atom cloud and drives compensation coils accordingly. The magnetic field component in the shifting axis (*x*-axis) is actively stabilized to a constant field of 1 G. The other field components are manually tuned to zero field. The magnetic field fluctuations can be reduced by the active stabilisation from ≈ 10 mG to ≈ 1.7 mG over several runs of the experiment. The short term stability is even better than this.

The field instability results in an uncertainty of the transition frequency of $\delta f \approx 3.4$ kHz or a coherence time on the order of 300 μs. As the short term stability is high compared to this, a spin-echo sequence [92] should lead to much longer coherence times. In a spin-echo sequence a constant detuning from resonance, be it due to stray magnetic fields or spatial inhomogeneity, can be compensated for. After the system has been subjected to the unknown detuning, the superposition of the $|0\rangle$ and $|1\rangle$ states have picked up an unwanted phase. In the spin-echo sequence, the two states are exchanged with a π-pulse after half of the total evolution time. The picked up phase acquires a negative sign in the process. In the second half of the evolution time, the same phase is picked up and cancels with the first phase.

The initial calculation of the expected transition-frequency at a given magnetic field is done using the Breit-Rabi formula:

$$
E = - \left(\frac{h\,\nu_{\mathrm{hfs}}}{2\,(2\,I+1)} \right) + g_{\mathrm{I}}\,h\,\mu_{\mathrm{B}}\,m_{\mathrm{F}}\,B \pm \frac{h\,\nu_{\mathrm{hfs}}}{2} \sqrt{1 + \frac{4\,m_{\mathrm{F}}\,x(B)}{2\,I+1} + x(B)^2},
$$

(3.6)

where I is the nuclear spin, ν_{hfs} is the hyperfine-splitting frequency. For shorthand, $x(B) = \frac{(g_{\mathrm{J}} - g_{\mathrm{I}})\mu_{\mathrm{B}}}{\nu_{\mathrm{hfs}}} B$ and B is the magnetic field applied to the atoms. For F=1, the $\pm$ is a minus, for F=2, it is a plus. The transition frequency is then the difference of the energy of the final state and that of the initial state. The magnetic field dependence of the ^{87}Rb ground states is shown in fig. C.2 on page 110. Please note that if $\left| \frac{4\,m_{\mathrm{F}}}{2\,I+1} \right| = 2$, then the radicand becomes a binomial formula. The square root acts as an absolute value operation, the sign of which is wrong for half of the values. So if in plots of extremal states there is a kink in the line, this is an artefact that has to be removed.

Naturally, the magnetic field is initially not well enough known to give more than an educated guess for the frequency of the transition. A search using frequency-sweeps with decreasing span has to be used to locate a resonance frequency. From that, the exact magnetic field and also the frequencies of all other transitions can be computed.

Once the resonance frequency is determined, the Rabi-frequency and the dephasing time can be measured. Figure 3.5 shows an exemplary Rabi oscillation, where the number of atoms on one state is measured relative to the total atom number. From a damped sine fitted to the data a π-pulse time of t_π=13 μs and a dephasing time $T_\phi \approx$1.6 ms are extracted.

With this information, an interferometer-type Ramsey sequence can be run. Here each qubit is first brought into a superposition of $|0\rangle$ and $|1\rangle$ with a $\pi/2$-pulse. Then the state is allowed to evolve a certain time t_{hold} and finally a second $\pi/2$-pulse reads out the phase ϕ picked up during the evolution. For this purpose, the microwave-phase α of the last $\pi/2$-pulse can be changed. Figure 3.6(a) on the next page shows the measured result in the inset: one period of a sinusoidal function. The visibility of this so called Ramsey-Fringe is fitted and the result for different hold times is plotted in the main part of fig. 3.6(a).

The coherence time of less than 300 μs is certainly not enough for the quantum gate experiments. The dephasing time $T_\phi \approx$1.6 ms for the rabi oscillation is longer, suggesting that the continuous spin-echo effect in a rabi oscillation cancels some of the decoherence effects. Figure 3.6(b) on the following page shows another Ramsey-experiment, where a spin-echo π-pulse was added. One clearly sees the effect of using a spin-echo sequence: the visibility is around 50 % after 3 ms, increasing the coherence time by an order of magnitude.
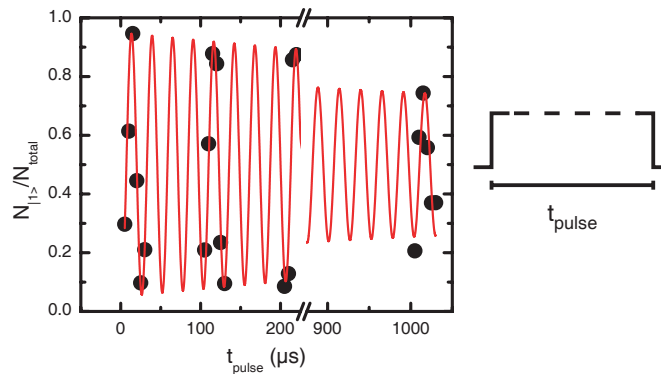
Figure 3.5.: Rabi oscillation measurement. A resonant microwave pulse of length t_{pulse} (as shown in the illustration) transfers the shown fraction of the atoms into the $|1\rangle$ state. The fit is a damped sine with a period of 26 μs and a dampening time of 1.6 ms.
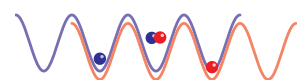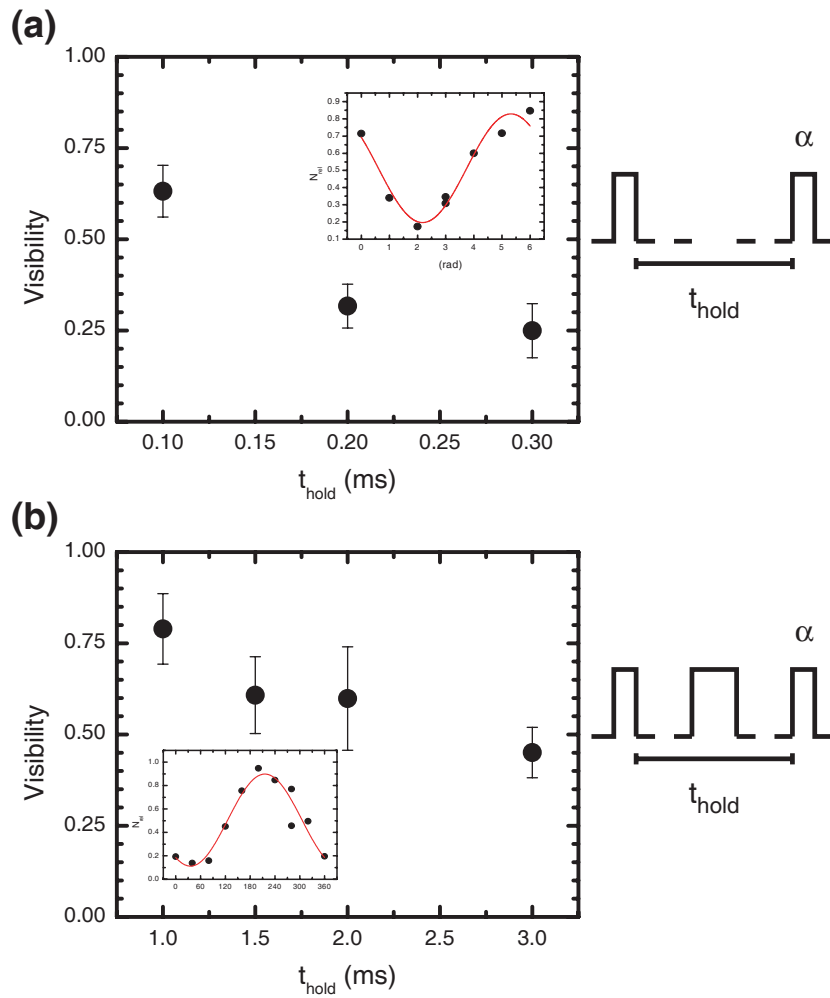
Figure 3.6.: Ramsey sequences demonstrating the effect of spin-
echo. The microwave pulses illustrated on the right hand side
form a Ramsey interferometer sequence and the phase α of
the last $\pi/2$-pulse is varied. The Ramsey-fringe is recorded
for different hold times t_{hold} (see the insets) and the visibil-
ity obtained by fitting to a sine-function is plotted in the main
graphs. **(a)** Without spin-echo, the coherence vanishes in less
than 300 μs. **(b)** With a spin-echo pulse the coherence is still
around 50 % at t_{hold}=3 ms.

3.3. Controlled Qubit-Delocalization over Variable Distances

Up until now, the shifting and delocalisation in the lattice has been studied for next neighbours only. Also, some advanced issues with moving atoms in a lattice have been neglected: the trap-configuration during the shift should be identical for both atomic states. Otherwise an additional, unwanted phase is picked up by the qubits that has to be compensated (if that is even possible). Also there may be no excitation to trap levels other than the groundstate. This would change the interaction term U from (2.23) and the time-evolution of two qubits in contact would not be a single phase-evolution. This chapter describes in detail the characterisation experiments for the shifting process and shows delocalisation over a distance of up to 6 lattice sites.

3.3.1. Trap Depths

For states that couple exclusively to either of the $\sigma^{\pm}$ lattices, the trap depth stays constant for any configuration of the minima of the lattice potentials. But in section 3.2.1 it is shown that the $|0\rangle$ state is sensitive to a sum of σ^{+} and σ^{-} lattice. If these lattices are moved relative to each other, the potential depth is reduced (see fig. 3.7 on the next page):

$$U_0(x, \beta) \propto \frac{1}{4}\cos(kx - \beta/2) + \frac{3}{4}\cos(kx + \beta/2). \qquad (3.7)$$

The lattice-depth for $|0\rangle$ is reduced during the shifting process by a factor of $1/2$. The trapping frequency f relates to the potential depth U as $U \propto f^2$. So the trapping frequency gets reduced by a factor of $1/\sqrt{2}$. This can been measured by preparing the system in either spin-state and then partially shifting the lattices by changing the voltage on the EOM. Then the trap position is modulated around this point with a test frequency and the excitation of the system is measured as the population in higher Brillouin zones (see section 2.2.4). The excitation is maximal for a modulation with the trap-frequency of this atomic state at this point in the shifting sequence. The graph of the trap depth for both spin states is shown in fig. 3.8 on page 59.

This effect can be reduced by changing the relative intensities of σ^{+} and σ^{-} lattices during the shifting process. This modifies (3.7) with a power-
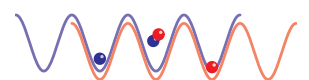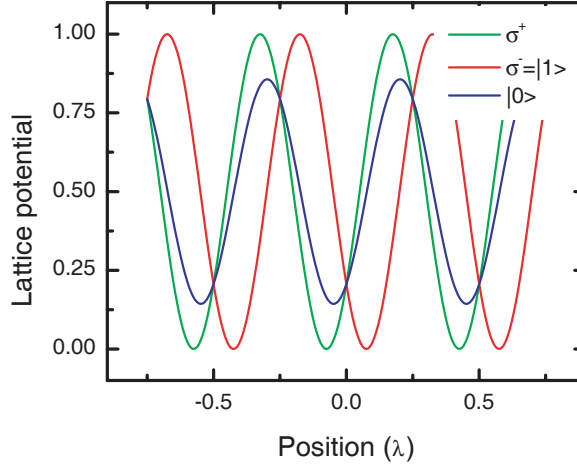
Figure 3.7.: Reduction of the lattice depths during the shifting operation. Shown is the lattice configuration for the $|0\rangle$ atomic state. The σ^- lattice (red) acts only on the Fine structure state $|j = \frac{1}{2}, m_j = -\frac{1}{2}\rangle$ and the σ^+ lattice (green) acts only on the $|j = \frac{1}{2}, m_j = +\frac{1}{2}\rangle$ state. The resulting potential for the Hyperfine structure state $|0\rangle$ is shown in blue.

distribution factor p:

$$U_0(x, \beta) \propto \frac{1-p}{4} \cos(kx - \beta/2) + \frac{3p}{4} \cos(kx + \beta/2). \qquad (3.8)$$

If the strength of the σ^+ lattice is increased during the shifting process ($p > \frac{1}{2}$), then the reduction in the potential depth U_0 can be compensated. On the other hand, this means a reduction in the σ^- lattice intensity and thus a reduced potential U_1. A trade-off has to be found, where the potentials for both spin states changes common mode. This should minimize the excitation into higher bands due to the shift in a lattice of reduced strength.

The redistribution of light between the two lattices is done by turning the EOM out of its exact alignment with respect to the incident polarisation. This results in a variable power distribution dependant on the shifting position: $p(\beta)$. While for $\beta = 0$ the power is equally distributed $p = \frac{1}{2}$, the power asymmetry is maximal for the middle of the shifting cycle (for details, see appendix A.1).

Another issue are traps of unequal groundstate energies: if the two spin states are stored at different energies, they acquire a different phase shift.
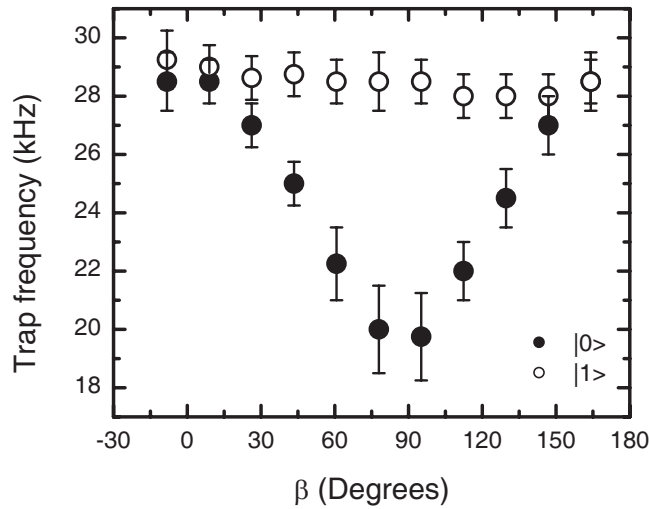
Figure 3.8.: Measured trap frequencies for both atomic states during shifting. The position of the lattice sites in the shifting process are expressed as the angle β in the lin-angle-lin lattice, $\beta=0°$ and $\beta=180°$ are the start and stop points of a lattice shift. The graph was taken for an **EOM** aligned exactly with the incoming light polarisation.

This phase would not be very stable, as it is dependant on minute details of the shifting operation. Compared to the phase-stability in the microwave pulse preparation, this is not well controlled and could therefore limit coherence times. To prevent this, the bottom of the traps for $|0\rangle$ and $|1\rangle$ have to always be at the same height. This also can be done by changing the power distribution between the two lattices. A plot (fig. 3.9 on page 61) shows though, that one cannot optimize both for identical trap depths and ground state energy at the same time. As we do later experiments in a spin-echo type experiment, it was decided not to try to cancel the phase evolution but instead minimize excitations. The spin-echo technique then removes most, if not all, of the phase picked up due to the unequal trap energies.

From fig. 3.8, the point of minimal lattice depths during the shifting can be determined. Then the **EOM** is rotated to different settings and the minimal trap frequency is measured (see fig. 3.10 on page 61). Note that in the experiment, the $\lambda/2$-plate (d) in fig. 3.3 on page 52 is turned, not the
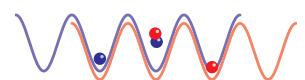
EOM itself. This causes a factor of two in the angles (i.e. an EOM-angle of 7.6° means the $\lambda/2$-plate was rotated by 3.8°. This measured angle of 7.6° for balanced trap frequencies agrees well with the calculation shown in fig. 3.9 on the next page.

3.3.2. Adiabaticity

To detect if the shifting process creates excitations into higher trap states, the population of the different trap levels needs to be measured. For that, the individual trap levels are mapped onto different Brillouin zones at the beginning of the Time-of-Flight (TOF). In short, a more adiabatic switch off of the lattice causes different Bloch states with quasi-momentum q to be mapped onto different free particle momenta (see fig. 2.11 on page 32). The ramp-down process needs to be fast compared to the tunnelling time, to prevent the simple deloading of the lattice into a single Bose-Einstein-Condensate (BEC). The chosen ramp-down time for these experiments is 500 μs. In the TOF images, the excited atoms lie outside of the first Brillouin zone and a simple atom-counting yields the excitation probability. This can then be compared to the ab initio calculation from appendix A.2.

The experiment starts with a Mott-Insulator. The trapping frequency of the shifting x-lattice is set to $\omega_x = 2\pi \times 45$ kHz. Depending on the investigated atomic state, a microwave π-pulse brings all atoms from state $|0\rangle$ to state $|1\rangle$. The control voltage of the EOM is then linearly increased in a time τ until the atomic state has been moved one lattice site further (by a distance of $\lambda/4$). There is no interaction between neighbouring atoms, as they have not been delocalised in the process. Either all atoms move $\lambda/4$ to the left (no π-pulse) or all move to the right (with π-pulse). After that, the lattice is adiabatically switched off and an image is taken after 14 ms TOF. The relative number of excited atoms is measured versus τ.

In fig. 3.11 on page 62 the excitation probability for both states is plotted together with sample absorption images, for some of the data points. The dashed lines in the images correspond to the border of the first Brillouin zone. Te shift to the nearest neighbour can be done in <10 μs, limited by the bandwidth of the EOM high voltage amplifier. For fast shifts of up to 25 μs, the system is excited quite strongly. Both atomic states behave nearly identically for different shift speeds. For shift times of 40 μs or more the excitation becomes minimal. Following experiments are therefore done with shift speeds of 50 μs and the technical limitation is not relevant.
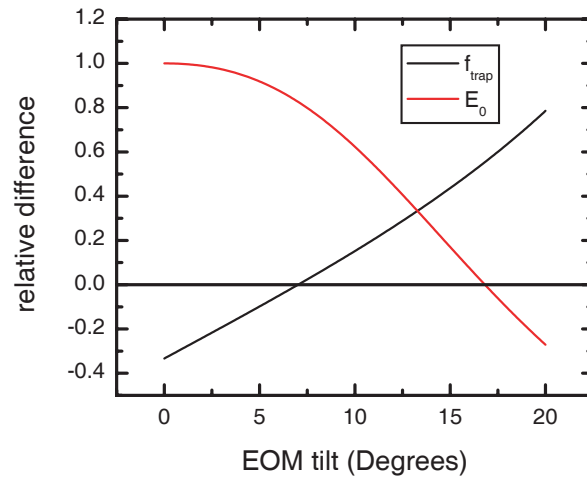
Figure 3.9.: Comparison of trap depth and ground state for a titled EOM. The graph shows the relative difference $(f(|0\rangle) - f(|1\rangle))/(f(|0\rangle) + f(|1\rangle))$ for f = "trap depth" (black) and f = "bottom of the trap" (red) versus the tilting angle of the EOM.
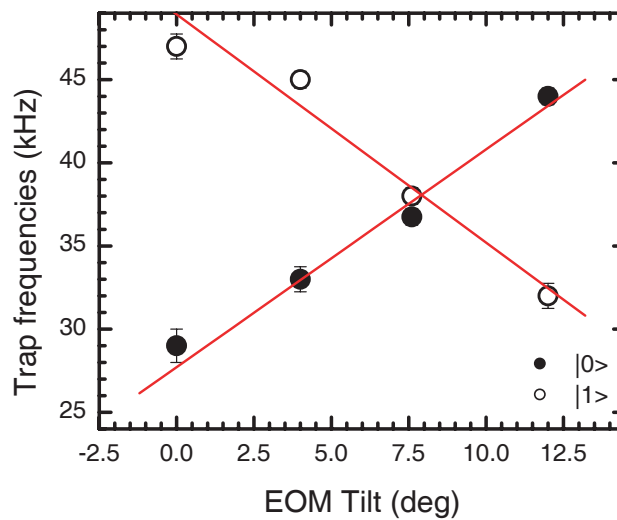
Figure 3.10.: Optimization of the EOM angle. Shown is the measured trap frequency as a function of the EOM rotation for $|F = 0\rangle$ (filled) and for $|F = 1\rangle$ (hollow circles). The graph shows the (virtual) angle of the EOM, not the angle of the $\lambda/2$-plate that was really used to turn the polarisation.
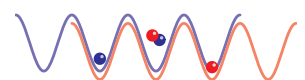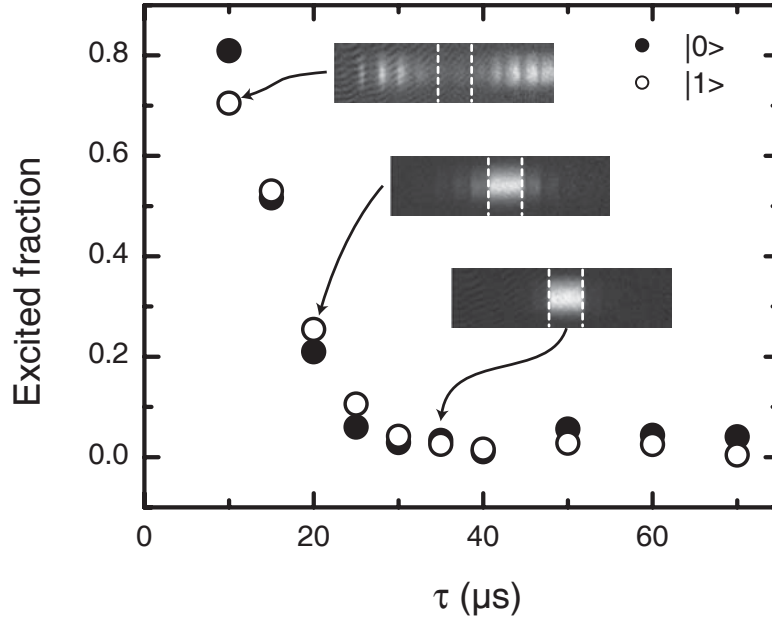
Figure 3.11.: Relative atom number excited from the ground state
after a shift of $\lambda/4$ in a time τ. The hollow (filled) circles rep-
resent atoms in state $|0\rangle$ ($|1\rangle$). The images shown correspond
to the indicated $|1\rangle$ data points.

3.3.3. Controlling the Phase-Shift

During the delocalisation process, each atomic state can pick up a kinetic
phase. In order to do useful experiments on the system, the acquired
phase has to be constant for all atoms independent of their position in
the trap and it has to be constant for different realizations of the same
experiment.

   In order to test this, an atom interferometer is used (see 3.12 on the fac-
ing page). The system is prepared in a MI state with one atom per lattice
site in state $|0\rangle$. Then a $\frac{\pi}{2}$-pulse brings each atom into a superposition of
$|0\rangle$ and $|1\rangle$. The lattice is shifted then, delocalising each atom over two
lattice sites. A second $\frac{\pi}{2}$-pulse puts each of the delocalised parts of an
atom into a superposition of $|0\rangle$ and $|1\rangle$, this way erasing the informa-
tion stored in the state of the atom if it is in the left or right lattice site.
After that the lattice is switched off and the atom is allowed to expand.
As in a double slit interference experiment, the expansion from two sep-
arate coherent sources creates an interference pattern. The difference to

Youngs experiment is that here a matter wave of one atom interferes with itself. The interference pattern formed in free flight is finally imaged onto a Charge Coupled Device (CCD) camera.

This type of interferometer in principle produces the same information as a trapped atom interferometer, the effects of TOF time and microwave-phase α can be found in appendix A.3. A phase is fitted to the interference fringe and the stability of this phase is observed over multiple runs of the experiment. Also, the question is examined, how well the interference phase can be controlled by tuning the interferometer.

The data taken by the imaging, relative atom number and interference fringe, is always the average over all atoms in the cloud. But the interference itself is a single particle interference. So if a well modulated interfer-
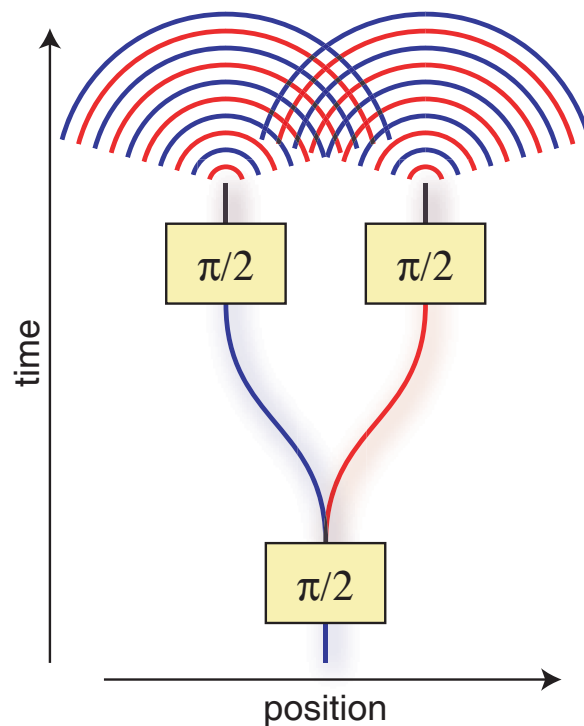
Figure 3.12.: "Double-slit" free flight atom interferometer. The atom is brought into a superposition state, delocalised and then the which-way-information is erased. After switching off the trapping potential, the the wave function of the atom expands and creates an interference pattern in free flight.
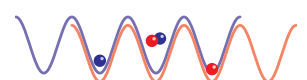
ence fringe is visible, this means that the single particle phase shifts dur-
ing the interferometer sequence were identical. Or expressed differently,
the shifting in the interferometer-sequence does not destroy the coherence
of a composite state.

Figure 3.13 shows a few example interference fringes in the insets. The
fitted phase ϕ is plotted vs. the $\pi/2$-pulse phase α. The expected linear
dependence $\phi(\alpha)$ is well fulfilled. This means that not only is the phase
between different realizations constant, this constant phase can also be
compensated by applying the last microwave pulse with a selected phase.
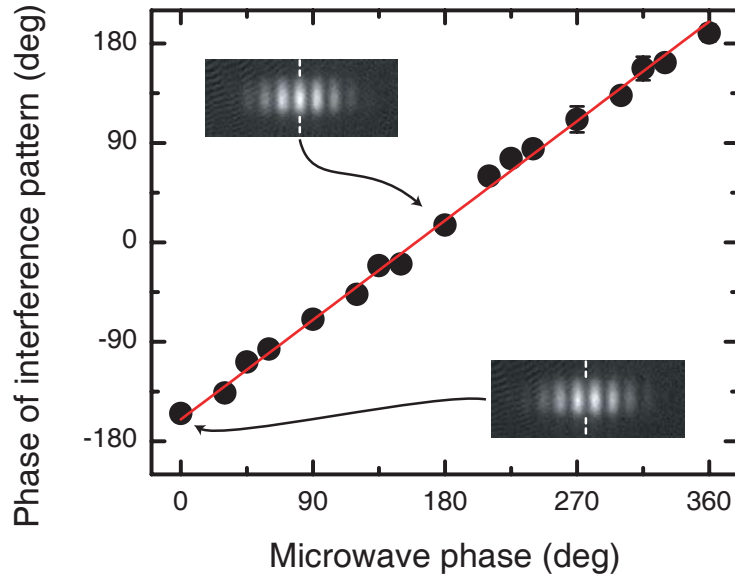
Figure 3.13.: Stability and controllability of the double slit inter-
ference pattern. The phase α of the last microwave-pulse of a
free-flight interferometer is varied and the pattern for state $|1\rangle$
is observed (see insets). To these a phase is fitted and plotted
in the graph.

3.3.4. Delocalisation over Large Distances

Delocalising over nearest neighbours means rotating the lattice polarisa-
tion α by $180\,°$. Delocalising further could be done by simply increasing
the rotation angle. But that is limited by the maximum control voltage
that can be applied to the EOM. Instead, another technique is used here:

consider the spin-echo technique introduced in section 3.2.3. After delocalising over a distance of one lattice site, a π-pulse is used to exchange the states $|0\rangle \leftrightarrow |1\rangle$. For example, a $|1\rangle$ state moves to the right in the first shift operation and is changed into a $|0\rangle$ state by the π-pulse (phases neglected here). Then the EOM control voltage is ramped back to the initial value, but the changed states mean that the atom is delocalised further instead of brought together. Another π-pulse may then again exchange the states and the delocalisation process may continue. In this step-wise delocalisation, each stroke only moves each of the wave functions by $\lambda/4 = 1/2$ site spacing. Figure 3.14 on the following page shows an example for a delocalisation over three lattice sites.

During the π-pulse, the wave functions of different atoms share a common lattice site. The combined state of the atoms could therefore pick up a collisional phase which is the central part of the gate-sequence shown in section 3.4.4. Here that would be undesired, as we want to demonstrate large delocalisations, not quantum gates (in this section). To suppress collisions, the lattice along the third axis (perpendicular to the imaging plane), is partially reduced after creating the Mott Insulator. This reduces the density inside a lattice site and thus the collision rate.

Figure 3.15 on page 67 contains state selective images taken after a free flight interference sequence (see section 3.3.3). All images show the typical double slit interference pattern with the stripes getting denser for larger delocalisation of the individual atoms. The quality of the double slit interference signal f is measured as the visibility

$$\text{visibility}(f) = \frac{\max(f) - \min(f)}{\max(f) + \min(f)}. \tag{3.9}$$

In this experiment, the visibility is up to 60 % for a delocalisation over adjacent lattice sites, and decreases for larger separations. Possible reasons for this decrease include a slight tilt of the pancake-shaped 3D interference structure relative to the imaging axis and a finite camera resolution: one pixel corresponds to $\approx 4.5\,\mu$m and the expected fringe spacing (see appendix A.3) for the last image of fig. 3.15 is already 27 μm.

3.4. Phase-Gate Experiments

In the previous sections, operations on stored atoms with microwave-pulses and the shifting technique for atoms stored in a lattice were shown. Delocalisation and atom interferometers were introduced, but always the
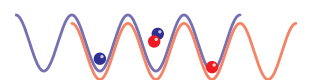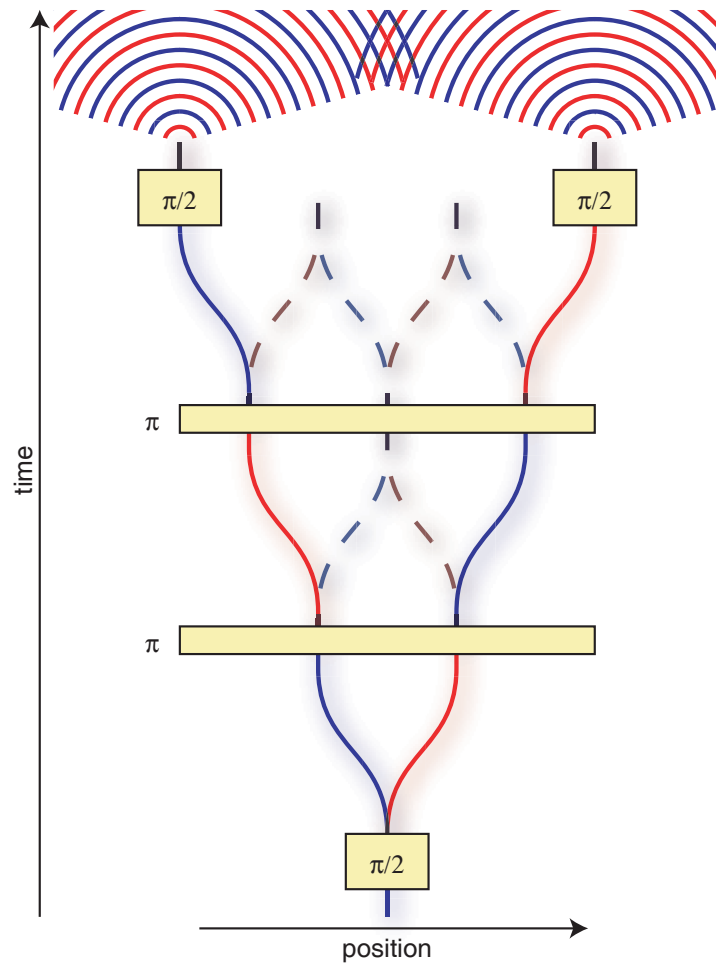
Figure 3.14.: Experimental sequence for delocalising an atom over a distance of three lattice sites. The different colours represent the different states of the atom, the boxes represent microwave pulses for manipulating the atom states.
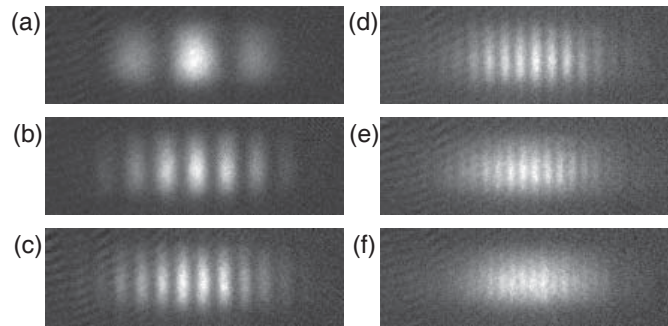
Figure 3.15.: Double slit interference for different delocalisations. The sample was separated over a distance of 1-6 lattice sites (images **(a)-(f)**) in a time of 50 μs. The images are taken of the $|1\rangle$ state after a TOF of 14 ms.

atom-atom interaction was removed from the experiment by reducing the density in the lattice sites. This section now focuses on the effect of atom-atom interaction in the interferometer-sequences. There are two different types of atom interferometers that were already discussed in this chapter: the Ramsey-type atom-interferometer and the Free-flight atom-interferometer. Results from both are shown here.

3.4.1. A Phase-Gate in the Spin-Dependant Lattice

The operation of a phase-gate in the described spin-dependent lattice is straight-forward considering the elementary actions possible. In the following, an example system of two atoms is subjected to the gate operation. The state of the system *after* each step is given. See also fig. 3.16 on page 69 for a graphical representation, with the following steps marked in the graph.

1. Start from a system with one atom stored in each lattice site.

$$|0\rangle_j |0\rangle_{j+1}$$

2. Create a superposition of $|0\rangle$ and $|1\rangle$ using a $\pi/2$ microwave pulse.

$$\frac{1}{2}(|0\rangle_j |0\rangle_{j+1} + i|0\rangle_j |1\rangle_{j+1} + i|1\rangle_j |0\rangle_{j+1} - |1\rangle_j |1\rangle_{j+1})$$
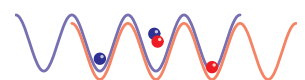
3. Shift the two lattices for $|0\rangle$ and $|1\rangle$ in opposite directions by half a lattice spacing. The atom is delocalised between two neighbouring sites in the process.

$$\frac{1}{2}\left(|0\rangle_j|0\rangle_{j+1} + i|0\rangle_j|1\rangle_{j+2} + i|1\rangle_{j+1}|0\rangle_{j+1} - |1\rangle_{j+1}|1\rangle_{j+2}\right)$$

4. Wait for the state of two atoms in one combined trap to accumulate the desired collisional phase shift φ.

$$\frac{1}{2}\left(|0\rangle_j|0\rangle_{j+1} + i|0\rangle_j|1\rangle_{j+2} + ie^{i\varphi}|1\rangle_{j+1}|0\rangle_{j+1} - |1\rangle_{j+1}|1\rangle_{j+2}\right)$$

5. Recombine the two state-dependent traps, that contain each atom. The atoms/qubits are localized to a single trap after that.

$$\frac{1}{2}\left(|0\rangle_j|0\rangle_{j+1} + i|0\rangle_j|1\rangle_{j+1} + ie^{i\varphi}|1\rangle_j|0\rangle_{j+1} - |1\rangle_j|1\rangle_{j+1}\right)$$

6. Erase the 'Which-Way information' with a second $\pi/2$-pulse. Without that, the information 'went left' or 'went right' during the shifting could be read from the state of an atom. For doing a Ramsey-experiment, the phase of this pulse can be shifted by an arbitrary phase α.

$$\begin{aligned}\frac{1}{4}\Big\{ &\left(1 - e^{i\alpha} + e^{2i\alpha} - e^{-i(\varphi-\alpha)}\right)|0\rangle_j|0\rangle_{j+1} \\ &+ i\left(e^{-i\alpha} - e^{i\alpha} - e^{-i\varphi} + 1\right)|0\rangle_j|1\rangle_{j+1} \\ &+ i\left(e^{-i\alpha} - e^{i\alpha} + e^{-i\varphi} - 1\right)|1\rangle_j|0\rangle_{j+1} \\ &- \left(1 + e^{-i\alpha} + e^{-2i\alpha} + e^{-i(\varphi+\alpha)}\right)|1\rangle_j|1\rangle_{j+1}\Big\}\end{aligned} \qquad (3.10)$$

After that, measure the result of the gate sequence in a TOF imaging. The gate-sequence is that of a Ramsey-experiment. The distinguishing point that makes this a quantum gate, is that the phase picked up between the $\pi/2$-pulses is a function of more than one atom. The Ramsey-interferometer is a trapped-atom interferometer, where each of the atoms is split into two paths, spatially separated for a certain time and recombined later. The $\pi/2$-pulses act as beam-splitters and the shiftable lattice keeps the atoms trapped at all times.
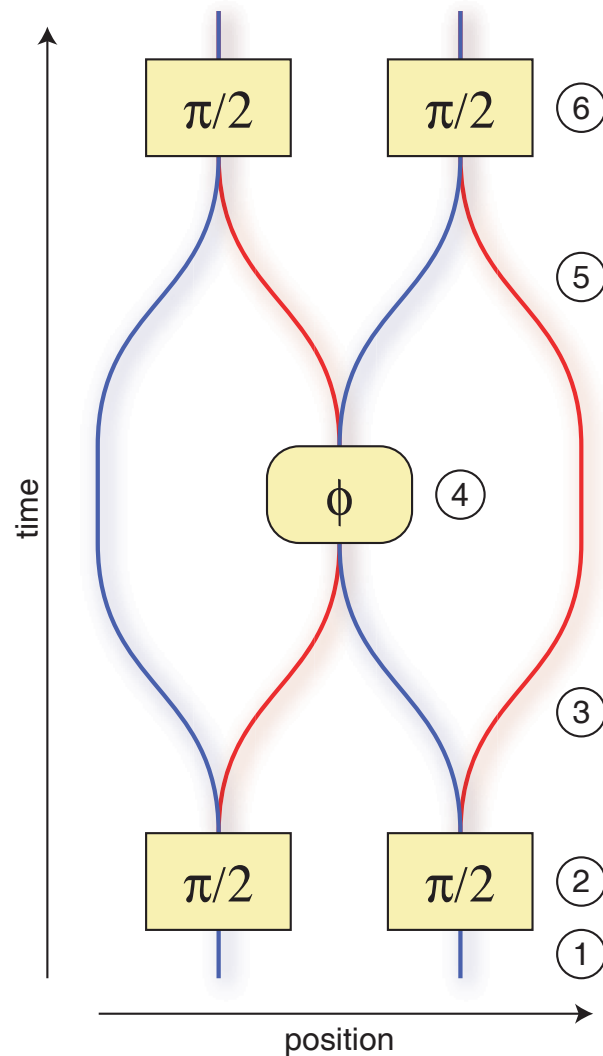
Figure 3.16.: A general gate operation between two neighbour-
ing atoms. The position of the atomic states in the lattice is
shown horizontally, while the time extends from the bottom
to the top of the illustration. The states $|0\rangle$ ($|1\rangle$) are encoded in
the colours blue (red). Rectangular boxes mark a microwave
$\pi/2$ pulse and the oval box marks the collision that picks up
a collisional phase ϕ. The circled numbers correspond to the
text on page 67
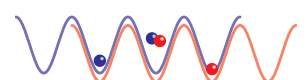
To illustrate the entanglement in (3.10), we consider the special case $\alpha = 0$. Then (3.10) can be rewritten as

$$\frac{1 + e^{-i\varphi}}{2} \overbrace{i^2 |1\rangle_j |1\rangle_{j+1}}^{\text{Product state}}$$

$$+ \frac{1 - e^{-i\varphi}}{2} \frac{1}{2} \underbrace{\left\{ \left(|0\rangle_j - i|1\rangle_j \right) |0\rangle_{j+1} + i \left(|0\rangle_j + i|1\rangle_j \right) |1\rangle_{j+1} \right\}}_{\text{Bell state}}, \qquad (3.11)$$

showing an oscillation between a product state and a Bell state. From (3.10) the probability to measure the atoms in state $|1\rangle$ is given by

$$P_{|1\rangle} = \frac{1}{4} \left(\cos(\alpha) \cos(\varphi) + \cos(\alpha) + 2 \right). \qquad (3.12)$$

This shows a sinusoidal modulation of the relative atom number under rotation of α. The amplitude of the interference fringe for this trapped atom interferometer is maximal for the product state and vanishes for the entangled state. It can be shown that this is still true for more than two neighbouring atoms. While a direct measurement of entanglement between individual qubits is not realized in our experiment, an indirect measurement can be done: if the reduction in contrast of the trapped atom interferometer is observed, then the only conceivable explanation is the creation of entanglement in the system.

3.4.2. Cluster states

In the previous section, the case of two interacting neighbours was discussed. But one of the advantages of this system of quantum gates in an optical lattice is its inherent parallelism: the operation is applied to all neighbouring atoms, not only to pairs [9, 11].

Repeating the steps described above for three atoms and concentrating only on the entangled state ($\varphi = \pi, \alpha = 0$), the above gate sequence produces the state

$$|0\rangle_j |0\rangle_{j+1} |0\rangle_{j+2} \xrightarrow[\text{sequence}]{\text{gate}} \frac{1}{2\sqrt{2}} \Big\{ \left(|0\rangle_j - i|1\rangle_j \right) |0\rangle_{j+1} \left(|0\rangle_{j+2} + i|1\rangle_{j+2} \right)$$

$$- i \left(|0\rangle_j + i|1\rangle_j \right) |1\rangle_{j+1} \left(|0\rangle_{j+2} - i|1\rangle_{j+2} \right) \Big\}, \quad (3.13)$$

which is a Greenberger-Horne-Zeilinger (GHZ) state [10]. We will call the result of applying the gate operation to n neighbouring atoms $|\phi_n\rangle$. The GHZ state in (3.13) can be written more compact by omitting the index for the lattice site and by only only specifying the state up to a local unitary (indicated by the $=_{\text{l.u.}}$ sign) operation:

$$|\phi_3\rangle =_{\text{l.u.}} \frac{1}{\sqrt{2}}(|0\rangle|0\rangle|0\rangle + |1\rangle|1\rangle|1\rangle). \tag{3.14}$$

While $|\phi_2\rangle$ and $|\phi_3\rangle$ are both (generalised) GHZ states, i.e. they can both be written as a superposition of all atoms in state $|0\rangle$ and all atoms in state $|1\rangle$, the result for 4 atoms is not:

$$\begin{aligned}|\phi_4\rangle =_{\text{l.u.}} \frac{1}{2}\big(&|0\rangle|0\rangle|0\rangle|0\rangle + |0\rangle|0\rangle|1\rangle|1\rangle \\ &+ |1\rangle|1\rangle|0\rangle|0\rangle - |1\rangle|1\rangle|1\rangle|1\rangle\big).\end{aligned} \tag{3.15}$$

For all $n > 3$, the $|\phi_n\rangle$, which are called "cluster states" [11], are different from GHZ states. The cluster state for general n can be written as a concatenation of states and the z-spin operator $\hat{\sigma}_z^{(j)}$ for lattice site j:

$$|\phi_n\rangle = \frac{1}{\sqrt{2^n}}\bigotimes_{j=1}^{n}(|0\rangle_j\hat{\sigma}_z^{(j+1)} + |1\rangle_j). \tag{3.16}$$

Here the convention $\hat{\sigma}_z^{(n)} = 1$ is used to not leave an unevaluated operator in the final term. In the evaluation, this would produce

$$\begin{aligned}(|0\rangle_{n-1}\hat{\sigma}_z^{(n)} &+ |1\rangle_{n-1}) \otimes (|0\rangle_n + |1\rangle_n) \\ &= |0\rangle_{n-1}(|0\rangle_n - |1\rangle_n) + |1\rangle_{n-1}(|0\rangle_n + |1\rangle_n).\end{aligned}$$

There has yet to be devised a commonly agreed upon measure for entanglement. It is therefore not straightforward to compare the cluster state to other entangled states, e.g. the generalized GHZ state. Reference [11] proposes two properties of entangled states and uses them to compare cluster states and GHZ states:

Maximum connectedness A n-particle state is maximally connected, if any pair of its constituents can be brought into a pure Bell state by local measurements on the other particles. Both the GHZ state and the cluster state have this property.
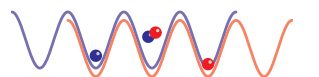
Persistency A measure of how difficult it is to completely disentangle a n-particle state. For the GHZ state a single local measurement projects the whole state into a product state. But it takes at least $\lfloor n/2 \rfloor$ measurements, to completely destroy all entanglement of a cluster state. In that sense, the cluster state is more robust that the GHZ state.

For further applications of cluster states in quantum information processing see chapter 4.

3.4.3. Ramsey-Type Atom-Interferometer

After having discussed the gate-sequence in detail for the case of two atoms and then extending the description to cluster states for larger atom numbers, this section describes the realisation of that gate-sequence in the experiment. The main differences to the description in section 3.4.1 are an additional π-pulse during the collision time and the number of neighbouring atoms that is as high as 60 atoms in a row. The π-pulse is used to increase the coherence time in the system with a spin-echo technique. The experiment is run in a lattice of isolated atoms initialised from a MI state with a diameter of $n \approx 60$ lattice sites. Even if one allows for some vacancies to form after the phase-transition to the MI, and even if the MI-phase with exactly one atom per lattice site does not span the complete 60 lattice sites but there is a sphere of superfluid lattice sites surrounding it: there are more than a few neighbouring lattice sites containing one atom each.

The experiment is illustrated in fig. 3.17 on the next page, with the next lattice sites to the left and to the right not occupied by an atom. The additional π-pulse changes the local states, essentially flipping $|0\rangle$ and $|1\rangle$. This does not affect the entanglement of a state and in the measurements below, this is only visible as a phase-shift in α. Without the π-pulse though, coherence would have been lost before the end of the first entanglement oscillation.

The creation of entanglement is measured as the reduction of the interference fringe of the Ramsey-interferometer. The effect is easily illustrated for two neighbouring atoms, where (3.12) directly shows the vanishing of the interference fringe. Another explanation for two atoms is to rewrite (3.10) for $\varphi = \pi$:
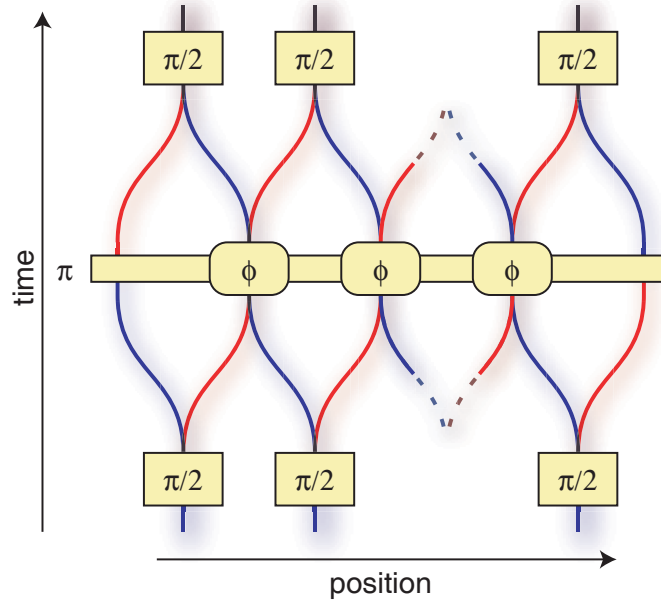
Figure 3.17.: The experimental sequence for the trapped atom interferometer. An additional π-pulse during the interaction time cancels the unwanted effects of non-homogeneous or fluctuating magnetic fields.

$$\frac{1}{2}\Big(\underbrace{(e^{i\alpha}\cos(\alpha)|0\rangle_j + (\sin(\alpha)-i)|1\rangle_i)|0\rangle_{j+1}}_{A}$$

$$+\underbrace{(\sin(\alpha)+i)|0\rangle_j - (e^{-i\alpha}\cos(\alpha)|1\rangle_i)|1\rangle_{j+1}}_{B}\Big) \quad (3.17)$$

and then to consider the measurement results for the terms A and B separately (as we want to have the probability to have an atom in state $|1\rangle$ and not the number of atoms in state $|1\rangle$, there is an additional term $\frac{1}{2}$):

$$P_{|1\rangle} = \frac{1}{2}\frac{1}{4}\Big(\overbrace{1+\sin^2(\alpha)}^{A} + \overbrace{1+\sin^2(\alpha)+2\cos^2(\alpha)}^{B}\Big) = \frac{1}{2} \quad (3.18)$$

The interference phase for one atom depends on the state of the other. The two interference fringes caused by terms A and B are $180°$ out of phase.
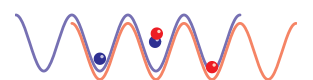
For $n > 2$ the interference visibility also goes down (see ref. [93]).

In the experiment, the collisional phase φ is proportional to the time t_{Hold} that nearest neighbours are allowed to interact with each other. The result of measuring $P_{|1\rangle}$ for different phases α gives an interference fringe that can be fitted to a sine. The visibility as defined in (3.9) for different t_{Hold} is shown in fig. 3.18 on the facing page.

The visibility of the interference itself follows a sinusoidal shape, the minimum at t_{Hold}=210 μs is the point of maximum entanglement. The initial visibility of the sample is 51 %, which drops to 8 % for the entangled system. After a complete cycle of entangling and disentangling, the visibility is a bit higher at 57 %. Also, the complete cycle is slightly out of phase for a cosine: the first maximum (at 480 μs) is not at double the position of the minimum (at 210 μs). The explanation for both effects is that the system is already slightly entangled for t_{Hold}=0 μs. This can happen during the shifting, shortly before the different lattice potentials completely overlap and during the first few moments when they separate afterwards. The overlap between the different atomic wave functions does not vanish immediately but grows weak slowly with increasing lattice site separation. Thus some interaction happens outside of what is called here the hold time t_{Hold}.

One possible reason for the visibility to be not near 100 % is that the EOM had to first shift from the starting configuration to the interaction position where the π-pulse swaps the states. So returning the atom to their starting position means to shift the EOM further to another overlap-configuration instead of back to the start-configuration. Slight asymmetries in the EOM setup mean the two shifts are not completely identical and the spin-echo can not completely cancel any shift-related phases.

Other reasons include:

- finite accuracy in the atom-number measurement

- isolated atoms not taking part in the gate-sequence: the Superfluid (SF) around the MI core [7, 94, 95], atoms with vacancies on both sides.

The second point warrants some explanation: an isolated atom does not undergo a spin-selective phase evolution, hence it will always produce a Ramsey-fringe of maximal visibility. The atom can be isolated, because it is not in the central region of the trap, which is in the MI state, but in an outer region with a SF state. Or the atom is located in the inner part of the trap, but is neighboured by vacancies: Directly after creation,
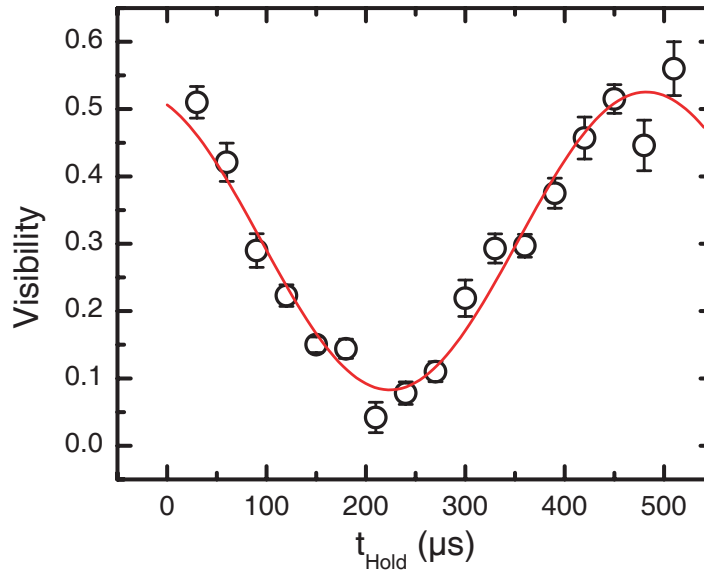
Figure 3.18.: Gate sequence in a Ramsey-interferometer. Shown is the visibility fitted to interference fringes of the Ramsey-interferometer for different interaction times t_{Hold}. The visibility is t_{Hold}=30 µs: 51 %, 210 µs: 8 %, 510 µs: 57 %.

the MI should have next to no vacancies, but during the preparation of the magnetic field to a stable 1 G value the system becomes noticeably deteriorated.

In both the trapped-atom interferometer and in the free-flight interferometer the minimum visibility is $\approx 8\%$. Two effects can cause a finite visibility at these times t_{Hold}:

- isolated atoms as above

- slight errors in the microwave pulse area. Even a 5% fractional error in the $\frac{\pi}{2}$- or π-pulses can lead to a reduced gate fidelity.

The entangling effect spans only connected chains of atoms. One vacancy disrupts this chain and the two parts do not become entangled with each other. If one takes the finite 8% visibility as completely caused by isolated atoms in the MI region of the trap, then the probability P of finding a vacancy in a lattice site is $P^2(1 - P) = 0.08 \Rightarrow P = 0.35$. This is much higher than observed, so the estimate will give too little entanglement. Simulating the chain-length possible even under these conditions
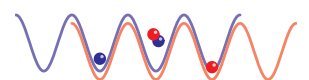
returns as many isolated atoms as occurrences of two neighbouring atoms plus three neighbouring atoms. And there is a high possibility for linger chains of atoms. So even if this measurement does not rigorously prove entanglement of more than pairs of atoms, it is highly indicative of that.

3.4.4. Free-Flight Atom-Interferometer

To observe the evolution of the system under the gate-operation for a longer hold-time, it is more convenient to use a free-flight atom-interfero-meter. Using this interferometer reduces the amount of measurements to take by a factor of 8 (as we took that many different values for α to measure the interference fringe in the previous section).

   The experimental sequence is shown in fig. 3.19. As described in sec-tion 3.3.3, this is analogous to Youngs double-slit interference experiment. An atom is delocalised over two lattice sites and allowed to expand. It in-terferes with itself and this interference pattern is then imaged by a CCD camera. But here neighbouring double-slits are fed with atoms that can
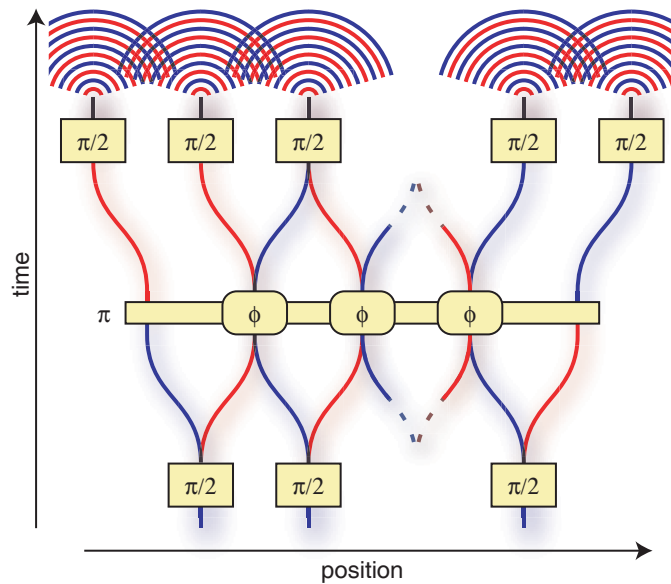
Figure 3.19.: The experimental sequence for the free-flight atom interferometer. After the interaction a further delocalisation step allows to read out the interferometer as the overlap of the double-slit interference patterns of each individual atom.
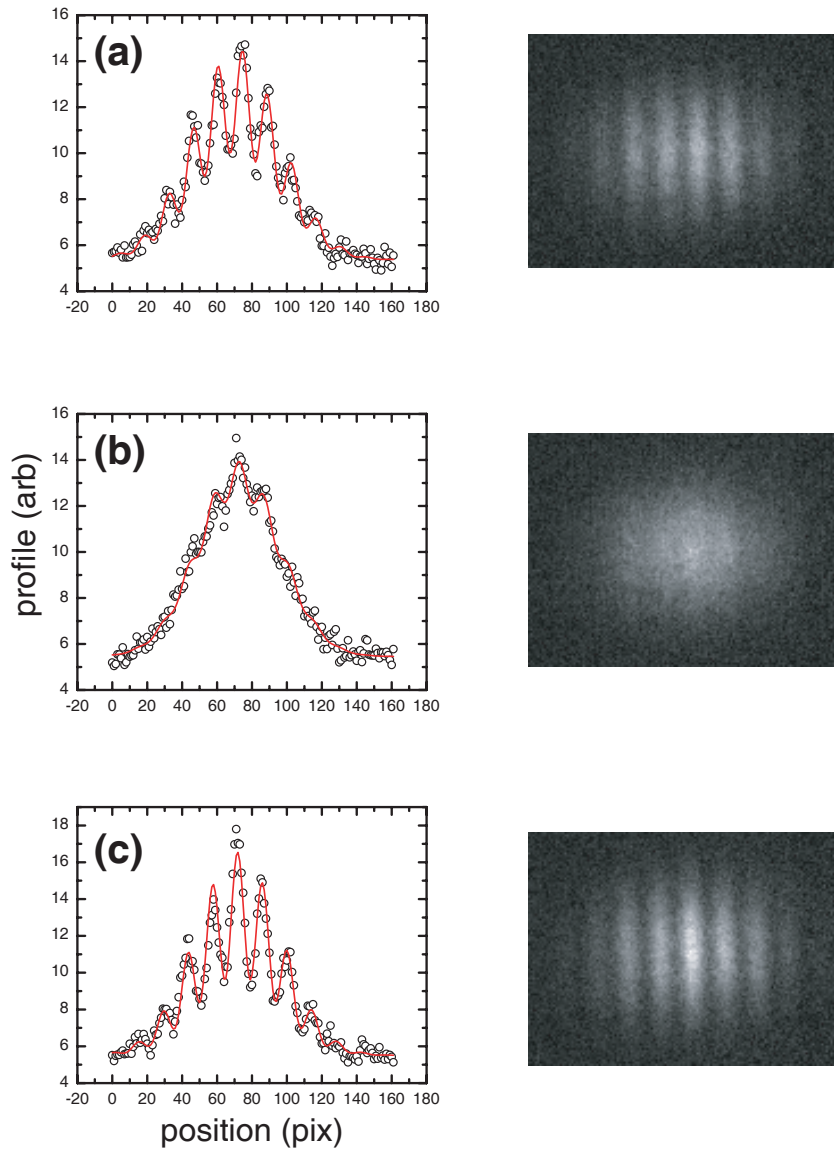
Figure 3.20.: Profiles from a Free-Flight Interferometer. The graphs show the intensity profile from a horizontal cut in the images, integrated over several CCD-rows. The height is in arbitrary units, the position is in pix $\approx 4.5\mu m$. The TOF is 11 ms. The visibility V for the different hold times t_{Hold} is **(a)** $V(30\,\mu s) = 33\%$, **(b)** $V(210\,\mu s) = 9\%$, **(c)** $V(450\,\mu s) = 44\%$.
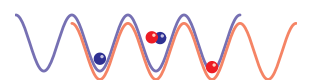
be entangled with each other. Analogous to (3.18), the two atoms will form interference patterns that are 180° out of phase and will thus cancel.

Exemplary interference patterns recorded with the **CCD** camera are shown in fig. 3.20 on the preceding page for different interaction times t_{Hold}. The profiles shown in the graph are fitted to a Gaussian envelope modulated with an interference fringe of visibility V:

$$f(x) = A e^{-\left(\frac{x-x_0}{w}\right)^2} \left(1 + V \sin\left(2\pi\left(\frac{x}{k} + \phi\right)\right)\right) + y_0. \qquad (3.19)$$

Here V, A, x_0, w, k, ϕ and y_0 are fit parameters with V being the visibility. More details about the fringe spacing k can be found in appendix A.3.

Stepping through t_{Hold} and measuring the visibility, the evolution over four complete gate cycles of entangling and disentangling can be measured. Figure 3.21 shows the average of three to four fitted visibilities per point.
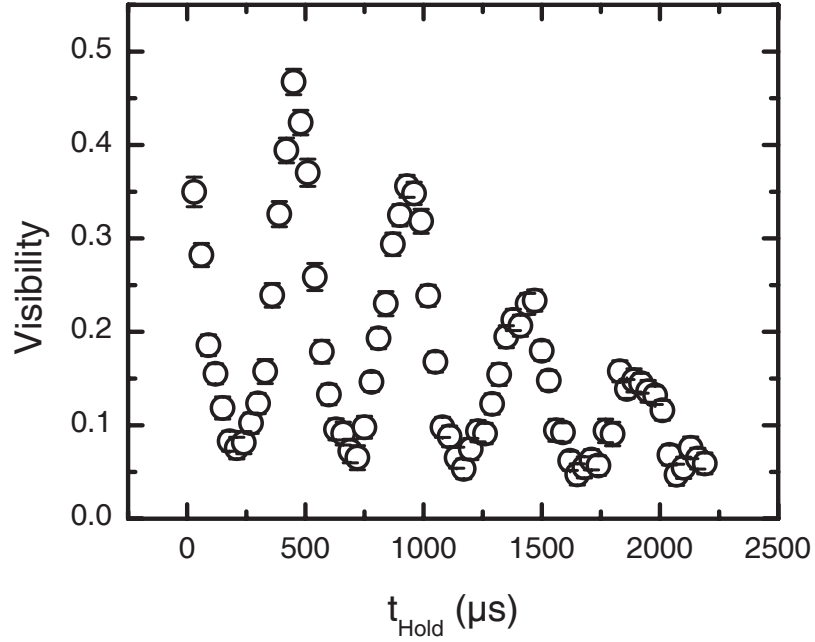
Figure 3.21.: Gate sequence in a free-flight-interferometer. Shown is the visibility fitted to interference images from the free flight interferometer for different interaction times t_{Hold}. The visibility is t_{Hold}=30 μs: 35 %, 210 μs: 8 %, 450 μs: 47 %. A total of 4 cycles of entanglement and disentanglement can be observed.

The visibility is again very low in the first data point, as there is additional collisional phase picked up during the shifting. After that, the visibility of the completely disentangled state is 47 %. This is lower than for the Ramsey-type interferometer, because the interference fringe is detected differently. One would actually expect a *better* visibility, as this interferometer does not suffer the problem of asymmetric EOM ramps described in the previous measurement. Here, the EOM is ramped symmetrically, as the π-pulse swaps the states in the middle of the sequence.
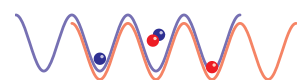
4. Outlook

In this work, an experimental realisation of stored single atoms in an optical lattice to represent qubits has been introduced. A shifting technique allowed for controlled interaction between neighbouring atoms and a new multi-qubit phase-gate has been implemented and used to entangle a large number of qubits in parallel in a single gate-operation.

Quantum random walks

One application of this technique that seems directly feasible is the study of so called quantum random walks [96]. Here a particle in the lattice is distributed over a region of adjacent lattice sites in a random pattern. The process consists of a series of steps, either to the left or to the right. The "decision" on the direction is done by creating a superposition of $|0\rangle$ and $|1\rangle$ and then delocalise this state over the next neighbours (see fig. 4.1 on the following page). Contrary to the classical random walk where the probability to find the atom is highest around the starting position, for the quantum random walk the atom is likely to be found far away from the centre. The experiment would much resemble the one for delocalising an atom over two lattice sites with a larger separation (see section 3.3.4). The difference are the microwave pulses: the (spartially) spin-echo type π-pulses are replaced for this experiment with $\frac{\pi}{2}$-pulses that before each step create a superposition state to be delocalised. The information on the random walk can be extracted from comparison of the interference pattern to theoretical calculations.

Quantum simulation

From here on, it seems but a small step to realizing a quantum simulator along the original ideas of Feynman from 1982 [2]. This device would allow to simulate complex 1D spin-$\frac{1}{2}$ Hamiltonians on a lattice [1]: the long-range potential of the Hamiltonian in question is developed as acting on spins in a distance of multiples of the lattice spacing $\lambda/2$. For any real potential, this development continues to an infinite distance. But for simulating the target Hamiltonian over a short time T within a desired accuracy, the number of development steps n can be chosen to relatively short. The target Hamiltonian is then simulated in a series small time-
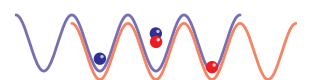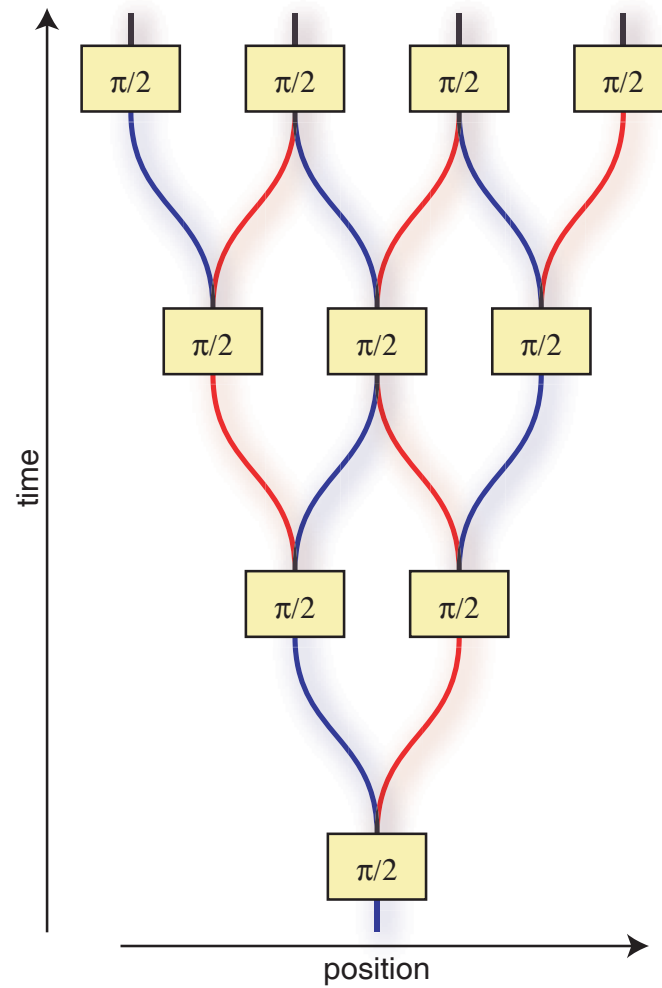
Figure 4.1.: Quantum random walk. A sequence of three steps in the quantum random walk delocalises one atom over a region of four lattice sites.

steps t_{step} (also dependant on the desired accuracy):

1. Start the simulation of the first time-step by creating a superposition with a $\pi/2$ microwave pulse. $t = 0$.

2. Start a new time-step: $i = 0$.

   a) Shift one site apart: $i+ = 1$.

   b) Acquire the collisional phase according to the development of the target-Hamiltonian: wait a time t_i

   c) If $i < n$, return to step 2a.

3. Return the system to initial setup: Shift i sites in the opposite direction. Finish the time-step: $t+ = t_{step}$.

4. If $t < T$, return to step 2.

5. Finish the simulation with a final $\pi/2$ microwave pulse.

With the algorithm sketched above, Hamiltonians such as the 1D Ising or the isotropic and anisotropic Heisenberg Hamiltonian could be simulated. The ratio of coherence-time to gate-duration is important here: at the moment, a few complete cycles of entanglement and disentanglement could be observed. This value is limited by magnetic field fluctuations, the speed of the collisional phase evolution and the shifting time. While the magnetic field fluctuations are somewhat difficult to tackle technically, a better active field stabilisation together with passive shielding should improve the stability immensely. The collision rate can be increased by using stronger lasers for the lattice. It might be needed to switch to blue-detuned lattices, though, to keep the spontaneous photon scattering events to an acceptable level. And there are at the moment calculations under way to optimize the shifting ramp for faster gate operation.

2D and 3D cluster states

At the moment, the cluster state created during the example gate operation is 1D. There are many redundant copies of each cluster state, but they are not connected. So a single vacancy in a string of lattice sites during the state creation would separate the two parts of the string and the cluster state could not spread across the vacancy. This issue was handled in the last part of section 3.4. If the cluster state was created in 2D, though, there suddenly is a finite percolation threshold [97]. As long as two qubits are
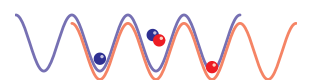
connected by a line of direct neighbours, they are part of the same cluster state after a 2D entanglement sequence. This would further reduce the requirements on the probability of having a vacancies.

The extension of the current setup to two or even three dimensions is straight-forward: obtain another Electro-Optical Modulator (EOM) and copy the shifting lattice setup (see fig. 3.3 on page 52). Apart from any technical details there are only two points to observe:

- The qubit states $|0\rangle$ and $|1\rangle$ are states of the hyperfine split ground states. They are only distinguished in a non-zero magnetic field. For the shifting setup, this magnetic field has to point in the direction of the shifting axis. So in a 2D or even 3D shifting lattice setup, the magnetic field has to be rotated before every shift operation to point along the desired shifting direction.

- The shifting lattice is comparatively near resonant to the ^{87}Rb D_1 and D_2 atomic lines. This could limit the life-time if many lattice axes are run at 785 nm. The laser should have a very clean mode with very little background near the ^{87}Rb-resonances.

One-way quantum computation

Also, the created cluster state might prove essential for later realisations of a quantum computer. In a 2D cluster state with individual qubit-addressing, the circuitry for a quantum computer can be created on-the-fly by spin-selective measurements: analogous to the process of etching a printed circuit board, the circuit is "etched" out of a 2D cluster state by measuring all unneeded qubits in the z-basis. Afterwards, the calculation is propagated through the remaining circuits by measurements in the xy plane. A detailed discussion of this approach can be found in ref. [85]. Figure 4.2 on the facing page shows the basic concept for the example of two CNOT-gates.

The circuit, that is the basis for the quantum computation, is not fixed from the beginning, as the net of a modern Central Processing Unit (CPU) is. In a modern computer, the circuitry is fixed from production on, and the program run on the CPU defines what calculation gets executed. In the cluster state quantum computer, the circuitry is not fixed, but rewritten before every calculation. This is loosely comparable to a Field Programmable Gate Array (FPGA), which is also a stack of gates that can be freely interconnected during initialization of the chip. The cluster state is even more flexible, as it does not define a list of gates and has
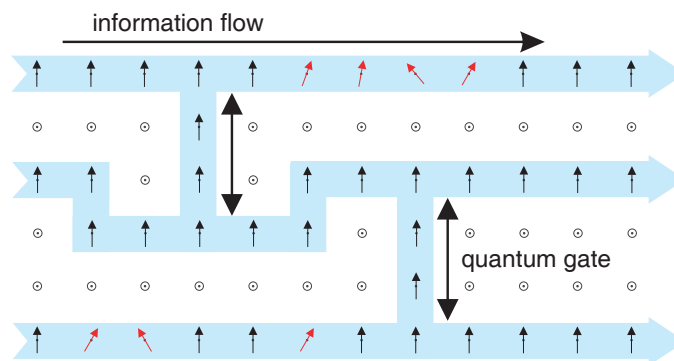
Figure 4.2.: Quantum computation in a 2D cluster state. In the 2D cluster state, measurements in the z-basis (shown in white) cut out the circuitry for the calculation (shaded). The information propagates along with the ongoing measurements in the x basis (vertical arrows). Single qubit operations are possible by measuring in the xy-plane (tilted arrows) and connecting two "wires" creates a quantum gate. (With kind permission from R. Raussendorf *et al.* [85])

no fixed number of interconnects. Programmable logic allows the use of strongly optimized nets of (quantum) gates, that have no overhead for programmability, as today's CPUs need. This would simplify the introduction of the first quantum computers, while gate count and coherence time is limited. Programmable quantum computers analogous to today's computers could be realized in a second step.

Another advantage of the freely programmable layout becomes apparent, when there are defects in the lattice of stored qubits (a vacancy or a region with a different groundstate energy): assuming the possibility to detect these defects non-destructively before the initialisation of the cluster state, it is possible to reroute the circuitry for the calculation. That would allow a cluster state quantum computer even in cases where the defects in the lattice of qubits is not negligible.
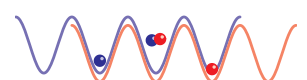
A. Calculations

A.1. Model of the EOM-controlled shifting lattice

In chapter 3.3, a simple model of the spin-dependent optical lattice controlled by an Electro-Optical Modulator (EOM) is introduced. The phase-difference between the ordinary and extraordinary light-axis is explained to change the phase between the two standing $\sigma^{\pm}$-waves and nothing else.

This is certainly not true, if the EOM is not aligned perfectly with the optical axis and with the incident linear polarisation. In this chapter, the case of a rotated EOM is considered, but the EOM is still aligned with the optical axis (no pitch, no yaw).

A.1.1. Definitions

The light beam is described by a complex scalar, where real and imaginary part represent the horizontal and vertical polarized components of the field amplitude. One such beam has the general form:

$$Ae^{i(\pm(\pm kx+\phi_0+B))} \tag{A.1}$$

where k is the wave-vector of the light. The first $\pm$ specifies the rotation sense of the light (σ^+ or σ^-) and the second $\pm$ specifies the direction of light propagation. The always constant time-dependent oscillation of the field is contained in the ϕ_0. A (B) stand for the amplitude (relative phase) of the beam.

With these definitions, the base-vectors for circular and linear polarisa-

tion become:
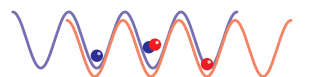
$$|+\rangle = \frac{1}{\sqrt{2}} e^{i(kx+\phi_0)} \tag{A.2a}$$

$$|-\rangle = \frac{1}{\sqrt{2}} e^{-i(kx+\phi_0)} \tag{A.2b}$$

$$|h\rangle = \frac{1}{\sqrt{2}} (|+\rangle + |-\rangle) \tag{A.2c}$$

$$|v\rangle = \frac{1}{\sqrt{2}} (|+\rangle - |-\rangle) \tag{A.2d}$$

The scalar product in this vector-space is

$$\langle a|b\rangle = \frac{1}{\pi} \int_0^{2\pi} a^* b \, d\phi_0. \tag{A.3}$$

With this definition, the integration goes over one complete cycle of the oscillation (as if $\phi_0 \rightarrow \omega t + \phi_0$).

A mirror acting on a beam $|b\rangle$ is then modelled as:

$$m(|b\rangle) = |b(\phi_0 \rightarrow -\phi_0)\rangle. \tag{A.4}$$

A wave plate of r retardance under an angle of α acting on a beam $|b\rangle$ is expressed as:

$$wp_{r,\alpha}(|b\rangle) = e^{i\alpha} \left\{ \mathrm{Re}[e^{-i\alpha}|b(x)\rangle] + i\, \mathrm{Im} \left[e^{-i\alpha} \left| b\left(x + \frac{2\pi r}{k} \right) \right\rangle \right] \right\} \tag{A.5}$$

A.1.2. Standing wave

With these building blocks, the standing wave at the position of the Bose-Einstein-Condensate (BEC) can be constructed. For this, the optical setup depicted in fig. 3.3 on page 52 is used as a model, where elements unnecessary for controlling the polarisation are removed:

$$|sw_\alpha(U)\rangle = |h\rangle + wp_{1/4,0}(wp_{U,\alpha}(m(|h\rangle))). \tag{A.6}$$

The composition of the lattice in terms of σ^+ and σ^- light can be given by projection on the two base-vectors for circular light:

$$\langle +|sw_\alpha(U)\rangle = 1 + \frac{1}{2}\{\cos(2kx) + \cos(2(\pi U + kx))$$
$$+ \sin(\pi U)\left[\sin(\pi U)\sin(4\alpha)\right.$$
$$\left. +2\sin(\pi U + 2kx)(\sin(2\alpha) + \cos(2\alpha))\right]\} \qquad \text{(A.7a)}$$

$$\langle -|sw_\alpha(U)\rangle = \frac{1}{2}\{1 + e^{-2ikx}[\cos(\alpha)(\cos(\alpha) - \sin(\alpha))$$
$$+ e^{-2i\pi U}\sin(\alpha)(\cos(\alpha) + \sin(\alpha))]\}$$
$$\times \{1 + e^{+2ikx}[\cos(\alpha)(\cos(\alpha) - \sin(\alpha))$$
$$+ e^{+2i\pi U}\sin(\alpha)(\cos(\alpha) + \sin(\alpha))]\} \qquad \text{(A.7b)}$$

A.2. Excitations during shifting

When a trapped atom is shifted with the state selective potentials, this must not cause excitations to higher trap states. In section 3.3.2 the excitation probability is measured, yielding a minimum shift time of $\tau \approx 40\,\mu$s. Here, we want to determine the theoretically expected shape of the excitation curve of fig. 3.11 on page 62 following ref. [98].

We assume a single harmonic oscillator in a constant potential. The eigenenergies E_n and the eigenfunctions $|\phi_n\rangle$ of the 1D time-independent Schrödinger equation are:

$$E_n = \hbar\omega\left(n + \frac{1}{2}\right) \qquad \text{(A.8)}$$

$$|\phi_n(x)\rangle = \left(\frac{\beta^2}{\pi}\right)^{\frac{1}{4}}\frac{1}{\sqrt{2^n n!}}e^{-\frac{1}{2}\beta^2 x^2}H_n(\beta x) \qquad \text{(A.9)}$$

Here $n \in \mathbb{N}$, ω is the trap-frequency, $\beta = \sqrt{\frac{m\omega}{\hbar}} = a_0^{-1}$ is the inverse of the harmonic oscillator length a_0, m is the atomic mass and H_n is the nth Hermite polynomial.

We now add a time-dependence by requiring that the trap follows the path $s(t)$ with $s(0) = 0$ and $s(\tau) = 1$:

$$|\phi_n(x,t)\rangle = |\tilde{\phi}_n(x,s(t))\rangle = |\phi_n(x \pm \tfrac{\lambda}{4}s)\rangle. \qquad \text{(A.10)}$$
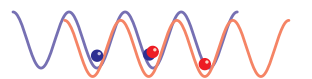
Here the $\pm$ depends on the shifting direction. We will see later, that the final result is independent of the sign. The shifting distance is $\lambda/4$, so for two states shifted in opposite directions, the total distance is $\lambda/2$. The base-states $|\phi_n(x,t)\rangle$ are solutions of the time-independent Schrödinger equation, the time-evolution due to their eigenenergies are missing still. They are added in the next step, that describes a general atomic state $|\psi(x,t)\rangle$ as the linear superposition of base-states

$$|\psi(x,t)\rangle = \sum_k c_k(t) e^{-i\int_0^t \frac{E_k(t')}{\hbar} dt'} |\phi_k(x,t)\rangle. \tag{A.11}$$

This function is now inserted into the time-dependent Schrödinger equation

$$\hat{H}|\psi(x,t)\rangle = i\hbar \frac{\partial}{\partial t}|\psi(x,t)\rangle \tag{A.12}$$

$$\sum_k c_k(t) e^{-i\int_0^t \frac{E_k(t')}{\hbar} dt'} \underbrace{\hat{H}|\phi_k(x,t)\rangle}_{E_k|\phi_k(x,t)\rangle}$$

$$= i\hbar \sum_k \frac{\partial}{\partial t}\left(c_k(t) e^{-i\int_0^t \frac{E_k(t')}{\hbar} dt'} |\phi_k(x,t)\rangle \right) \tag{A.13}$$

The the value on the left hand side results from the time-independent Schrödinger equation. Taking the derivative yields a term that cancels with the left side of the equation:

$$\sum_k \left(\frac{\partial}{\partial t} c_k(t) \right) e^{-i\int_0^t \frac{E_k(t')}{\hbar} dt'} |\phi_k(x,t)\rangle$$

$$= -\sum_k c_k(t) e^{-i\int_0^t \frac{E_k(t')}{\hbar} dt'} \left(\frac{\partial}{\partial t} |\phi_k(x,t)\rangle \right). \tag{A.14}$$

Renaming one of the two summation variables to n and selecting an entry from the second sum yields:

$$\frac{\partial}{\partial t} c_k(t) = -\sum_n c_k(t) e^{i\int_0^t \frac{E_k(t')-E_k(t')}{\hbar} dt'} \langle \phi_k(n,t)| \frac{\partial}{\partial t} |\phi_n(x,t)\rangle. \tag{A.15}$$

Now we consider the special case of only a single eigenstate $|\phi_0(x, t = 0)$ being initially populated, and that the transition probability via other states is small. Then in first-order perturbation theory

$$c_k(t) = -\int_0^t e^{i \int_0^{t'} \frac{E_k(t'') - E_k(t'')}{\hbar} dt''} \langle \phi_k(n, t') | \frac{\partial}{\partial t'} | \phi_0(x, t') \rangle dt', \qquad (A.16)$$

and the transition probability is

$$P_k(t) = |c_k(t)|^2. \qquad (A.17)$$

The transition probability is dependant on the shifting path $s(t)$ and the shifting time τ. For a linear shift, the total excitation probability into the first excited state is:

$$s(t) = \frac{t}{\tau} \qquad\qquad P_1(\tau) = \frac{\beta^2 \lambda^2}{8\omega^2} \frac{\sin(\omega\tau/2)^2}{\tau^2} \qquad (A.18)$$

The excitation probability is quite strongly modulated, as shown in fig. A.1 on the next page. This is different from the observed excitations (see fig. 3.11 on page 62). One possible explanation is the not perfectly linear response of the **EOM**-driver to the desired shifting-ramp. If the path $s(t)$ is smoothed out, the excitations are diminished:

$$s(t) = -2\left(\frac{t}{\tau}\right)^3 + 3\left(\frac{t}{\tau}\right)^2$$
$$P_1(\tau) = \frac{9\beta^2\lambda^2}{2\omega^6} \frac{(\omega\tau\cos(\omega\tau/2) - 2\sin(\omega\tau/2))^2}{\tau^6} \qquad (A.19)$$

$$s(t) = \left(\frac{t}{\tau}\right)^3 \left(6\left(\frac{t}{\tau}\right)^2 - 15\left(\frac{t}{\tau}\right) + 10\right)$$
$$P_1(\tau) = \frac{450\beta^2\lambda^2}{\omega^{10}} \frac{(6\omega\tau\cos(\omega\tau/2) + (\omega^2\tau^2 - 12)\sin(\omega\tau/2))^2}{\tau^{10}} \qquad (A.20)$$

These are also plotted in fig. A.1. While they fit the measured results much better, the minimum allowable shifting time is increased for smoother shifting.
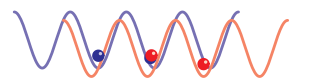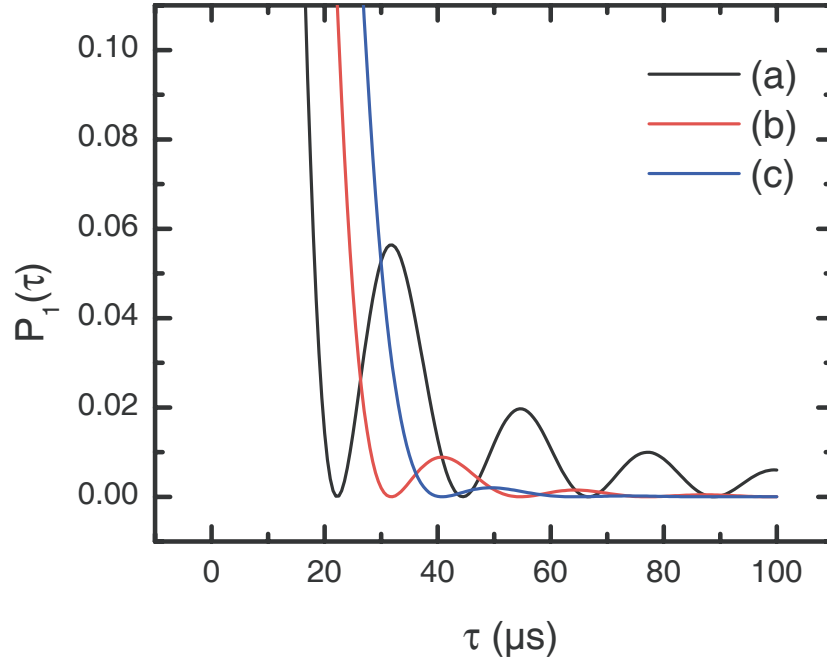
Figure A.1.: Excitation probability during shifting. The excitation probability to the first excited trap state P_1 is plotted over the shifting time τ. The simulated trapping frequency is $\omega = 2\pi \times 45\,\text{kHz}$. The curves correspond to the results of the different shifting paths of **(a)** eq. (A.18), **(b)** eq. (A.19) and **(c)** eq. (A.20).

A.3. The Free Flight Interferometer

In section 3.3.3 the free flight atom interferometer is introduced, where atoms are delocalised in the lattice and then interfere in a Time-of-Flight (TOF) expansion. The resulting pattern has the shape of a double-slit interference. Here, the interference pattern is calculated as a function of the distance d between the two parts of the atoms wave functions (d is in units of lattice sites) and the TOF expansion time t. The envelope of the interference pattern is not considered here, as it depends only on the single lattice site wave function.

The interferometer-sequence is as follows (compare the listing on page 67):

1. Start with one atom stored lattice site j.

$$|0\rangle_j$$

2. After the first $\pi/2$ microwave pulse.

$$\frac{1}{\sqrt{2}}(|0\rangle_j + i|1\rangle_j)$$

3. The first delocalisation step

$$\frac{1}{\sqrt{2}}(|0\rangle_j + i|1\rangle_{j+1})$$

4. For $d > 1$, there is a sequence of π-pulses and delocalisation steps. The final state after a total of d delocalisation steps is:

$$\frac{i^{d-1}}{\sqrt{2}}\left(|\tfrac{1}{2}(1+(-1)^d)\rangle_{j-\lfloor d/2\rfloor} + i|\tfrac{1}{2}(1-(-1)^d)\rangle_{j+\lceil d/2\rceil}\right)$$

5. After the second $\pi/2$ pulse with an arbitrary phase α.

$$\frac{i^d}{2}\left\{e^{(-1)^d i\alpha}|\tfrac{1}{2}(1-(-1)^d)\rangle_{j-\lfloor d/2\rfloor} + |\tfrac{1}{2}(1-(-1)^d)\rangle_{j+\lceil d/2\rceil}\right.$$
$$\left. -i|\tfrac{1}{2}(1+(-1)^d)\rangle_{j-\lfloor d/2\rfloor} + ie^{-(-1)^d i\alpha}|\tfrac{1}{2}(1+(-1)^d)\rangle_{j+\lceil d/2\rceil}\right\}$$

As we observe only one of the two states later, we can now neglect the terms for the other. The resultant state is not (easily) expressed in a closed form for even and odd d any more, but in two equations:

$$P(|1\rangle)_{\text{odd}} = \frac{i^d}{2}e^{-i\alpha}\left\{|1\rangle_{j-\frac{d-1}{2}} + e^{i\alpha}|1\rangle_{j+\frac{d+1}{2}}\right\} \tag{A.21a}$$

$$P(|1\rangle)_{\text{even}} = -\frac{i^{d+1}}{2}\left\{|1\rangle_{j-\frac{d}{2}} + e^{i(\pi-\alpha)}|1\rangle_{j+\frac{d}{2}}\right\} \tag{A.21b}$$

Now neglect the global phase and also the slight offset in position given by the rounding up and down for uneven d:

$$P(|1\rangle) = \frac{1}{2}\left\{|1\rangle_{j-d/2} + e^{i\phi}|1\rangle_{j+d/2}\right\}, \tag{A.22}$$
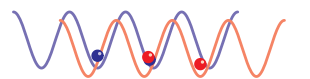
where ϕ is the phase set by the microwave-phase α. For this state, the interference pattern (without envelope) can be computed as the sum of two spherical waves with ignored $1/r$-term:

$$P(x, t_{\text{TOF}}) = \left| e^{if(x - \frac{d}{2}\frac{\lambda}{2}, t_{\text{TOF}})} + e^{i(f(x + \frac{d}{2}\frac{\lambda}{2}, t_{\text{TOF}}) + \phi)} \right|^2. \qquad (A.23)$$

Here x is the position along the interference pattern and t_{TOF} is the TOF time. The phase due to the TOF is the De Broglie wave length times the velocity integrated over t_{TOF}:

$$f(x, t_{\text{TOF}}) = \int_0^{t_{\text{TOF}}} \frac{mv}{\hbar} v \, dt \qquad (A.24)$$

with the velocity a sum of the linear motion to reach a distance x and the free-fall:

$$v = \sqrt{(\frac{x}{t_{\text{TOF}}})^2 + (gt)^2}.$$

Inserting (A.24) into (A.23) yields:

$$P(x, t_{\text{TOF}}) = \cos\left(\frac{1}{2}(\phi + \frac{dm\lambda}{\hbar t_{\text{TOF}}} x) \right) \qquad (A.25)$$

B. Selected Publications

Contained:

- M. GREINER, O. MANDEL, T. W. HÄNSCH, and I. BLOCH. *Collapse and revival of the matter wave field of a Bose-Einstein condensate.* Nature **419**, 51–54 (2002).

- O. MANDEL, M. GREINER, A. WIDERA, T. ROM, T. W. HÄNSCH, and I. BLOCH. *Coherent transport of neutral atoms in spin-dependent optical lattice potentials.* Phys. Rev. Lett. **91**, 010407–4 (2003).

- O. MANDEL, M. GREINER, A. WIDERA, T. ROM, T. W. HÄNSCH, and I. BLOCH. *Controlled collisions for multi-particle entanglement of optically trapped atoms.* Nature **425**, 937–940 (2003).

The first publication in the list, "Collapse and revival", contains the proof that the cold collisions in our experiment really only lead to a phase-evolution of the many atom state. This measurement is also presented in section 2.4.

The second publication, "Coherent transport", shows the first realisation of the shifting scheme discussed in section 3.3. Directly linked to that is the third publication, "Controlled collisions for multi-particle entanglement". This paper presents the creation of large, entangled states in a time independent of the size of the system.
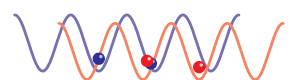
family formation predict that the memory of spin of the original unshattered parent body is lost[3], and existing models of spin angular momentum suggest that collisional evolution randomizes asteroid spin vectors regardless of their initial orientations[2], although the absolute timescale is uncertain. Here, I briefly identify two possible general explanations for future study.

One possibility is that randomly oriented gravitational aggregates from the initial collision have further fragmented, creating smaller objects that have the same spin obliquities as the remnants from which they were formed. Secondary fragmentation of the largest remnant of the initial break-up has previously been proposed to explain the existence of several objects of comparable size among the largest Koronis family members[16], but if the spin clusters were formed in this way then the absence of obvious corresponding associations in proper orbital elements also needs to be explained. To test this hypothesis, further work is needed to better understand the behaviour and evolution of gravitational aggregates.

A second possible explanation for spin clusters is that some dynamical process is aligning the obliquities and matching the rotation rates. Thermal effects can change obliquities and spin rates of small irregular asteroids, but calculations for Ida suggest that asteroids of comparable size are unlikely to have been substantially affected[17]. If a secular effect has clustered the spin vectors, then the present understanding of the timescale over which thermal processes have affected the spin cluster objects may be incomplete, or some nonthermal process may be at work. Finding similar clustering of spins for 20–40-km asteroids outside the Koronis family would support the hypothesis of a secular effect. □

1. Chapman, C. R., Paolicchi, P., Zappalà, V., Binzel, R. P. & Bell, J. F. in *Asteroids II* (eds Binzel, R. P., Gehrels, T. & Matthews, M. S.) 386–415 (Univ. Arizona Press, Tucson, 1989).
2. Binzel, R. P. Collisional evolution in the Eos and Koronis asteroid families: Observational and numerical results. *Icarus* **73**, 303–313 (1988).
3. Michel, P., Benz, W., Tanga, P. & Richardson, D. C. Collisions and gravitational reaccumulation: Forming asteroid families and satellites. *Science* **294**, 1696–1700 (2001).
4. Zappalà, V., Bendjoya, Ph., Cellino, A., Farinella, P. & Froeschle, C. Asteroid families: Search of a 12,487-asteroid sample using two different clustering techniques. *Icarus* **116**, 291–314 (1995).
5. Binzel, R. P. A photoelectric survey of 130 asteroids. *Icarus* **72**, 135–208 (1987).
6. Slivan, S. M. *Spin-Axis Alignment of Koronis Family Asteroids* PhD thesis, Massachusetts Institute of Technology (1995).
7. Slivan, S. M. & Binzel, R. P. Forty-eight new rotation lightcurves of 12 Koronis family asteroids. *Icarus* **124**, 452–470 (1996).
8. Slivan, S. M. *et al.* Spin vectors in the Koronis family: Comprehensive results from two independent analyses of 213 rotation lightcurves. *Icarus* (submitted).
9. Drummond, J. D., Weidenschilling, S. J., Chapman, C. R. & Davis, D. R. Photometric geodesy of main-belt asteroids. II. Analysis of lightcurves for poles, periods, and shapes. *Icarus* **76**, 19–77 (1988).
10. Kaasalainen, M. & Torppa, J. Optimization methods for asteroid lightcurve inversion. I. Shape determination. *Icarus* **153**, 24–36 (2001).
11. Kaasalainen, M., Torppa, J. & Muinonen, K. Optimization methods for asteroid lightcurve inversion. II. The complete inverse problem. *Icarus* **153**, 37–51 (2001).
12. Binzel, R. P. *et al.* Asteroid 243 Ida: Ground-based photometry and a pre-Galileo physical model. *Icarus* **105**, 310–325 (1993).
13. Davies, M. E. *et al.* The north pole direction and the control network of the asteroid 243 Ida. *Bull. Am. Astron. Soc.* **26**, 1154–1155 (1994).
14. Miller, I. & Freund, J. E. *Probability and Statistics for Engineers* (Prentice-Hall, Englewood Cliffs, New Jersey, 1977).
15. Belton, M. J. S. *et al.* First images of asteroid 243 Ida. *Science* **265**, 1543–1547 (1994).
16. Marzari, F., Davis, D. & Vanzani, V. Collisional evolution of asteroid families. *Icarus* **113**, 168–187 (1995).
17. Rubincam, D. P. Radiative spin-up and spin-down of small asteroids. *Icarus* **148**, 2–11 (2000).
18. Bowell, E., *et al.* in *Asteroids II* (eds Binzel, R. P., Gehrels, T. & Matthews, M. S.) 524–556 (Univ. Arizona Press, Tucson, 1989).
19. Landolt, A. U. *UVBRI* photometric standard stars around the celestial equator. *Astron. J.* **88**, 439–460 (1983).

Correspondence and requests for materials should be addressed to the author (e-mail: slivan@mit.edu).

---

letters to nature

Collapse and revival of the matter wave field of a Bose–Einstein condensate

Markus Greiner, Olaf Mandel, Theodor W. Hänsch & Immanuel Bloch

Sektion Physik, Ludwig-Maximilians-Universität, Schellingstrasse 4/III, D-80799 Munich, Germany, and Max-Planck-Institut für Quantenoptik, D-85748 Garching, Germany

A Bose–Einstein condensate represents the most 'classical' form of a matter wave, just as an optical laser emits the most classical form of an electromagnetic wave. Nevertheless, the matter wave field has a quantized structure owing to the granularity of the discrete underlying atoms. Although such a field is usually assumed to be intrinsically stable (apart from incoherent loss processes), this is no longer true when the condensate is in a coherent superposition of different atom number states[1–6]. For example, in a Bose–Einstein condensate confined by a three-dimensional optical lattice, each potential well can be prepared in a coherent superposition of different atom number states, with constant relative phases between neighbouring lattice sites. It is then natural to ask how the individual matter wave fields and their relative phases evolve. Here we use such a set-up to investigate these questions experimentally, observing that the matter wave field of the Bose–Einstein condensate undergoes a periodic series of collapses and revivals; this behaviour is directly demonstrated in the dynamical evolution of the multiple matter wave interference pattern. We attribute the oscillations to the quantized structure of the matter wave field and the collisions between individual atoms.

In order to determine the evolution with time of a many-atom state with repulsive interactions in a confining potential, we first assume that all atoms occupy only the ground state of the external potential. The hamiltonian governing the system after subtracting the ground-state energy of the external potential is then solely determined by the interaction energy between the atoms:

$$\hat{H} = \frac{1}{2} U \hat{n}(\hat{n} - 1) \tag{1}$$

Here $\hat{n}$ counts the number of atoms in the confining potential, and U is the on-site interaction matrix element that characterizes the energy cost due to the repulsive interactions when a second atom is added to the potential well. It can be related to the *s*-wave scattering length a and the ground-state wavefunction $w(\mathbf{x})$ through $U = 4\pi\hbar^2 a/m \int |w(\mathbf{x})|^4 \, d^3x$, as long as the vibrational level spacing of the external potential is large compared with the interaction energy. The eigenstates of the above hamiltonian are Fock states $|n\rangle$ in the atom number, with eigenenergies $E_n = Un(n-1)/2$. The evolution with time (t) of such an n-particle state is then simply given by $|n\rangle(t) = |n\rangle(0) \times \exp(-iE_n t/\hbar)$, where $\hbar$ is Planck's constant (h) divided by 2π.

We now consider a coherent state $|\alpha\rangle$ (see, for example, ref. 7) of the atomic matter field in a potential well. Such a coherent state with a complex amplitude α and an average number of atoms $\bar{n} = |\alpha|^2$ can be expressed as a superposition of different number states $|n\rangle$ such that $|\alpha\rangle = \exp(-|\alpha|^2/2)\sum_n \frac{\alpha^n}{\sqrt{n!}}|n\rangle$. Now the system is in a superposition of different eigenstates, which evolve in time according to their eigenenergies E_n. This allows us to calculate the evolution with time of an initially coherent state:

$$|\alpha\rangle(t) = e^{-|\alpha|^2/2}\sum_n \frac{\alpha^n}{\sqrt{n!}} e^{-i\frac{1}{2}Un(n-1)t/\hbar}|n\rangle \tag{2}$$

Evaluating the atomic field operator $\hat{a}$ for such a state then yields the
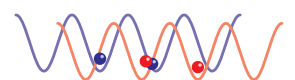
letters to nature
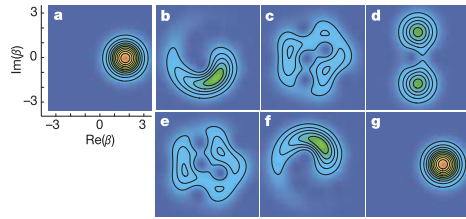
Figure 1 Quantum dynamics of a coherent state owing to cold collisions. The images **a**–**g** show the overlap $|\langle \beta | \alpha(t) \rangle|^2$ of an arbitrary coherent state $|\beta\rangle$ with complex amplitude β with the dynamically evolved quantum state $|\alpha\rangle(t)$ (see equation (2)) for an average number of $|\alpha|^2 = 3$ atoms at different times t. **a**, $t = 0\ h/U$; **b**, $0.1\ h/U$; **c**, $0.4\ h/U$; **d**, $0.5\ h/U$; **e**, $0.6\ h/U$; **f**, $0.9\ h/U$; and **g**, h/U. Initially, the phase of the macroscopic matter wave field becomes more and more uncertain as time evolves (**b**), but remarkably at $t_{rev}/2$ (**d**), when the macroscopic field has collapsed such that $\psi \approx 0$, the system has evolved into an exact 'Schrödinger cat' state of two coherent states. These two states are 180° out of phase, and therefore lead to a vanishing macroscopic field ψ at these times. More generally, we can show that at certain rational fractions of the revival time t_{rev}, the system evolves into other exact superpositions of coherent states—for example, at $t_{rev}/4$, four coherent states, or at $t_{rev}/3$, three coherent states[2,4]. A full revival of the initial coherent state is then reached at $t = h/U$. In the graph, red denotes maximum overlap and blue vanishing overlap with 10 contour lines in between.

macroscopic matter wave field $\psi = \langle \alpha(t) | \hat{a} | \alpha(t) \rangle$, which has an intriguing dynamical evolution. At first, the different phase evolutions of the atom number states lead to a collapse of ψ. However, at integer multiples of the revival time $t_{rev} = h/U$ all phase factors in the sum of equation (2) re-phase modulo 2π, leading to a perfect revival of the initial coherent state. The collapse time t_c depends on the variance σ_n^2 of the atom number distribution, such that $t_c \approx$

t_{rev}/σ_n (see refs 1–5). A more detailed picture of the dynamical evolution of ψ can be seen in Fig. 1, where the overlap of an arbitrary coherent state $|\beta\rangle$ with the state $|\alpha\rangle$ (t) is shown for different evolution times up to the first revival time of the many-body state[8,9].

In our experiment, we create coherent states of the matter wave field in a potential well, by loading a magnetically trapped Bose–Einstein condensate into a three-dimensional optical lattice potential. For low potential depths, where the tunnelling energy J is much larger than the on-site repulsive interaction energy U in a single well, each atom is spread out over all lattice sites. For the case of a homogeneous system with N atoms and M lattice sites, the many-body state can then be written in second quantization as a product of identical single-particle Bloch waves with zero quasi-momentum $|\Psi\rangle_{U/J=0} \propto \left(\sum_{i=1}^{M} \hat{a}_i^\dagger \right)^N |0\rangle$. It can be approximated by a product over single-site many-body states $|\phi_i\rangle$, such that $|\Psi\rangle_{U/J=0} \approx \prod_{i=1}^{M} |\phi_i\rangle$. In the limit of large N and M, the atom number distribution of $|\phi_i\rangle$ in each potential well is poissonian and almost identical to that of a coherent state. Furthermore, all the matter waves in different potential wells are phase coherent, with constant relative phases between lattice sites. As the lattice potential depth V_A is increased and J decreases, the atom number distribution in each potential well becomes markedly subpoissonian[10] owing to the repulsive interactions between the atoms, even before entering the Mott insulating state[11–13]. After preparing superposition states $|\phi_i\rangle$ in each potential well, we increase the lattice potential depth rapidly in order to create isolated potential wells. The hamiltonian of equation (1) then determines the dynamical evolution of each of these potential wells.

The experimental set-up used here to create Bose–Einstein condensates in the three-dimensional lattice potential (see Methods) is similar to that used in our previous work[11,14,15]. Briefly, we start with a quasi-pure Bose–Einstein condensate of up to 2×10^5 ^{87}Rb atoms in the $|F = 2, m_F = 2\rangle$ state in a harmonic magnetic trapping potential with isotropic trapping frequencies of $\omega = 2\pi \times 24\ \text{Hz}$. Here F and m_F denote the total angular momentum
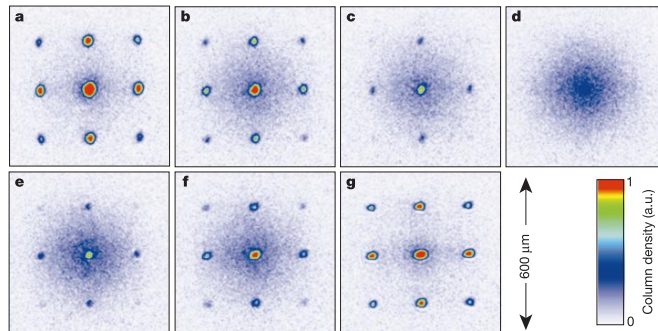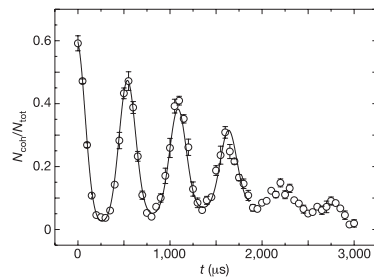

Figure 2 Dynamical evolution of the multiple matter wave interference pattern observed after jumping from a potential depth $V_A = 8\ E_r$ to a potential depth $V_B = 22\ E_r$ and a subsequent variable hold time t. After this hold time, all trapping potentials were shut off and absorption images were taken after a time-of-flight period of 16 ms. The hold times t were **a**, $0\ \mu s$; **b**, $100\ \mu s$; **c**, $150\ \mu s$; **d**, $250\ \mu s$; **e**, $350\ \mu s$; **f**, $400\ \mu s$; and **g**, $550\ \mu s$. At first, a distinct interference pattern is visible, showing that initially the system can be described by a macroscopic matter wave with phase coherence between individual potential wells. Then after a time of ~250 μs the interference pattern is completely lost. The vanishing of the interference pattern is caused by a collapse of the macroscopic matter wave field in each lattice potential well. But after a total hold time of 550 μs (**g**) the interference pattern is almost perfectly restored, showing that the macroscopic matter

wave field has revived. The atom number statistics in each well, however, remains constant throughout the dynamical evolution time. This is fundamentally different from the vanishing of the interference pattern with no further dynamical evolution, which is observed in the quantum phase transition to a Mott insulator, where Fock states are formed in each potential well. From the above images the number of coherent atoms N_{coh} is determined by first fitting a broad two-dimensional gaussian function to the incoherent background of atoms. The fitting region for the incoherent atoms excludes 130 μm × 130 μm squares around the interference peaks. Then the number of atoms in these squares is counted by a pixel-sum, from which the number of atoms in the incoherent gaussian background in these fields is subtracted to yield N_{coh}. a.u., arbitrary units.

letters to nature

and the magnetic quantum number of the atom's hyperfine state. In order to transfer the magnetically trapped atoms into the optical lattice potential, we slowly increase the intensity of the lattice laser beams over a time of 80 ms so that a lattice potential depth V_A of up to 11 recoil energies E_r (see Methods) is reached[11]. This value of V_A is chosen so that the system is still completely in the superfluid regime[16]. We then rapidly increase the lattice potential depth to a value V_B of up to 35 E_r within a time of 50 μs so that the tunnel coupling between neighbouring potential wells becomes negligible. The timescale for the jump in the potential depth is chosen such that it is fast compared with the tunnelling time between neighbouring potential wells, but sufficiently slow to ensure that all atoms remain in the vibrational ground state of each well. In this way, we preserve the atom number distribution of the potential depth V_A at the potential depth V_B.

We follow the dynamical evolution of the matter wave field after jumping to the potential depth V_B by holding the atoms in the optical lattice for different times t. After these hold times, we suddenly turn off the confining optical and magnetic trapping potentials and observe the resulting multiple matter wave interference pattern after a time-of-flight period of 16 ms. An example of such an evolution can be seen in Fig. 2, which shows the collapse and revival of the interference pattern over a time of 550 μs. This collapse and revival of the interference pattern is directly related to the collapses and revivals of the individual coherent matter wave fields in each potential well. It is important to note a crucial difference between the outcome of a collapse and revival experiment in a double-well system and our multiple-well system. In a double-well system, a perfect interference pattern would be observed in each single realization of the experiment for all times. However, when the matter wave fields have collapsed in both wells, this interference pattern would alternate randomly for each realization. Averaging

over several single realizations would then yield the ensemble average value $\psi = 0$ that indicates the randomness of the interference pattern associated with the collapse of the matter wave fields. For the multiple-well set-up used here, however, the interference pattern in a single realization of the experiment can only be observed if the matter wave fields in each potential well have constant relative phase to each other, which requires that $\psi \neq 0$. The matter wave field ψ is therefore directly connected to the visibility of the multiple matter wave interference pattern in a single realization of the experiment.

In order to analyse quantitatively the temporal evolution of the interference pattern, we evaluate the number of atoms in the first and central order interference peaks N_{coh} versus the total number of atoms N_{tot} in the time-of-flight images. In the optical lattice, the matter wave field in each potential well $\psi_i(t) = \langle \phi_i(t) | \hat{a}_i | \phi_i(t) \rangle$ collapses and revives owing to the nonlinear dynamics discussed above. In order to relate the time evolution of the global fraction of coherent atoms N_{coh}/N_{tot} to such a single-site time evolution $\psi_i(t)$ with $\bar{n}_i$ atoms on average on this lattice site, we sum the coherent fraction in each well over all M lattice sites: $N_{coh}/N_{tot} = 1/N_{tot} \sum_{i=1}^{M} |\psi_i(t)|^2$. This sum can be converted into an integral using the classical probability distribution $W(\bar{n})$ which describes the probability of finding a lattice site with an average number of $\bar{n}$ atoms. If the single-site dynamics is given by $\psi(t, \bar{n}, (U/J)_A, U_B)$, then the total number of coherent atoms can be determined by $N_{coh} = \int W(\bar{n}) |\psi(t, \bar{n}, (U/J)_A, U_B)|^2 d\bar{n}$. Using the Bose–Hubbard model and assuming a homogenous system, we are able to numerically calculate the initial atom number statistics on a single lattice site for finite U/J up to $U/J \approx 20$ and small $\bar{n}$ using a Gutzwiller ansatz[13,17]. This allows us to predict the dynamical evolution of the matter wave field on a single lattice site $\psi(t, \bar{n}, (U/J)_A, U_B)$. Figure 3 shows the experimentally determined evolution of N_{coh}/N_{tot} over time after jumping to the potential depth V_B. Up to five revivals are visible, after which a damping of the signal prevents further detection of revivals.

The revival of the matter wave field in each potential well is expected to occur at times that are multiples of h/U, independent of the atom number statistics in each well. Therefore, in our inhomogeneous system, the macroscopic interference pattern should revive at the same times on all sites. As the on-site matrix element U increases for greater potential depths, we expect the revival time to decrease as V_B increases. This is shown in Fig. 4, where we have measured the revival period for different final potential depths V_B. We find excellent agreement between an *ab initio* calculation of h/U

Figure 3 Number of coherent atoms relative to the total number of atoms monitored over time for the same experimental sequence as in Fig. 2. The solid line is a fit to the data assuming a sum of gaussians with constant widths and constant time separations, including an exponential damping and a linear background. The damping is mainly due to the following process: after jumping to a potential depth V_B and thereby abruptly changing the external confinement and the on-site matrix element U, we obtain a parabolic profile of the chemical potential over the cloud of atoms in the optical lattice, which leads to a broadening of the interference peaks over time. When the interference peaks become broader than the rectangular area in which they are counted, we cannot determine N_{coh} correctly any more, which explains the rather abrupt damping that can be seen—for example, between the third and fourth revival in the above figure. Furthermore, the difference in U of ~3% over the cloud of atoms contributes to the damping of N_{coh}/N_{tot} over time. The finite contrast in N_{coh}/N_{tot} of initially 60% can be attributed to atoms in higher-order momentum peaks (~10% of the total atom number), s-wave scattering spheres created during the expansion[14], a quantum depletion of the condensate for the initial potential depth of $V_A = 8 E_r$, and a finite condensate fraction due to the finite temperature of the system.

Figure 4 Revival period in the dynamical evolution of the interference pattern after jumping to different potential depths V_B from a potential depth of $V_A = 5.5 E_r$. The solid line is an *ab initio* calculation of h/U with no adjustable parameters based on a band structure calculation. In addition to the statistical uncertainties shown in the revival times, the experimental data points have a systematic uncertainty of 15% in the values for the potential depth.
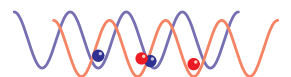
letters to nature

from a band structure calculation and our data points. The revivals also directly prove the quantization of the underlying Bose field, and provide experimental proof that collisions between atoms lead to a fully coherent collisional phase $Un(n-1)t/2\hbar$ of the $|n\rangle$-particle state over time, even on the level of individual pairs of atoms.

As we increase our initial lattice potential depth V_A, we expect the atom number distribution in each well to become markedly sub-poissonian owing to the increasing importance of the interactions as U/J increases. This in turn should lead to an increase of the collapse time, which depends on the variance of the superimposed number states. We have verified this by measuring the collapse time for different values of V_A (Fig. 5a). We can clearly observe a significant increase in the collapse time, when jumping from greater potential depths. For example, when jumping from $V_A = 11\ E_r$, t_c/t_{rev} is more than 50% larger than when jumping from $V_A = 4\ E_r$. This indicates that the atom number distribution in each potential well has indeed become subpoissonian, because for our experimental parameters the average atom number per lattice site, $\bar{n}_i$ remains almost constant when V_A is increased. A comparison of the collapse time for different initial potential depths V_A to a theoretical prediction is shown in Fig. 5b.

The observed collapse and revival of the macroscopic matter wave field of a Bose–Einstein condensate directly demonstrate behaviour of ultracold matter beyond mean-field theories. Furthermore, the

collapse times can serve as an independent, efficient probe of the atom number statistics in each potential well. It would be interesting to start from a Mott insulating state and use the coherent collisions between single atoms, which have been demonstrated here, to create a many-atom entangled state[18–20]. This highly entangled state could then serve as a promising starting point for quantum computing with neutral atoms[19,21]. □

Methods

Optical lattices

A three-dimensional array of microscopic potential wells is created by overlapping three orthogonal optical standing waves at the position of the Bose–Einstein condensate. The atoms are then trapped in the intensity maxima of the standing-wave light field owing to the resulting dipole force. The laser beams for the periodic potential are operated at a wavelength of $\lambda = 838$ nm with beam waists of $\sim 125\ \mu$m at the position of the Bose–Einstein condensate. This gaussian laser beam profile leads to an additional isotropic harmonic confinement of the atoms with trapping frequencies of 60 Hz for lattice potential depths of 20 E_r. Here E_r denotes the recoil energy $E_r = \hbar^2 k^2 / 2m$, with $k = 2\pi/\lambda$ being the wavevector of the laser light and m the mass of a single atom. In this configuration, we populate almost 150,000 lattice sites with an average atom number per lattice site of up to 2.5 in the centre of the lattice. The lattice structure is of simple cubic type, with a lattice spacing of $\lambda/2$ and oscillation frequencies in each lattice potential well of ~ 30 kHz for a potential depth of 20 E_r.

1. Wright, E. M., Walls, D. F. & Garrison, J. C. Collapses and revivals of Bose-Einstein condensates formed in small atomic samples. *Phys. Rev. Lett.* **77,** 2158–2161 (1996).
2. Wright, E. M., Wong, T., Collett, M. J., Tan, S. M. & Walls, D. F. Collapses and revivals in the interference between two Bose-Einstein condensates formed in small atomic samples. *Phys. Rev. A* **56,** 591–602 (1997).
3. Imamoglu, A., Lewenstein, M. & You, L. Inhibition of coherence in trapped Bose-Einstein condensates. *Phys. Rev. Lett.* **78,** 2511–2514 (1997).
4. Castin, Y. & Dalibard, J. Relative phase of two Bose-Einstein condensates. *Phys. Rev. A* **55,** 4330–4337 (1997).
5. Dunningham, J. A., Collett, M. J. & Walls, D. F. Quantum state of a trapped Bose-Einstein condensate. *Phys. Lett. A* **245,** 49–54 (1998).
6. Zhang, W. & Walls, D. F. Bosonic-degeneracy-induced quantum correlation in a nonlinear atomic beam splitter. *Phys. Rev. A* **52,** 4696–4703 (1995).
7. Walls, D. F. & Milburn, G. J. *Quantum Optics* (Springer, Berlin, 1994).
8. Milburn, G. J. & Holmes, C. A. Dissipative quantum and classical Liouville mechanics of the anharmonic oscillator. *Phys. Rev. Lett.* **56,** 2237–2240 (1986).
9. Daniel, D. J. & Milburn, G. J. Destruction of quantum coherence in a nonlinear oscillator via attenuation and amplification. *Phys. Rev. A* **39,** 4628–4640 (1989).
10. Orzel, C., Tuchman, A. K., Fenselau, M. L., Yasuda, M. & Kasevich, M. A. Squeezed states in a Bose-Einstein condensate. *Science* **291,** 2386–2389 (2001).
11. Greiner, M., Mandel, O., Esslinger, T., Hänsch, T. W. & Bloch, I. Quantum phase transition from a superfluid to a Mott insulator in a gas of ultracold atoms. *Nature* **415,** 39–44 (2002).
12. Fisher, M. P. A., Weichman, P. B., Grinstein, G. & Fisher, D. S. Boson localization and the superfluid-insulator transition. *Phys. Rev. B* **40,** 546–570 (1989).
13. Jaksch, D., Bruder, C., Cirac, J. I., Gardiner, C. W. & Zoller, P. Cold bosonic atoms in optical lattices. *Phys. Rev. Lett.* **81,** 3108–3111 (1998).
14. Greiner, M., Bloch, I., Mandel, O., Hänsch, T. W. & Esslinger, T. Exploring phase coherence in a 2D lattice of Bose-Einstein condensates. *Phys. Rev. Lett.* **87,** 160405-1–160405-4 (2001).
15. Greiner, M., Bloch, I., Hänsch, T. W. & Esslinger, T. Magnetic transport of trapped cold atoms over a large distance. *Phys. Rev. A* **63,** 031401-1–031401-4 (2001).
16. Cataliotti, F. S. *et al.* Josephson junction arrays with Bose-Einstein condensates. *Science* **293,** 843–846 (2001).
17. Rokhsar, D. S. & Kotliar, B. G. Gutzwiller projection for bosons. *Phys. Rev. B* **44,** 10328–10332 (1991).
18. Jaksch, D., Briegel, H. J., Cirac, J. I., Gardiner, C. W. & Zoller, P. Entanglement of atoms via cold controlled collisions. *Phys. Rev. Lett.* **82,** 1975–1978 (1999).
19. Briegel, H. J., Calarco, T., Jaksch, D., Cirac, J. I. & Zoller, P. Quantum computing with neutral atoms. *J. Mod. Opt.* **47,** 415–451 (2000).
20. Briegel, H. J. & Raussendorf, R. Persistent entanglement in arrays of interacting particles. *Phys. Rev. Lett.* **86,** 910–913 (2001).
21. Raussendorf, R. & Briegel, H. J. A one-way quantum computer. *Phys. Rev. Lett.* **86,** 5188–5191 (2001).
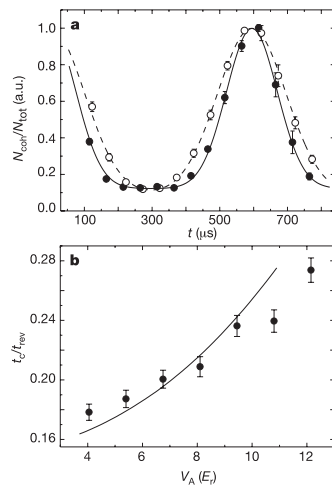
Figure 5 Influence of the atom number statistics on the collapse time. **a**, First revival observed in the ratio N_{coh}/N_{tot} after jumping from different initial potential depths $V_A = 4\ E_r$ (filled circles) and $V_A = 11\ E_r$ (open circles) to a potential depth of $V_B = 20\ E_r$. The data have been scaled to the same height in order to compare the widths of the collapse times, where the contrast of the curve at $V_A = 11\ E_r$ was 20% smaller than that for $V_A = 4\ E_r$. The solid and dashed line are fits to the data assuming a sum of two gaussians with constant widths t_c (measured as the 1/e half width of the gaussian), spaced by the corresponding revival time t_{rev} for the potential depth $V_B = 20\ E_r$. **b**, Collapse time t_c relative to the revival time t_{rev} after jumping from different potential depths V_A to a potential depth $V_B = 20\ E_r$. The solid line is an *ab initio* theoretical prediction based on the averaged time-evolution of the matter wave fields in each lattice potential well described in the text. Considering the systematic experimental uncertainties in the determination of the potential depths V_A of $\sim$15% and an uncertainty in the total atom number of $\sim$20%, we find a reasonable agreement between both the experimental data and the theoretical prediction. a.u., arbitrary units.

Coherent Transport of Neutral Atoms in Spin-Dependent Optical Lattice Potentials

Olaf Mandel, Markus Greiner, Artur Widera, Tim Rom, Theodor W. Hänsch, and Immanuel Bloch*

Ludwig-Maximilians-Universität, Schellingstrasse 4/III, 80799 Munich, Germany
Max-Planck-Institut für Quantenoptik, 85748 Garching, Germany
(Received 13 January 2003; published 3 July 2003)

We demonstrate the controlled coherent transport and splitting of atomic wave packets in spin-dependent optical lattice potentials. Such experiments open intriguing possibilities for quantum state engineering of many body states. After first preparing localized atomic wave functions in an optical lattice through a Mott insulating phase, we place each atom in a superposition of two internal spin states. Then state selective optical potentials are used to split the wave function of a single atom and transport the corresponding wave packets in two opposite directions. Coherence between the wave packets of an atom delocalized over up to seven lattice sites is demonstrated.

Over the past few years Bose-Einstein condensates (BEC's) in optical lattices have opened fascinating new experimental possibilities in condensed matter physics, atomic physics, quantum optics, and quantum information processing. Already now the study of Josephson junction-like effects [1,2], the formation of strongly correlated quantum phases [3–5], and the observation of the collapse and revival of the matter wave field of a BEC [6] have shown some of these diverse applications. In an optical lattice, neutral atoms can be trapped in the intensity maxima (or minima) of a standing wave light field due to the optical dipole force [7,8]. So far the optical potentials used have been mostly independent of the internal ground state of the atom. However, it has been suggested that by using spin-dependent periodic potentials one could bring atoms on different lattice sites into contact and thereby realize fundamental quantum gates [9–12], create large scale entanglement [13,14], excite spin waves [15,16], study quantum random walks [17], or form a universal quantum simulator to simulate fundamental complex condensed matter physics Hamiltonians [18]. Here we report on the realization of a coherent spin-dependent transport of neutral atoms in optical lattices [19,20]. We show how the wave packet of an atom that is initially localized to a single lattice site can be split and delocalized in a controlled and coherent way over a defined number of lattice sites.

In order to realize a spin-dependent transport for neutral atoms in optical lattices, a standing wave configuration formed by two counterpropagating laser beams with linear polarization vectors enclosing an angle θ has been proposed [9,13]. Such a standing wave light field can be decomposed into a superposition of a σ^+ and σ^- polarized standing wave laser field, giving rise to lattice potentials $V_+(x, \theta) = V_{max}\cos^2(kx + \theta/2)$ and $V_-(x, \theta) = V_{max}\cos^2(kx - \theta/2)$. Here k is the wave vector of the laser light used for the standing wave and V_{max} is the potential depth of the lattice. By changing the polarization angle θ one can thereby control the separation between the two

potentials $\Delta x = \theta/180° \cdot \lambda_x/2$. When increasing θ, both potentials shift in opposite directions and overlap again when $\theta = n \cdot 180°$, with n being an integer. For a spin-dependent transfer two internal spin states of the atom should be used, where one spin state dominantly experiences the $V_+(x, \theta)$ potential and the other spin state mainly experiences the $V_-(x, \theta)$ dipole force potential. Such a situation can be realized in rubidium by tuning the wavelength of the optical lattice laser to a value of $\lambda_x = 785$ nm between the fine structure splitting of the rubidium $D1$ and $D2$ transitions. Then the dipole potential experienced by an atom in, e.g., the $|1\rangle \equiv |F = 2, m_F = -2\rangle$ state is given by $V_1(x, \theta) = V_-(x, \theta)$ and that for an atom in the $|0\rangle \equiv |F = 1, m_F = -1\rangle$ state is given by $V_0(x, \theta) = 3/4V_+(x, \theta) + 1/4V_-(x, \theta)$. If an atom is now first placed in a coherent superposition of both internal states $1/\sqrt{2}(|0\rangle + i|1\rangle)$ and the polarization angle θ is continuously increased, the spatial wave packet of the atom is split with both components moving in opposite directions.

As in our previous experiments, Bose-Einstein condensates of up to 3×10^5 atoms are created in the $|F = 1, m_F = -1\rangle$ hyperfine state in a harmonic magnetic trap with almost isotropic oscillation frequencies of $\omega = 2\pi \times 16$ Hz. A three dimensional lattice potential is then superimposed on the Bose-Einstein condensate and the intensity raised in order to drive the system into a Mott insulating phase [5]. The atoms are thereby localized to individual lattice sites with no long range phase coherence. Tunneling between neighboring lattice sites is suppressed and irrelevant for the observed dynamics of the experiment. Two of the three orthogonal standing wave light fields forming the lattice potential are operated at a wavelength of $\lambda_{y,z} = 840$ nm. For the third standing wave field along the horizontal x direction a laser at a wavelength of $\lambda_x = 785$ nm is used. Along this axis a quarter wave plate and an electro-optical modulator (EOM) allow us to dynamically rotate the polarization vector of the retroreflected laser beam through an angle θ
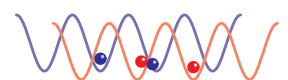
by applying an appropriate voltage to the EOM (see Fig. 1). Initially the polarization angle θ is set to a lin $\parallel$ lin polarization configuration. After reaching the Mott insulating phase we completely turn off the harmonic magnetic trapping potential but maintain a 1 G homogeneous magnetic field along the x direction in order to preserve the spin polarization of the atoms. This homogeneous field is actively stabilized to an accuracy of ≈ 1 mG. Shortly before moving the atoms along this standing wave direction we adiabatically turn off the lattice potentials along the y and z directions. This is done in order to reduce the interaction energy, which strongly depends on the confinement of the atoms at a single lattice site. We can thereby study the transport process itself at a single-particle level, without having to take into account the phase shifts in the many body state that result from a coherent collisional interaction between atoms.

By using microwave radiation around 6.8 GHz we are able to drive Rabi oscillations between the $|0\rangle$ and the $|1\rangle$ state with resonant Rabi frequencies of $\Omega = 2\pi \times 40$ kHz, such that, e.g., a π pulse can be achieved in a time of 12.5 μs. The microwave field therefore allows us to place the atom into an arbitrary superposition of the two internal states $|0\rangle$ or $|1\rangle$.

During the shifting process of the atoms it is crucial to avoid unwanted vibrational excitations, especially if the shifting process would be repeated frequently. We therefore analyze the time scale for such a movement process in the following way. First the atom is placed either in state $|0\rangle$ or state $|1\rangle$ by using microwave pulses in a standing wave lin $\parallel$ lin polarization configuration. Then we rotate the polarization to an angle $\theta = 180°$ in a linear ramp within a time τ, such that again a lin $\parallel$ lin polarization configuration is achieved. However, during this process the atoms will have moved by a distance $\pm \lambda_x/4$ depending on their internal state. In order to determine whether any higher lying vibrational states have been populated, we adiabatically turn off the lattice potential within a time of 500 μs. The population of the energy bands is then mapped onto the population of the corresponding Brillouin zones [21,22]. By counting the num-

ber of atoms outside of the first Brillouin zone of the system relative to the total number of atoms we are able to determine the fraction of vibrationally excited atoms after the shifting of the lattice potential (see Fig. 2). For a perfectly linear ramp with infinite acceleration at the beginning and ending of the ramp one would expect the fraction of atoms in the first vibrational state to be given by $|c_1(\tau)|^2 = 2v^2/(a_0\omega)^2\sin^2(\omega\tau/2)$, where $v = \lambda_x/(4\tau)$ is the shift velocity, a_0 is the size of the ground state harmonic oscillator wave function, and ω is the vibrational frequency on each lattice site.
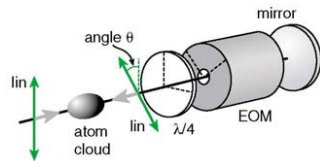
We have measured the vibrational frequencies on a lattice site for different polarization angles θ by slightly modulating the lattice position and observing a resonant transfer of atoms to the first excited vibrational state. For atoms in the $|1\rangle$ state the vibrational frequencies remain constant for different polarization angles θ as the lattice potential depth $V_1(x, \theta)$ remains constant. However, for atoms in the $|0\rangle$ state the lattice potential depth $V_0(x, \theta)$ decreases to 50% in a lin$\perp$lin configuration. In order to reduce this effect we tilt the EOM by 3° and thereby decrease the strength of the σ^- standing wave but increase the strength of the σ^+ standing wave in such a polarization configuration. Then both trapping frequencies for the $|0\rangle$ and the $|1\rangle$ state decrease to approximately 85% in a lin$\perp$lin configuration relative to their initial value of $\omega = 2\pi \times 45$ kHz in a lin $\parallel$ lin standing wave configuration. For such trapping frequencies of ≈ 45 kHz during the transport process, the excitation probability should remain below 5% for shifting times longer than $\approx 2\pi/\omega_x$, taking into account the finite bandwidth of our
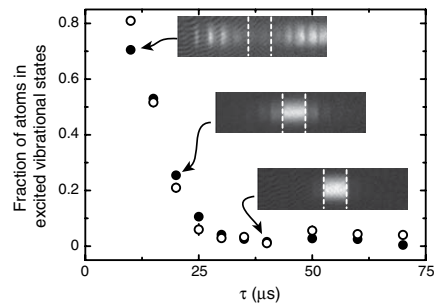
FIG. 2.   Fraction of atoms in excited vibrational states after moving the lattice potential in a time τ over a distance of $\lambda_x/4$. Filled (hollow) circles denote atoms in the $|1\rangle$ ($|0\rangle$) state. The images show the population of the Brillouin zones when the lattice potential was adiabatically ramped down after the shifting process. These absorption images correspond to the $|1\rangle$ state and were taken after a time of flight period of 14 ms. The white dashed lines in the images denote the borders of the first Brillouin zone. Atoms within this Brillouin zone correspond to atoms in the vibrational ground state on each lattice site.

FIG. 1 (color online).   Schematic experimental setup. A one dimensional optical standing wave laser field is formed by two counterpropagating laser beams with linear polarizations. The polarization angle of the returning laser beam can be adjusted through an electro-optical modulator. The dashed lines indicate the principal axes of the wave plate and the EOM.
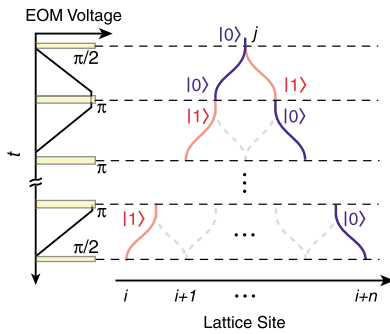
FIG. 3 (color online). General interferometer sequence used to delocalize an atom over an arbitrary number of lattice sites. Initially an atom is localized to the jth lattice site. The graph on the left indicates the EOM voltage and the sequence of $\pi/2$ and π microwave pulses that are applied over time (see text).
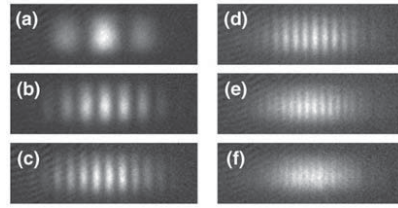

FIG. 4. Observed interference patterns in state $|1\rangle$ after initially localized atoms have been delocalized over (a) two, (b) three, (c) four, (d) five, (e) six, and (f) seven lattice sites using the interferometer sequence of Fig. 3. The time of flight period before taking the images was 14 ms and the horizontal size of each image is 880 μm. The shift time for this experiment was 50 μs.

high voltage amplifier. This finite bandwidth smooths the edges of our linear voltage ramp and thereby efficiently suppresses the oscillatory structure in the calculated excitation probability (see Fig. 2).

In order to verify the coherence of the spin-dependent transport we use the interferometer sequence of Fig. 3. Let us first consider the case of a single atom being initially localized to the jth lattice site. First, the atom is placed in a coherent superposition of the two internal states $|0\rangle_j$ and $|1\rangle_j$ with a $\pi/2$ microwave pulse (here the index denotes the position in the lattice). Then the polarization angle θ is rotated to 180°, such that the spatial wave packet of an atom in the $|0\rangle$ and the $|1\rangle$ state are transported in opposite directions. The final state after such a movement process is then given by $1/\sqrt{2}(|0\rangle_j + i\exp(i\beta)|1\rangle_{j+1})$, where the wave function of an atom has been delocalized over the jth and the $(j + 1)$th lattice site. The phase β between the two wave packets depends on the accumulated kinetic and potential energy phases in the transport process and in general will be nonzero. In order to reveal the coherence between the two wave packets, we apply a final $\pi/2$ microwave pulse that erases the which way information encoded in the hyperfine states. We then release the atoms from the confining potential by suddenly turning off the standing wave optical potential and observe the momentum distribution of the trapped atoms in the $|1\rangle$ state with absorption imaging after a time of flight period. As a result of the above sequence, the spatial wave packet of an atom in the $|0\rangle$ ($|1\rangle$) state is delocalized over two lattice sites resulting in a double slit momentum distribution $w(p) \propto \exp[-p^2/(\hbar/\sigma_x)^2] \cdot \cos^2(p\delta x_0/2\hbar + \beta/2)$ [see Fig. 4(a)], where δx_0 denotes the separation between the two wave packets and σ_x is the spatial extension of the Gaussian ground state wave function on each lattice site. In order to increase the separation be-

tween the two wave packets further, one could increase the polarization angle θ to further integer multiples of 180°. In practice, such an approach is, however, limited by the finite maximum voltage that can be applied to the EOM. In order to circumvent this limitation we apply a microwave π pulse after the polarization has been rotated to $\theta = +180°$, thereby swapping the role of the two hyperfine states. By then returning the polarization vector to $\theta = 0°$, we do not bring the two wave packets of an atom back to their original site but rather further increase the separation between the wave packets (see Fig. 3). The interlaced π pulse provides a further advantage of canceling inhomogeneous phase shifts acquired in the single-particle phase β in a spin-echo-like sequence. With increasing separation between the two wave packets the fringe spacing of the interference pattern further decreases (see Fig. 4). We have been able to observe such interference patterns for two wave packets delocalized over up to seven lattice sites [see Fig. 4(f)]. When
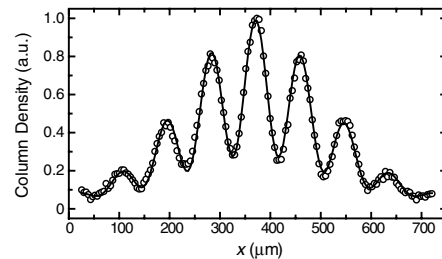
FIG. 5. Profile of the interference pattern obtained after delocalizing atoms over three lattice sites with a $\pi/2$-π-$\pi/2$ microwave pulse sequence. The solid line is a fit to the interference pattern with a sinusoidal modulation, a finite visibility ($\approx 60\%$), and a Gaussian envelope. The time of flight period was 15 ms.
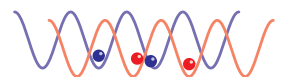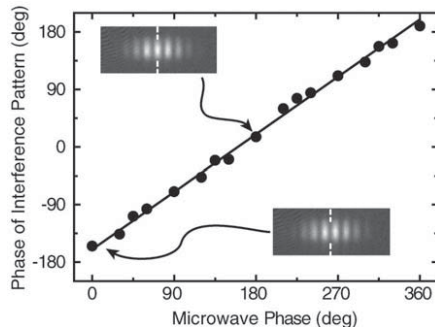
FIG. 6. Phase of the interference pattern vs the phase α of the final microwave $\pi/2$ pulse in a $\pi/2$-π-$\pi/2$ delocalization sequence (see Fig. 3). The absorption images show the measured interference pattern for $\alpha = 0°$ and $\alpha = 180°$ after a time of flight period of 15 ms. The solid line is a linear fit to the data with unity slope and a variable offset. The dashed lines in the images correspond to the center of the envelope of the interference pattern.

moving the atoms over up to three lattice sites, the visibility of the interference pattern remains rather high with up to 60% (see Fig. 5). These high contrast interference patterns directly prove the coherence of the transport process and also show that the single-particle phase β acquired for each atom is almost constant throughout the cloud of atoms in our system. If the movement process is repeated more often, inhomogeneously acquired phase shifts over the cloud of atoms significantly decrease the visibility.

For many further applications of the coherent spin-dependent transport it will also be crucial that the single-particle phase β is not only constant throughout the cloud of atoms within a single run of the experiment but is also reproducible between different sets of experiments. We have verified this by varying the phase α of the final microwave $\pi/2$ pulse in a sequence where an atom is delocalized over three lattice sites. In Fig. 6 we plot the experimentally measured phase of the interference pattern vs the phase α of the final microwave pulse obtained in different runs of the experiment. We find a high correlation between the detected phase of the interference pattern vs the phase of the applied microwave pulse which proves that indeed the single-particle phase is constant between different experiments and can be canceled via the phase of the final microwave pulse.

In conclusion we have demonstrated the coherent spin-dependent transport of neutral atoms in optical lattices, thereby showing an essential level of coherent control for many future applications. The method demonstrated here, e.g., provides a simple way to continuously tune the interspecies interactions by controlling the overlap of

the two ground state wave functions for the two spin states. Furthermore, if such a transport is carried out in a three dimensional lattice, where the on-site interaction energy between atoms is large, one could induce interactions between almost any two atoms on different lattice sites in a controlled way. Such controlled interactions of Ising or Heisenberg type could then be used to simulate the behavior of quantum magnets [15], to realize quantum gates between different atoms [9–12], or to generate highly entangled cluster states [10,13] that could form the basis of a one-way quantum computer [11].

*Electronic addresses: imb@mpq.mpg.de; http://www.mpq.mpg.de/~haensch/bec

[1] B. P. Anderson and M. A. Kasevich, Science **282**, 1686 (1998).
[2] F. S. Cataliotti *et al.*, Science **293**, 843 (2001).
[3] D. Jaksch *et al.*, Phys. Rev. Lett. **81**, 3108 (1998).
[4] C. Orzel *et al.*, Science **291**, 2386 (2001).
[5] M. Greiner *et al.*, Nature (London) **415**, 39 (2002).
[6] M. Greiner *et al.*, Nature (London) **419**, 51 (2002).
[7] P. S. Jessen and I. H. Deutsch, Adv. At. Mol. Opt. Phys. **37**, 95 (1996).
[8] R. Grimm, M. Weidemüller, and Y. B. Ovchinnikov, Adv. At. Mol. Opt. Phys. **42**, 95 (2000).
[9] G. K. Brennen *et al.*, Phys. Rev. Lett. **82**, 1060 (1999).
[10] H.-J. Briegel *et al.*, J. Mod. Opt. **47**, 415 (2000).
[11] R. Raussendorf and H.-J. Briegel, Phys. Rev. Lett. **86**, 5188 (2001).
[12] G. K. Brennen, I. H. Deutsch, and C. J. Williams, Phys. Rev. A **65**, 022313 (2002).
[13] D. Jaksch *et al.*, Phys. Rev. Lett. **82**, 1975 (1999).
[14] H.-J. Briegel and R. Raussendorf, Phys. Rev. Lett. **86**, 910 (2001).
[15] A. Sørensen and K. Mølmer, Phys. Rev. Lett. **83**, 2274 (1999).
[16] Spin waves have recently been observed in H. J. Lewandowski *et al.*, Phys. Rev. Lett. **88**, 070403 (2002); J. M. McGuirk *et al.*, Phys. Rev. Lett. **89**, 090402 (2002).
[17] W. Dür *et al.*, Phys. Rev. A **66**, 052319 (2002).
[18] E. Jané *et al.*, quant-ph/0207011
[19] Spin-dependent transport of neutral atoms has also been observed at National Institute of Standards and Technology. William Phillips (private communication).
[20] In a fixed polarization configuration, spin-dependent tunneling between two lattice sites has been observed in D. L. Haycock *et al.*, Phys. Rev. Lett. **85**, 3365 (2000).
[21] A. Kastberg *et al.*, Phys. Rev. Lett. **74**, 1542 (1995).
[22] M. Greiner *et al.*, Phys. Rev. Lett. **87**, 160405 (2001).

of 3.2×10^{12} cm for a prograde orbit of $J/(GM_{BH}/c) = 0.52$; the last stable retrograde orbit for that spin parameter has a period of 38 min at a radius of 4×10^{12} cm). Lense-Thirring precession and viscous (magnetic) torques will gradually force the accreting gas into the black hole's equatorial plane[29]. Recent numerical simulations indicate that a (prograde) disk analysis is appropriate to first order even for the hot accretion flow at the Galactic Centre[27]. ☐

1. Schödel, R. *et al.* A star in a 15.2 year orbit around the supermassive black hole at the centre of the Milky Way. *Nature* **419**, 694–696 (2002).
2. Ghez, A. M. *et al.* The first measurement of spectral lines in a short-period star bound to the Galaxy's central black hole: A paradox of youth. *Astrophys. J.* **586**, L127–L131 (2003).
3. Eisenhauer, F. *et al.* A geometric determination of the distance to the Galactic Center. *Astrophys. J. Lett.* (in the press); preprint at ⟨http://arXiv.org/astro-ph/0306220⟩ (2003).
4. Doeleman, S. S. *et al.* Structure of SgrA* at 86 GHz using VLBI closure quantities. *Astron. J.* **121**, 2610–2617 (2001).
5. Backer, D. C. & Sramek, R. A. Proper motion of the compact, nonthermal radio source in the Galactic Center, SgrA*. *Astrophys. J.* **524**, 805–815 (1999).
6. Baganoff, F. K. *et al.* Chandra X-ray spectroscopic imaging of SgrA* and the central parsec of the Galaxy. *Astrophys. J.* **591**, 891–915 (2003).
7. Hornstein, S. D. *et al.* Limits on the short-term variability of SgrA* in the near-IR. *Astrophys. J.* **577**, L9–L13 (2002).
8. Melia, F. & Falcke, H. The supermassive black hole at the Galactic Center. *Annu. Rev. Astron. Astrophys.* **39**, 309–352 (2001).
9. Lenzen, R., Hofmann, R., Bizenberger, P. & Tusche, A. CONICA: The high-resolution near-infrared camera for the ESO VLT. *Proc. SPIE* **3354** (IR Astronomical Instrumentation), 606–614 (1998).
10. Rousset, G. *et al.* Design of the Nasmyth adaptive optics system (NAOS) of the VLT. *Proc. SPIE* **3353** (Adaptive Optics Technology), 508–516 (1998).
11. Benlloch, S., Wilms, J., Edelson, R., Raqoob, T. & Staubert, T. Quasi-periodic oscillation in Seyfert galaxies: Significance levels. The case of Mrk 766. *Astrophys. J.* **562**, L121–L124 (2001).
12. Ghez, A. M. *et al.* Variable infrared emission from the supermassive black hole at the center of the Milky Way. *Astrophys. J. Lett.* (submitted); preprint at ⟨http://arXiv.org/astro-ph/0309076⟩ (2003).
13. Baganoff, F. K. Multi-wavelength monitoring of SgrA* during Chandra observations of multiple X-ray flares. *High Energy Astrophysics Division (HEAD)* AAS Abstr. 3.02, 35 (2003).
14. Alexander, T. & Sternberg, A. Near-IR microlensing of stars by the supermassive black hole in the Galactic Center. *Astrophys. J.* **520**, 137–148 (1999).
15. Yuan, F., Markoff, S. & Falcke, H. A jet-ADAF model for SgrA*. *Astron. Astrophys.* **854**, 854–863 (2002).
16. Liu, S. & Melia, F. New constraints on the nature of the radio emission in SgrA*. *Astrophys. J.* **561**, L77–L80 (2001).
17. Yuan, F., Quataert, E. & Narayan, R. Nonthermal electrons in radiatively inefficient flow models of SgrA*. *Astrophys. J.* (submitted); preprint at ⟨http://arXiv.org/astro-ph/0304125⟩ (2003).
18. Markoff, S., Falcke, H., Yuan, F. & Biermann, P. L. The nature of the 10ksec X-ray flare in SgrA*. *Astron. Astrophys.* **379**, L13–L16 (2001).
19. Baganoff, F. K. *et al.* Rapid X-ray flaring from the direction of the supermassive black hole at the Galactic Centre. *Nature* **413**, 45–48 (2001).
20. Porquet, D. *et al.* XMM-Newton observation of the brightest X-ray flare detected so far from SgrA*. *Astron. Astrophys.* **407**, L17–L20 (2003).
21. Zhao, J.-H. *et al.* Variability of SgrA*: Flares at 1 mm. *Astrophys. J.* **586**, L29–L32 (2003).
22. Miyazaki, A, Tstsumi, T. & Tsuboi, M. Flares of SgrA* at short submm wavelengths. *Astron. Nachr.* **324**, 3–9 (2003).
23. Nayakshin, S., Cuadra, J. & Sunyaev, R. X-ray flares from SgrA*: Star-disk interactions? *Astron. Astrophys.* (in the press); preprint at ⟨http://arXiv.org/astro-ph/0304126⟩ (2003).
24. Hollywood, J. M. & Melia, F. General relativistic effects on the infrared spectrum of thin accretion disks in active galactic nuclei: Application to SgrA*. *Astrophys. J. Suppl.* **112**, 423–455 (1997).
25. Bardeen, J. M., Press, W. M. & Teukolsky, S. A. Rotating black holes: Locally non-rotating frames, energy extraction and scalar synchrotron radiation. *Astrophys. J.* **178**, 347–369 (1972).
26. Melia, F., Bromley, C., Liu, S. & Walker, C. K. Measuring the black hole spin in SgrA*. *Astrophys. J.* **554**, L37–L40 (2001).
27. De Villiers, J.-P., Hawley, J. F. & Krolik, J. H. Magnetically driven accretion flows in the Kerr metric I: Models and overall structure. *Astrophys. J.* (submitted); preprint at ⟨http://arXiv.org/astro-ph/0307260⟩ (2003).
28. Nowak, M. A., Wagoner, R. V., Begelman, M. C. & Lehr, D. E. The 67 Hz feature in the black hole candidate GRS1915 + 105 as a possible diskoseismic mode. *Astrophys. J.* **477**, L91–L94 (1997).
29. Bardeen, J. & Pettersen, J. A. The Lense-Thirring effect and accretion disks around Kerr black holes. *Astrophys. J.* **105**, L65–L67 (1975).

---

letters to nature

Controlled collisions for multi-particle entanglement of optically trapped atoms

Olaf Mandel, Markus Greiner, Artur Widera, Tim Rom, Theodor W. Hänsch & Immanuel Bloch

Sektion Physik, Ludwig-Maximilians-Universität, Schellingstrasse 4/III, D-80799 Munich, Germany, and the Max-Planck-Institut für Quantenoptik, D-85748 Garching, Germany

Entanglement lies at the heart of quantum mechanics, and in recent years has been identified as an essential resource for quantum information processing and computation[1–4]. The experimentally challenging production of highly entangled multi-particle states is therefore important for investigating both fundamental physics and practical applications. Here we report the creation of highly entangled states of neutral atoms trapped in the periodic potential of an optical lattice. Controlled collisions between individual neighbouring atoms are used to realize an array of quantum gates, with massively parallel operation. We observe a coherent entangling–disentangling evolution in the many-body system, depending on the phase shift acquired during the collision between neighbouring atoms. Such dynamics are indicative of highly entangled many-body states; moreover, these are formed in a single operational step, independent of the size of the system[5,6].

Bose–Einstein condensates have been loaded into the periodic dipole force potential of a standing-wave laser field—a so-called optical lattice. In these systems, it has been possible to probe fundamental many-body quantum mechanics in an unprecedented way, with experiments ranging from Josephson junction tunnel arrays[7,8] to the observation of a Mott insulating state of quantum gases[9,10]. Important applications of atoms in a Mott insulating state in quantum information processing were envisaged early on. The Mott state itself, with one atom per lattice site, could act as a huge quantum memory, in which information would be stored in atoms at different lattice sites. Going beyond these ideas, it has been suggested that controlled interactions between atoms on neighbouring lattice sites could be used to realize a massively parallel array of neutral-atom quantum gates[5,11–14], with which a large multi-particle system could be highly entangled[6] in a single operational step. Furthermore, the repeated application of the quantum gate array could form the basis for a universal quantum simulator along the original ideas of Feynman for a quantum computer as a simulator of quantum dynamics[15–17].

The basic requirement for such control over the quantum state of a many-body system, including entanglement, is the precise microscopic control of the interactions between atoms on different lattice sites. To illustrate this, let us consider the case of two neighbouring atoms, initially in state $|\Psi\rangle = |0\rangle_j |0\rangle_{j+1}$ placed on the jth and $(j+1)$th lattice site of the periodic potential in the spin-state $|0\rangle$. First, both atoms are brought into a superposition of two internal states $|0\rangle$ and $|1\rangle$, using a $\pi/2$ pulse such that $|\Psi\rangle = (|0\rangle_j + |1\rangle_j)(|0\rangle_{j+1} + |1\rangle_{j+1})/2$. Then, a spin-dependent transport[18] splits the spatial wave packet of each atom such that the wave packet of the atom in state $|0\rangle$ moves to the left, whereas the wave packet of the atom in state $|1\rangle$ moves to the right. The two wave packets are separated by a distance $\Delta x = \lambda/2$, such that now $|\Psi\rangle = (|0\rangle_j |0\rangle_{j+1} + |0\rangle_j |1\rangle_{j+2} + |1\rangle_j |0\rangle_{j+1} + |1\rangle_{j+1} |1\rangle_{j+2})/2$, where in the notation atoms in state $|0\rangle$ have retained their original lattice site index and λ is the wavelength of the laser forming the optical periodic potential. The collisional interaction between the atoms[5,12,19] over a time t_{hold} will lead to a distinct phase shift $\varphi = U_{01} t_{hold}/\hbar$, when
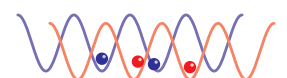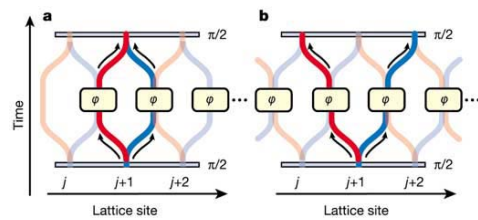
letters to nature

both atoms occupy the same lattice site $j + 1$ resulting in: $|\Psi\rangle = (|0\rangle_j|0\rangle_{j+1} + |0\rangle_j|1\rangle_{j+2} + e^{-i\varphi}|1\rangle_{j+1}|0\rangle_{j+2} + |1\rangle_{j+1}|1\rangle_{j+2})/2$. Here U_{01} is the onsite-interaction matrix element that characterizes the interaction energy when an atom in state $|0\rangle$ and an atom in state $|1\rangle$ are placed at the same lattice site and $\hbar$ is Planck's constant divided by 2π. Alternatively, a dipole–dipole interaction has been proposed[11] for generating a state-dependent phase shift φ. The final many-body state after bringing the atoms back to their original site and applying a last $\pi/2$ pulse can be expressed as $|\Psi\rangle = \frac{1+e^{-i\varphi}}{2}|1\rangle_j|1\rangle_{j+1} + \frac{1-e^{-i\varphi}}{2}|\text{BELL}\rangle$. Here $|\text{BELL}\rangle$ denotes the Bell-like state corresponding to $(|0\rangle_j(|0\rangle_{j+1} - |1\rangle_{j+1}) + |1\rangle_j(|0\rangle_{j+1} + |1\rangle_{j+1}))/2$.

This scheme can be generalized when more than two particles are placed next to each other, starting from a Mott insulating state of matter[9,10]. In such a Mott insulating state, atoms are localized to lattice sites, with a fixed number of atoms per site. For three particles for example, one can show that if $\varphi = (2n + 1)\pi$ (with n being an integer), so-called maximally entangled Greenberger–Horne–Zeilinger (GHZ) states[20] are realized. For a string of $N > 3$ atoms, where each atom interacts with its left- and right-hand neighbour (see Fig. 1), the entire string of atoms can be entangled to form so-called cluster states in a single operational step[5,6]. The controlled interactions described above can be viewed as being equivalent to an ensemble of quantum gates acting in parallel[3,5].

The experimental set-up used to load Bose–Einstein condensates into the three-dimensional optical lattice potential (see Methods section) is similar to our previous work[10,19]. Briefly, we start with a quasi-pure Bose–Einstein condensate of 10^5 ^{87}Rb atoms in the $|F = 1, m_F = -1\rangle$ state in a harmonic magnetic trapping potential with isotropic trapping frequencies of $\omega = 2\pi \times 14$ Hz. Here F and m_F denote the total angular momentum and the magnetic quantum number of the atom's hyperfine state. The three-dimensional periodic potential of an optical lattice is then ramped up over a period of 80 ms to a potential depth of $25E_r$, such that the Bose–Einstein condensate is converted into a Mott insulating state. Here

E_r denotes the recoil energy $E_r = \hbar^2 k^2/2m$, with $k = 2\pi/\lambda$ being the wavevector of the laser light and m the mass of a single atom. For our experimental parameters of atom number and harmonic confinement, such a Mott insulator should consist mainly of a central core with $n = 1$ atoms per lattice site[9,21,22]. The magnetic trapping potential is then rapidly switched off, but an actively stabilized magnetic offset field of 1 G along the transport direction is maintained to preserve the spin polarization of the atoms. With the optical standing wave along this direction, we are able to realize a spin-dependent transport of the atoms. After turning off the magnetic trapping field, we wait another 40 ms for the electronics to stabilize the magnetic offset field. Thereafter, 3.5 ms before the quantum gate sequence is initiated, we adiabatically increase the lattice depth along this axis to 34 E_r such that atoms remain in the vibrational ground state, are tightly confined and can be moved as fast as possible without excitations to higher vibrational states.

In the experiment, the two hyperfine states $|F = 1, m_F = -1\rangle \equiv |0\rangle$ and $|F = 2, m_F = -2\rangle \equiv |1\rangle$ form the logical basis of a single-atom qubit at each lattice site. These two states can be coupled

Figure 1 Schematic multiple quantum gate sequences based on controlled interactions. **a**, A chain of neutral atoms on different lattice sites is first placed in a coherent superposition of two spin-states $|0\rangle$ (red) and $|1\rangle$ (blue) with a $\pi/2$ microwave pulse. Then a spin-dependent transport is used to split the spatial wave packet of an atom, and move these two components along two opposite directions depending on their spin-state. The wave packets are separated by a lattice period such that each atom is brought into contact with its neighbouring atom. Owing to the collisional interaction between the atoms, a phase shift φ is acquired during a time t_{hold} that the atoms are held on a common lattice site depending on the spin-state of the atoms. After such a controlled collisional interaction, the wave packets of the individual atoms are returned to their original site and a final microwave $\pi/2$ pulse is applied to all atoms. This multiple quantum gate sequence can be equivalently described as a controllable quantum Ising interaction[6,12]. **b**, In a slight modification of such a sequence, the atoms are not returned to their original lattice site $j + 1$ but rather delocalized further over the jth and $(j + 2)$th lattice site after the controlled collisional interaction. The small arrows indicate the different paths that a single atom will follow during the multiple quantum gate sequence. Both sequences can be viewed as multi-particle interferometers, where the many-body output state of the interferometer can in general not be expressed as a product state of single-particle wavefunctions.

Figure 2 Experimentally measured Ramsey fringes for different hold times t_{hold} during which atoms undergo a controlled collisional interaction with their neighbouring atoms. The experimental sequence used is similar to the one in Fig. 1a, where atoms are returned to their original lattice site after the controlled interaction. The hold times t_{hold} are **a**, 30 μs, **b**, 210 μs and **c**, 450 μs. The relative number of atoms $N_{rel} = N_1/N_{tot}$ in the $|1\rangle$ state versus the phase α of the final microwave $\pi/2$ pulse is measured. A state-selective absorption imaging of the atom cloud is used to obtain N_1 after a time-of-flight period of 12 ms, and 110 μs thereafter the total atom number is measured to yield N_{tot}. The solid line indicates a fit of a sinusoidal function with variable amplitude and an offset to the data from which the visibility of the Ramsey fringe is extracted. The change in the phase of the Ramsey fringes for different hold times is mainly caused by the different exposure times of the two spin-states of an atom to differential light shifts of the optical lattice that are not perfectly cancelled in the spin-echo sequence.

letters to nature
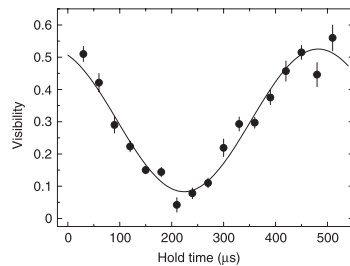
Figure 3 Visibility of Ramsey fringes versus hold times on neighbouring lattice sites for the experimental sequence similar to the one displayed in Fig. 1a. The solid line is a sinusoidal fit to the data including an offset and a finite amplitude. Such a sinusoidal behaviour of the visibility versus the collisional phase shift (determined by the hold time t_{hold}) is expected for a Mott insulating state with an occupancy of $n = 1$ atom per lattice site[23]. The maximum observed visibility is limited to 55% by inhomogeneities and time-dependent fluctuations of the lattice potentials throughout the cloud of atoms that are not perfectly compensated by the applied spin-echo sequence (see text).

coherently using resonant microwave radiation around 6.8 GHz. A $\pi/2$ pulse allows us to place the atom in a coherent superposition of the two states within a time of $6\,\mu s$. After creating such a coherent superposition, we use a spin-dependent transfer to split and move the spatial wavefunction of the atom over half a lattice spacing in two opposite directions depending on its internal state (see Fig. 1). Such a movement process is carried out within a time of $40\,\mu s$ in order to avoid any vibrational excitations[18] (the probability for excitations into higher-lying vibrational states was measured to be less than 3%). Atoms on neighbouring sites then interact for a variable amount of time t_{hold}. After half of the hold time, a microwave π pulse is applied. This spin-echo type π pulse is mainly used to cancel unwanted single-particle phase shifts, due, for example, to inhomogeneities in the trapping potentials. It does not, however, affect the non-trivial and crucial collisional phase shift due to the interactions between the atoms. After such a controlled collision, the atoms are moved back to their original site. Then a final $\pi/2$ microwave pulse with variable phase α is applied, and the atom number in state $|1\rangle$ relative to the total atom number is recorded.

The Ramsey fringes obtained in this way are shown in Fig. 2 for some different hold times t_{hold}, and for a wider range of hold times their visibility is plotted in Fig. 3. For short hold times, where no significant collisional phase shift is acquired, a Ramsey fringe with a

visibility of approximately 50% is recorded. For longer hold times we notice a strong reduction in the visibility of the Ramsey fringe, with an almost vanishing visibility of approximately 5% for a hold time of $210\,\mu s$ (Fig. 2b). This hold time corresponds to an acquired collisional phase shift of $\varphi = \pi$ for which we expect a minimum visibility if the system is becoming entangled.

For such an entangled state the probability for finding atoms in state $|1\rangle$ becomes independent of the phase α corresponding to a vanishing Ramsey fringe. This can be seen, for example, for the two-particle case: when the phase α of the last pulse is kept variable, the maximally entangled state for a collisional phase $\varphi = (2n+1)\pi$ can be expressed as: $|\Psi(\varphi = \pi)\rangle = \frac{1}{\sqrt{2}}(|0\rangle|-,\alpha\rangle + |1\rangle|+,\alpha\rangle)$, where $|-,\alpha\rangle \equiv \frac{1}{\sqrt{2}}(c_c^- |0\rangle - c_s^- |1\rangle)$ and $|+,\alpha\rangle \equiv \frac{1}{\sqrt{2}}(c_s^+ |0\rangle + c_c^+ |1\rangle)$ with $c_c^\pm \equiv e^{\pm i\alpha}\cos\alpha$ and $c_s^\pm \equiv -(\pm i\sin\alpha - 1)$. Here the probability for finding an atom in either spin-state, for example, $P(|1\rangle)$, is independent of α and equal to 1/2: $P(|1\rangle) = \frac{1}{8}\{|c_s^+|^2 + |c_s^-|^2 + 2|c_c^+|^2\} = \frac{1}{2}$. This indicates that no single-particle operation can place all atoms in either spin-state when a maximally entangled state has been created. The disappearance of the Ramsey fringe has been shown to occur not only for a two-particle system, but is a general feature for an arbitrary N-particle array of atoms that have been highly entangled with the above experimental sequence[3,23]. A vanishing Ramsey fringe can therefore in principle not distinguish between two-particle or multi-particle entanglement.

For longer hold times, the visibility of the Ramsey fringe increases again reaching a maximum of 55% for a hold time of $450\,\mu s$. Here the system becomes disentangled again, as the collisional phase shift is close to $\varphi = 2\pi$ and the Ramsey fringe is restored with maximum visibility.

The coherent 'entanglement oscillations' of the many-body system[6] are recorded for longer hold times by using the multi-particle interferometer sequence of Fig. 1b, where the atoms are not brought back to their original site but are rather kept delocalized[18]. This allows us to observe the Ramsey fringe of the previous sequence as a spatial interference pattern in a single run of the experiment in analogy to a double-slit interference experiment, when a state-selective time-of-flight detection is used. Images of such an interference pattern can be seen in Fig. 4 for different hold times t_{hold}. The coherent evolution again indicates the entangling–disentangling dynamics that the system undergoes for different collisional phase shifts φ (see Fig. 5).

Although the observed coherent dynamics in the vanishing and re-emergence of the Ramsey fringe does not provide a rigorous proof of a highly entangled multi-particle state, it is very indicative of such a state. So far, we cannot employ single-atom measurement techniques to detect correlations between individual atoms in the cluster that would provide a quantitative measurement for the size
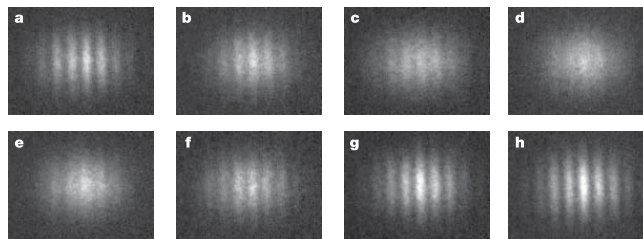
Figure 4 Spatial interference patterns recorded after applying the multiple quantum gate sequence of Fig. 1b for different collisional interaction times t_{hold}. The different hold times (μs) of 30 (**a**), 90 (**b**), 150 (**c**), 210 (**d**), 270 (**e**), 330 (**f**), 390 (**g**) and 450 (**h**) lead to different collisional phase shifts φ, ranging from $\varphi \approx 0$ (**a**) to just over $\varphi \approx 2\pi$ (**h**). The vanishing and reappearance of the interference pattern is caused by the coherent entangling–disentangling dynamics in the many-body system due to the controlled collisions between neighbouring atoms. The state-selective absorption images were obtained after a time-of-flight period of 11 ms.
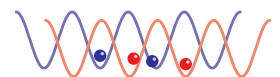
letters to nature
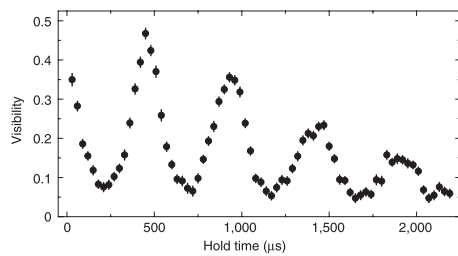
Figure 5 Visibility of the spatial interference patterns versus different collisional interaction times t_{hold}. We have been able to observe up to four entangling–disentangling cycles in the experiment. The reduced visibility for longer hold times is mainly caused by a dephasing over the trapped cloud of atoms due to inhomogeneities in the external potentials.

of the entangled many-body state. It is clear, however, that the minimum visibility observed in the Ramsey fringes is dependent on the quality of our initial Mott insulating state and the fidelity of the quantum gate operations. In an ideal experimental situation with perfect fidelity for the multi-particle quantum gates and a defect-free Mott insulating state, this visibility should vanish for a phase shift of $\varphi = (2n + 1)\pi$. For a finite fidelity of the quantum gates, caused, for example, by a 5% fractional error in the pulse areas of the microwave pulses, the minimum visibility would already increase to ~2%. If defects are present in the initial quantum state of the Mott insulator—for example, vacant lattice sites—then the entangled cluster state will not extend beyond this vacancy and the visibility of the Ramsey fringe will become non-zero owing to isolated atoms in the lattice. We have noticed, for example, that the quality of the Mott insulating state deteriorates owing to its prolonged uncompensated exposure to the potential gradient of gravity after the magnetic trapping potential is turned off. In addition to an imperfect creation of the Mott state, such vacancies could be caused by the superfluid shell of atoms surrounding the Mott insulating core[9,21,22] or spontaneous emission due to the laser light, which leads to excitations of approximately 5% of the atoms for our total experimental sequence times.

In our one-dimensional lattice shift the system is very susceptible to vacant lattice sites, as a defect will immediately limit the size of the cluster. However, the scheme can be extended to two or three dimensions by using two additional lattice shift operations along the remaining orthogonal lattice axes. As long as the filling factor of lattice sites exceeds the percolation threshold (31% for a three-dimensional simple cubic lattice system[24]) a large entangled cluster should be formed, making massive entanglement of 100,000 atoms possible in only three operational steps. For some of the applications of such a highly entangled state it will, however, be crucial to locate the position of the defects in the lattice.

In the future, it will be interesting to explore schemes for quantum computing that are based only on single-particle operations and measurements on such a cluster state[2]. Here the large amount of entanglement in a cluster state can be viewed as a resource for quantum computations. But now, even without the possibility of manipulating single atoms in the periodic potential, a quantum computer based on the controlled collisions demonstrated here could be able simulate a wide class of complex hamiltonians of condensed-matter physics that are translationally invariant[12,17]. □

Methods

Optical lattices

A three-dimensional array of microscopic potential wells is created by overlapping three orthogonal optical standing waves at the position of the Bose–Einstein condensate. In our case the atoms are trapped in the intensity maxima of the standing-wave light field owing to the resulting dipole force[25,26]. The laser beams for two of the periodic potentials are operated at a wavelength of $\lambda = 820$ nm with beam waists of approximately 210 μm at the position of the Bose–Einstein condensate. This gaussian laser beam profile leads to an additional isotropic harmonic confinement of the atoms with trapping frequencies of 40 Hz for lattice potential depths of $25E_r$. In this configuration, we populate almost 100,000 lattice sites with an average atom number per lattice site of up to 1 in the centre of the lattice. The lattice structure is of simple cubic type, with a lattice spacing of $\lambda/2$ and oscillation frequencies in each lattice potential well of approximately 30 kHz for a potential depth of $25 E_r$.

State-dependent lattice potentials

Along a third orthogonal direction a standing-wave potential at a wavelength of $\lambda_x = 785$ nm is used, formed by two counter-propagating laser beams with linear polarization vectors[5,11,18]. The angle θ between these polarization vectors can be dynamically adjusted through an electro-optical modulator and additional polarization optics. Such a lin-angle-lin polarization configuration can be decomposed into a σ^+ and a σ^- polarized standing-wave laser field, giving rise to potentials $V_+(x,\theta) = V_0\cos^2(k_x x + \theta/2)$ and $V_-(x,\theta) = V_0\cos^2(k_x x - \theta/2)$. Here V_0 is the potential depth of the lattice. By changing the polarization angle θ one can control the separation $\Delta x = (\theta/\pi)(\lambda_x/2)$ between the two potentials. When increasing θ, both potentials shift in opposite directions and overlap again for $\theta = n\pi$. For our experimental conditions, the dipole potential experienced by atoms in the $|1\rangle$ state is given by $V_-(x,\theta)$ and for atoms in the $|0\rangle$ state, it is dominated by the $V_+(x,\theta)$ potential[18]. For these laser beams, a waist of 150 μm has been used, resulting in a maximum potential depth of $34E_r$ and corresponding maximum vibrational trapping frequencies of 39 kHz.

1. Gottesman, D. & Chuang, I. L. Demonstrating the viability of universal quantum computation using teleportation and single-qubit operations. *Nature* **402**, 390–393 (1999).
2. Raussendorf, R. & Briegel, H. J. A one-way quantum computer. *Phys. Rev. Lett.* **86**, 5188–5191 (2001).
3. Briegel, H. J., Calarco, T., Jaksch, D., Cirac, J. I. & Zoller, P. Quantum computing with neutral atoms. *J. Mod. Opt.* **47**, 415–451 (2000).
4. Terhal, B. M., Wolf, M. M. & Doherty, A. C. Quantum entanglement: A modern perspective. *Phys. Today* **56**, 46–52 (2003).
5. Jaksch, D., Briegel, H. J., Cirac, J. I., Gardiner, C. W. & Zoller, P. Entanglement of atoms via cold controlled collisions. *Phys. Rev. Lett.* **82**, 1975–1978 (1999).
6. Briegel, H. J. & Raussendorf, R. Persistent entanglement in arrays of interacting particles. *Phys. Rev. Lett.* **86**, 910–913 (2001).
7. Anderson, B. P. & Kasevich, M. A. Macroscopic quantum interference from atomic tunnel arrays. *Science* **282**, 1686–1689 (1998).
8. Cataliotti, F. S. *et al.* Josephson junction arrays with Bose-Einstein condensates. *Science* **293**, 843–846 (2001).
9. Jaksch, D., Bruder, C., Cirac, J. I., Gardiner, C. W. & Zoller, P. Cold bosonic atoms in optical lattices. *Phys. Rev. Lett.* **81**, 3108–3111 (1998).
10. Greiner, M., Mandel, O., Esslinger, T., Hänsch, T. W. & Bloch, I. Quantum phase transition from a superfluid to a Mott insulator in a gas of ultracold atoms. *Nature* **415**, 39–44 (2002).
11. Brennen, G., Caves, C. M., Jessen, P. S. & Deutsch, I. H. Quantum logic gates in optical lattices. *Phys. Rev. Lett.* **82**, 1060–1063 (1999).
12. Sørensen, A. & Mølmer, K. Spin-spin interaction and spin squeezing in optical lattices. *Phys. Rev. Lett.* **83**, 2274–2277 (1999).
13. Brennen, G., Song, D. & Williams, C. J. A quantum computer architecture using nonlocal interactions. *Phys. Rev. A* **67**, 050302 (2003).
14. Pachos, J. K. & Knight, P. L. Quantum computation with a one-dimensional optical lattice. Preprint at 〈http://xxx.lanl.gov/quant-ph/0301084〉 (2003).
15. Feynman, R. P. Quantum mechanical computers. *Opt. News* **11**, 11–20 (1985).
16. Feynman, R. P. Quantum mechanical computers. *Found. Phys.* **16**, 507–531 (1986).
17. Jané, E., Vidal, G., Dür, W., Zoller, P. & Cirac, J. I. Simulation of quantum dynamics with quantum optical systems. *Quant. Inform. Comput.* **3**, 15–37 (2003).
18. Mandel, O. *et al.* Coherent transport of neutral atoms in spin-dependent optical lattice potentials. *Phys. Rev. Lett.* **91**, 010407 (2003).
19. Greiner, M., Mandel, O., Hänsch, T. W. & Bloch, I. Collapse and revival of the matter wave field of a Bose–Einstein condensate. *Nature* **419**, 51–54 (2002).
20. Greenberger, D. M., Horne, M. A. & Zeilinger, A. in *Bell's Theorem, Quantum Theory, and Conceptions of the Universe* (ed. Kafatos, M.) 69–72 (Kluwer Academic, Dordrecht, 1989).
21. Kashurnikov, V. A., Prokof´ef, N. V. & Svistunov, B. V. Revealing the superfluid–Mott-insulator transition in an optical lattice. *Phys. Rev. A* **66**, 031601 (2002).
22. Batrouni, G. G. *et al.* Mott domains of bosons confined on optical lattices. *Phys. Rev. Lett.* **89**, 117203 (2002).
23. Jaksch, D. Bose–Einstein condensation and applications. *Naturwissenschaftliche Fakultät*. PhD thesis, 97–197, Leopold-Franzens-Univ., Innsbruck (1999).
24. Stauffer, D. & Aharony, A. *Introduction to Percolation Theory* (Taylor and Francis, London, 1991).
25. Grimm, R., Weidemüller, M. & Ovchinnikov, Y. B. Optical dipole traps for neutral atoms. *Adv. At. Mol. Opt. Phys.* **42**, 95–170 (2000).
26. Jessen, P. S. & Deutsch, I. H. Optical Lattices. *Adv. At. Mol. Opt. Phys.* **37**, 95–139 (1996).

C. Data on Rubidium

Relevant ^{87}Rb data taken from ref. [99]. Scattering lengths taken directly from references::

Description	Symbol	Value	
Natural abundance	$\eta(^{87}\text{Rb})$	27.83(2) %	[100]
Atomic mass	m	86.909 180 520(15) u 1.443 160 60(11)$\times 10^{-22}$ g	[101]
Nuclear spin	I	3/2	
Landé g-factor	$g_J(5^2\text{S}_{1/2})$	2.002 331 13(20)	[102]
	$g_J(5^2\text{P}_{1/2})$	0.666	[99]
	$g_J(5^2\text{P}_{3/2})$	1.3362(13)	[102]
Nuclear g-factor	g_I	-0.000 995 141 4(10)	[102]
Wavelength (Vacuum)	λ_{D1}	794.978 850 9(8) nm	[103]
	λ_{D1}	780.241 209 686(13) nm	[103]
Lifetime P-states	$\tau_{1/2}$	27.70(4) ns	[104]
	$\tau_{3/2}$	26.24(4) ns	[104]
Natural line width	Γ_{D1}	36.10(5) $\times 10^6\,\text{s}^{-1}$ $2\pi \times 5.746(8)$ MHz	
	Γ_{D2}	38.11(6) $\times 10^6\,\text{s}^{-1}$ $2\pi \times 6.065(9)$ MHz	
Saturation intensity $\lvert\text{F}=2\rangle \rightarrow \lvert\text{F}'=3\rangle$ cycling	I_{sat}	1.669(9) mW/cm^2	[99]
Scattering lengths:	a_T	$106 \pm 4\,a_0$	[105]
Triplet, Singlet	a_S	$90 \pm 1\,a_0$	[105]
$\lvert\text{F}=1, m_{\text{F}}=-1\rangle$	a	$103 \pm 5\,a_0$	[106]
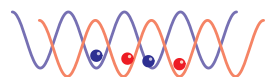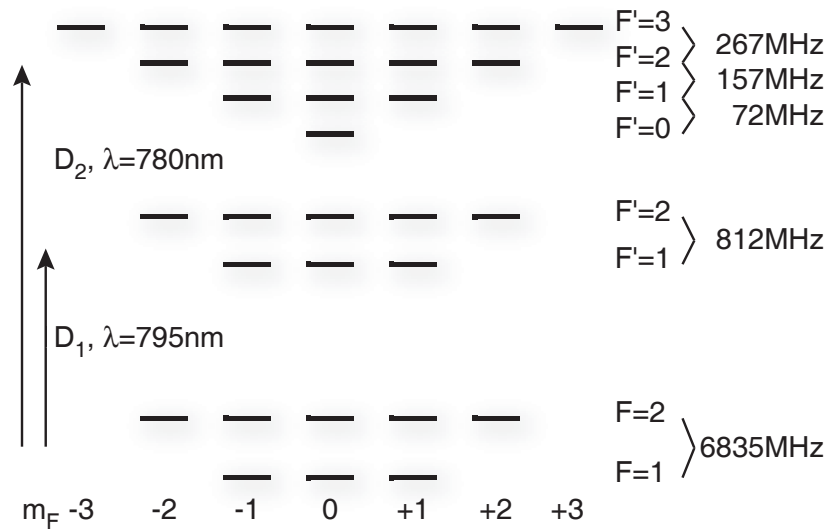
Figure C.1.: ^{87}Rb levelscheme.
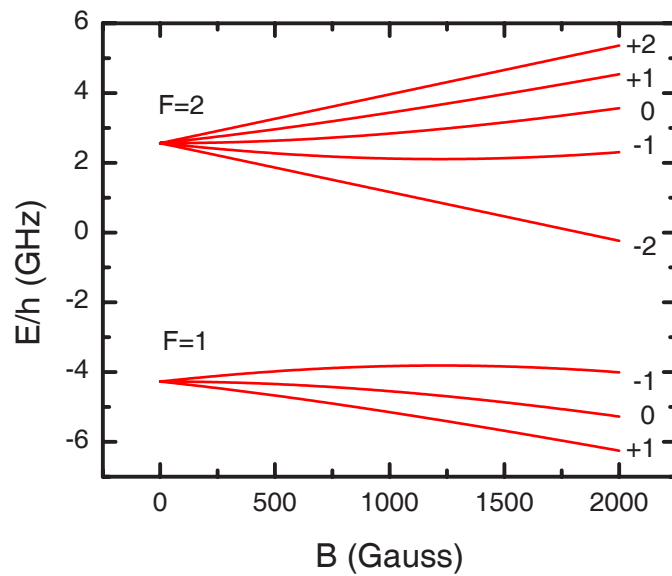
Figure C.2.: ^{87}Rb groundstate versus magnetic field. Plotted is the energy of the groundstate levels in frequency units. The m_F quantum numbers are given for each curve.

D. List of abbreviations

AOM Acusto-Optical Modulator
In a non-linear crystal, a high-frequency acoustic wave creates a lattice in the optical density. A laser beam passing through the AOM is shifted in its frequency by $\pm$ the frequency of the sonic wave.

BCS Bardeen-Cooper-Schrieffer
The theory to explain superconductivity was published by Bardeen, Cooper and Schrieffer, hence BCS. It uses a state, in which fermions form bosonic pairs, that then condense into a BEC. Here, the term is used in BCS transition, meaning the quantum phase transition into or out of this state.

BEC Bose-Einstein-Condensate
A Bose-Einstein-Condensate consists of cold bosons, that macroscopically occupy the trap ground state. All atoms in a BEC share a common wave function and are thus superfluid. For further properties of BECs, see [16].

CCD Charge Coupled Device
The light sensitive part of many modern cameras or shorthand for such a camera itself. A CCD (chip) consists of a two-dimensional array of light-sensitive pixels, that convert photons to electric charges. These are stored at the pixel, until after the exposure. Then, in a readout-row, the charges are shifted one pixel at a time into a readout-amplifier. After one row has been read completely, the image-field is shifted one line down, so that the next row of pixels can be read out.

CPU Central Processing Unit
The core of every modern computer, this chip is capable of conducting an arbitrary list of operations from a set of implemented functions. The commands, that control which operation is performed when and on which operand define the calculation the Central Processing Unit (CPU) performs, not the basic design of the chip.

EOM Electro-Optical Modulator

A material (often $LiNbO_3$ or KH_2PO_4(KDP)) with a high electro optic constants is submitted to a high electric field. The refractive index along certain crystal axis changes with the applied voltage. Depending on the geometry of applied field, beam polarisation and crystal orientation, the EOM can be used as a phase modulator or variable $\lambda/2$ plate.

FPGA Field Programmable Gate Array

Used for micro-chips that are divided into a large array of computation cells and interconnects. During initialisation of the chip, the function of each cell gets defined and the interconnects are routed according to an editable circuit description. A modern FPGA can contain over 200,000 logic cells and nearly 6 MBits of RAM (e.g. Xilinx 4VLX200).

GHZ Greenberger-Horne-Zeilinger

The GHZ state is an entangled state of $n = 3$ qubits (generalized GHZ for $n \geq 3$) that can be written as $|00\ldots0\rangle + |11\ldots1\rangle$ in some basis. This state is maximally entangled, but very fragile against measurements.

MOSFET Metal Oxide Semiconductor Field Effect Transistor

A solid state device comprised of a channel whose conductivity can be modulated by applying a voltage to a capacitor in the device. In our experiment, they are used as fast switches for large currents (several 100 A).

MOT Magneto-Optical Trap

The Magneto-Optical Trap has become the most common source for ultra-cold atoms in labs around the world. A combination of magnetic field gradients and laser-fields tuned slightly below an atomic resonance trap over 10^{11} atoms and cool them to temperatures of typically 10–100 μK. For more details on MOTs, see [25].

MI Mott-Insulator

In a Mott-Insulator, atoms distribute over a regular array of lattice sites such that interaction energy is minimized. This results in each lattice site having a single atom-number state, for the experiments considered here usually exactly one atom. This means, that a MI-state does not have a phase, as this requires a superposition of atom number states.

QUIC Quadrupole-Ioffe-Configuration

A Ioffe-Pritchard type magnetic trap made of three coils [38]. It works on small currents of $\approx 40\,\mathrm{A}$. The aspect-ratio of this trap is ≈ 10.

RF Radio-Frequency

An electromagnetic wave in the high kHz to MHz frequency range.

SF Superfluid

A Superfluid is a state featuring a defined phase, where the matter behaves like a wave. The BEC is a SF.

TA Tapered Amplifier

A laser, where a comparatively weak master laser is coupled into a trapezoid laser diode, where it is amplified in a single pass. The shape of the amplifier-chip guaranties spatial coherence of the emitted light, while at the same time keeping the energy-density on the chip-surface below the destruction limit.

TOF Time-of-Flight

Before taking an absorption image of an atom cloud, all trapping potentials are switched off and the cloud is allowed to expand in free flight for a Time-of-Flight. This scales the features of the system up for easier imaging while at the same time Fourier-converting the image. So our experimental images show the momentum-space, not the real space.

UHV Ultra-High-Vacuum

In our apparatus, two vacuum chambers are operated at pressures of 10^{-9} mbar and 10^{-11} mbar, respectively.

List of Figures

Danksagung

Diese Arbeit wäre nicht zustande gekommen, ohne die Hilfe vieler Förderer, Kollegen und Freunde. Ich möchte mich an dieser Stelle ganz herzlich bedanken bei:

- **Prof. T. W. Hänsch**, der mir den Einstieg in die spannende Welt der Quantenoptik ermöglicht hat. Er verbindet ein intuitives Verständnis der Physik mit einer fantastischen Begeisterung für clevere technische Details. Ausserdem lebt er deutlich vor, dass Computer durchaus mehr sein dürfen als nur Werkzeuge.

- Prof. **Immanuel Bloch**, der das Experiment von Anfang an betreut hat. Immanuels Art, wie er sich selbst bedingungslos für das Experiment einsetzt, haben viele Messungen sehr stark beschleunigt. Auch wenn Immanuel die Verbindung nach „draußen" gehalten hat, war er doch immer über sein Handy mit uns verbunden. . .

- **Markus Greiner**, der die BEC-Apparatur für diese Experimente gebaut hat. Markus geht mit einer spielerischen Leichtigkeit an neue Optik oder Elektronik heran. Seine Neugierde hat ihn im „normalen Leben" bis nach Tibet und beruflich bis ans JILA gebracht, wohin sie ihn wohl noch führt?

- **Artur Widera**, der sich unserer Gruppe zu Beginn der hier beschriebenen Experimente sehr Vorteil der Gruppe anschloss. Auf seine Unterstützung habe ich immer vertrauen können. Bei Arturs besonderem Geschick, Dinge anschaulich darzustellen, bin ich mir sicher, dass er Handlungsreisender in Sachen Physik wie Prof. Hänsch oder Immanuel wird, oder dass McKinsey ihn uns wegschnappt.

- **Tim Rom**, **Thorsten Best** und **Simon Fölling**, die mir während der letzten Jahre wunderbare Kollegen gewesen sind und mit denen zusammen ich den Gemeinheiten der Apparatur getrotzt habe. Während Simon jetzt an unserem Experiment weiterarbeitet, haben Tim und Thorsten in Mainz endlich Gelegenheit, ihr eigenes Experiment mit ^{40}K aufzubauen. Man darf gespannt sein!

Bibliography

[1] E. JANÉ, G. VIDAL, W. DÜR, P. ZOLLER, and J. I. CIRAC. *Simulation of quantum dynamics with quantum optical systems*. Quant. Inform. Comput. **3**, 15–37 (2003). Also available at arXiv:quant-ph/0207011.

[2] R. P. FEYNMAN. *Simulating physics with computers*. Int. J. of Theo. Phys. **21**, 467–488 (1982).

[3] R. P. FEYNMAN. *Quantum mechanical computers*. Found. Phys. **16**, 503–531 (1986).

[4] D. DEUTSCH. *Quantum theory, the church-turing principle and the universal quantum computer*. Proc. R. Soc. A **400**, 97–117 (1985).

[5] A. STEANE. *Quantum computing*. Rep. Prog. Phys. **61**, 117–173 (1998). Also available at arXiv:quant-ph/9708022.

[6] M. A. NIELSEN and I. L. CHUANG. *Quantum Computation and Quantum Information*. Cambridge University Press (2001). ISBN 0-521-63235-8.

[7] D. JAKSCH, C. BRUDER, J. I. CIRAC, C. W. GARDINER, and P. ZOLLER. *Cold bosonic atoms in optical lattices*. Phys. Rev. Lett. **81**, 3108–3111 (1998).

[8] V. FINKELSTEIN, P. R. BERMAN, and J. GUO. *One-dimensional laser cooling below the doppler limit*. Phys. Rev. A **45**, 1829–1842 (1992).

[9] D. JAKSCH, H.-J. BRIEGEL, J. I. CIRAC, C. W. GARDINER, and P. ZOLLER. *Entanglement of atoms via cold controlled collisions*. Phys. Rev. Lett. **82**, 1975–1978 (1999).

[10] D. M. GREENBERGER, M. A. HORNE, A. SHIMONY, and A. ZEILINGER. *Bell's theorem without inequalities*. Am. J. Phys. **58**, 1131–1143 (1990).

[11] H. J. BRIEGEL and R. RAUSSENDORF. *Persistent entanglement in arrays of interacting particles*. Phys. Rev. Lett. **86**, 910–913 (2001).

[12] M. GREINER. *Ultracold quantum gases in three-dimensional optical lattice potentials*. PhD thesis, Ludwig-Maximilians-Universität München (2003).

[13] M. H. ANDERSON, J. R. ENSHER, M. R. MATTHEWS, C. E. WIEMAN, and E. A. CORNELL. *Observation of Bose-Einstein condensation in a dilute atomic vapor*. Science **269**, 198–201 (1995).

[14] K. B. DAVIS, M.-O. MEWES, M. R. ANDREWS, N. J. VAN DRUTEN, D. S. DURFEE, D. M. KURN, and W. KETTERLE. *Bose-Einstein condensation in a gas of sodium atoms*. Phys. Rev. Lett. **75**, 3969–3973 (1995).

[15] C. C. BRADLEY, C. A. SACKETT, J. J. TOLLETT, and R. G. HULET. *Evidence of Bose-Einstein condensation in an atomic gas with attractive interactions*. Phys. Rev. Lett. **75**, 1687–1690 (1995). *ibid.* **79**, 1170 (1997).

[16] F. DALFOVO, S. GIORGINI, L. P. PITAEVSKII, and S. STRINGARI. *Theory of Bose-Einstein condensation in trapped gases*. Rev. Mod. Phys. **71**, 463–512 (1999).

[17] A. J. LEGGETT. *Bose-Einstein condensation in the alkali gases: Some fundamental concepts*. Rev. Mod. Phys. **73**, 307–356 (2001).

[18] A. S. PARKINS and D. F. WALLS. *The physics of trapped dilute-gas Bose-Einstein condensates*. Phys. Rep. **303**, 1–80 (1998).

[19] C. J. PETHICK and H. SMITH. *Bose-Einstein Condensation in Dilute Gases*. Cambridge University Press (2001). ISBN 0-521-66580-9.

[20] Y. CASTIN. *Bose-Einstein condensates in atomic gases: simple theoretical results*. arXiv:cond-mat/0105058 (2001).

[21] W. KETTERLE, D. S. DURFEE, and D. M. STAMPER-KURN. *Making, probing and understanding Bose-Einstein condensates*. In M. INGUSCIO, S. STRINGARI, and C. E. WIEMAN, editors, *Proceedings of the International School of Physics - Enrico Fermi*, pages 67–176. IOS Press (1999). ISBN 0-967-33555-8. Also available at arXiv:cond-mat/9904034.

[22] M. D. BARRETT, J. A. SAUER, and M. S. CHAPMAN. *All-optical formation of an atomic Bose-Einstein condensate*. Phys. Rev. Lett. **87**, 010404–4 (2001).

[23] T. WEBER, J. HERBIG, M. MARK, H.-C. NÄGERL, and R. GRIMM. *Bose-Einstein condensation of Cesium*. Science **299**, 232–235 (2003).

[24] E. L. RAAB, M. PRENTISS, A. CABLE, S. CHU, and D. E. PRITCHARD. *Trapping of neutral sodium atoms with radiation pressure*. Phys. Rev. Lett. **59**, 2631–2634 (1987).

[25] C. S. ADAMS and E. RIIS. *Laser cooling and trapping of neutral atoms*. Prog. Quant. Electr. **21**, 1–79 (1997).

[26] W. D. PHILLIPS. *Laser cooling and trapping of neutral atoms*. Rev. Mod. Phys. **70**, 721–741 (1998).

[27] K. E. GIBBLE, S. KASAPI, and S. CHU. *Improved magneto-optic trapping in a vapor cell*. Opt. Lett. **17**, 526 (1992).

[28] A. L. MIGDALL, J. V. PRODAN, W. D. PHILLIPS, T. H. BERGEMAN, and H. J. METCALF. *First observation of magnetically trapped neutral atoms*. Phys. Rev. Lett. **54**, 2596–2599 (1985).

[29] V. S. BAGNATO, G. P. LAFYATIS, A. G. MARTIN, E. L. RAAB, R. N. AHMAD-BITAR, and D. E. PRITCHARD. *Continuous stopping and trapping of neutral atoms*. Phys. Rev. Lett. **58**, 2194–2197 (1987).

[30] H. F. HESS, G. P. KOCHANSKI, J. M. DOYLE, N. MASUHARA, D. KLEPPNER, and T. J. GREYTAK. *Magnetic trapping of spin polarized atomic hydrogen*. Phys. Rev. Lett. **59**, 672–675 (1987).

[31] W. D. PHILLIPS, J. V. PRODAN, and H. J. METCALF. *Laser cooling and electromagnetic trapping of neutral atoms*. J. Opt. Soc. Am. B **2**, 1751–1767 (1985).

[32] M. GREINER, I. BLOCH, T. W. HÄNSCH, and T. ESSLINGER. *Magnetic transport of trapped cold atoms over a large distance*. Phys. Rev. A **63**, 031401–4 (2001).

[33] E. MAJORANA. *Atomi orientati in campo magnetico variabile*. Nuovo Cimento **9**, 43–50 (1932).

[34] K. B. DAVIS, M.-O. MEWES, M. A. JOFFE, M. R. ANDREWS, and W. KETTERLE. *Evaporative cooling of sodium atoms*. Phys. Rev. Lett. **74**, 5202–5205 (1995).
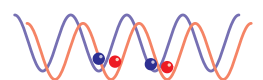
[35] W. PETRICH, M. H. ANDERSON, J. R. ENSHER, and E. A. CORNELL. *Stable, tightly confining magnetic trap for evaporative cooling of neutral atoms*. Phys. Rev. Lett. **74**, 3352–3355 (1995).

[36] D. E. PRITCHARD. *Cooling neutral atoms in a magnetic trap for precision spectroscopy*. Phys. Rev. Lett. **51**, 1336–1339 (1983).

[37] T. BERGEMAN, G. EREZ, and H. METCALF. *Magnetostatic trapping fields for neutral atoms*. Phys. Rev. A **35**, 1535–1546 (1987).

[38] T. ESSLINGER, I. BLOCH, and T. W. HÄNSCH. *Bose-Einstein condensation in a quadrupole-Ioffe-configuration trap*. Phys. Rev. A **58**, R2664–R2667 (1998).

[39] I. F. SILVERA and J. T. M. WALRAVEN. *Stabilization of atomic hydrogen at low temperature*. Phys. Rev. Lett. **44**, 164–168 (1980).

[40] H. F. HESS. *Evaporative cooling of magnetically trapped and compressed spin-polarized hydrogen*. Phys. Rev. B **34**, 3476–3479 (1986).

[41] N. MASUHARA, J. M. DOYLE, J. C. SANDBERG, D. KLEPPNER, T. J. GREYTAK, H. HESS, and G. P. KOCHANSKI. *Evaporative cooling of spin-polarized atomic hydrogen*. Phys. Rev. Lett. **61**, 935–938 (1988).

[42] J. M. DOYLE, J. C. SANDBERG, I. A. YU, C. L. CESAR, D. KLEPPNER, and T. J. GREYTAK. *Hydrogen in the submillikelvin regime: Sticking probability on superfluid ^4He*. Phys. Rev. Lett. **67**, 603–606 (1991).

[43] J. E. BJORKHOLM, R. E. FREEMAN, A. ASHKIN, and D. B. PEARSON. *Observation of focusing on neutral atoms by the dipole forces of resonance-radiation pressure*. Phys. Rev. Lett. **41**, 1361–1364 (1978).

[44] S. CHU, J. E. BJORKHOLM, A. ASHKIN, and A. CABLE. *Experimental observation of optically trapped atoms*. Phys. Rev. Lett. **57**, 314–317 (1986).

[45] R. GRIMM, M. WEIDEMÜLLER, and Y. B. OVCHINNIKOV. *Optical dipole traps for neutral atoms*, volume 42 of *Adv. At. Mol. Opt. Phys.*, pages 95–170. Academic Press (2000). ISBN 0-120-03842-0. Also available at arXiv:physics/9902072.

[46] P. S. JESSEN and I. H. DEUTSCH. *Optical Lattices*, volume 37 of *Adv. At. Mol. Opt. Phys.*, pages 95–138. Academic Press (1996). ISBN 0-120-03837-4.

[47] C. N. COHEN-TANNOUDJI. *Manipulating atoms with photons*. Rev. Mod. Phys. **70**, 707–719 (1998).

[48] C. S. ADAMS, M. SIGEL, and J. MLYNEK. *Atom optics*. Phys. Rep. **240**, 143–210 (1994).

[49] P. L. GOULD, G. A. RUFF, and D. E. PRITCHARD. *Diffraction of atoms by light: The near-resonant kapitza-dirac effect*. Phys. Rev. Lett. **56**, 827–830 (1986).

[50] P. J. MARTIN, B. G. OLDAKER, A. H. MIKLICH, and D. E. PRITCHARD. *Bragg scattering of atoms from a standing light wave*. Phys. Rev. Lett. **60**, 515–518 (1988).

[51] M. PRENTISS. *Bound by light*. Science **260**, 1078 (1993).

[52] A. HEMMERICH and T. W. HÄNSCH. *Two-dimesional atomic crystal bound by light*. Phys. Rev. Lett. **70**, 410–413 (1993).

[53] A. HEMMERICH, M. WEIDEMÜLLER, T. ESSLINGER, C. ZIMMER-MANN, and T. HÄNSCH. *Trapping atoms in a dark optical lattice*. Phys. Rev. Lett. **75**, 37–40 (1995).

[54] M. WEIDEMÜLLER, A. HEMMERICH, A. GÖRLITZ, T. ESSLINGER, and T. W. HÄNSCH. *Bragg diffraction in an atomic lattice bound by light*. Phys. Rev. Lett. **75**, 4583–4586 (1995).

[55] G. GRYNBERG, B. LOUNIS, P. VERKERK, J.-Y. COURTOIS, and C. SALOMON. *Quantized motion of cold cesium atoms in two- and three-dimensional optical potentials*. Phys. Rev. Lett. **70**, 2249–2252 (1993).

[56] A. GÖRLITZ, M. WEIDEMÜLLER, T. W. HÄNSCH, and A. HEMMERICH. *Observing the position spread of atomic wave packets*. Phys. Rev. Lett. **78**, 2096–2099 (1997).

[57] A. GÖRLITZ, T. KINOSHITA, T. W. HÄNSCH, and A. HEMMERICH. *Realization of bichromatic optical superlattices*. Phys. Rev. A **64**, 011401–4 (2001).

[58] M. GREINER, I. BLOCH, O. MANDEL, T. W. HÄNSCH, and T. ESSLINGER. *Exploring phase coherence in a 2D lattice of Bose-Einstein condensates*. Phys. Rev. Lett. **87**, 160405–4 (2001).

[59] N. W. ASHCROFT and N. D. MERMIN. *Solid State Physics*. Thomson Learning (1976). ISBN 0-030-83993-9.
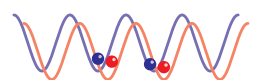
[60] C. KITTEL. *Introduction to Solid State Physics*. Wiley, 8. edition (2004). ISBN 0-471-41526-X.

[61] P. A. LEE and T. V. RAMAKRISHNAN. *Disordered electronic systems*. Rev. Mod. Phys. **57**, 287–337 (1985).

[62] M. P. A. FISHER, P. B. WEICHMAN, G. GRINSTEIN, and D. S. FISHER. *Boson localization and the superfluid-insulator transition*. Phys. Rev. B **40**, 546–570 (1989).

[63] K. SHESHADRI, H. R. KRISHNAMURTHY, R. PANDIT, and T. V. RAMAKRISHNAN. *Superfluid and insulating phases in an interacting-boson model: mean-field theory and the RPA*. Europhys. Lett. **22**, 257–263 (1993).

[64] J. K. FREERICKS and H. MONIEN. *Phase diagram of the bose-hubbard model*. Europhys. Lett. **26**, 545–550 (1994).

[65] D. VAN OOSTEN, P. VAN DER STRATEN, and H. T. C. STOOF. *Quantum phases in an optical lattice*. Phys. Rev. A **63**, 053601–11 (2001).

[66] T. D. KÜHNER and H. MONIEN. *Phases of the one-dimensional bose-hubbard model*. Phys. Rev. B **58**, R14741–R14744 (1998).

[67] S. SACHDEV. *Quantum Phase Transitions*. Cambridge University Press (1999). ISBN 0-521-58254-7.

[68] D. F. WALLS and G. J. MILBURN. *Quantum Optics*. Springer, Berlin (1995). ISBN 3-540-58831-0.

[69] C. COHEN-TANNOUDJI, B. DIU, and F. LALOE. *Quantum Mechanics*, volume 1. John Wiley & Sons Inc (1977). ISBN 0-471-16433-X.

[70] J. A. DUNNINGHAM and K. BURNETT. *Phase standard for Bose-Einstein condensates*. Phys. Rev. Lett. **82**, 3729–3733 (1999).

[71] M. GREINER, O. MANDEL, T. ESSLINGER, T. W. HÄNSCH, and I. BLOCH. *Quantum phase transition from a superfluid to a Mott insulator in a gas of ultracold atoms*. Nature **415**, 39–44 (2002).

[72] D. J. HEINZEN. *Ultracold atomic interactions*. In M. INGUSCIO, S. STRINGARI, and C. E. WIEMAN, editors, *Proceedings of the International School of Physics - Enrico Fermi*, pages 351–390. IOS Press (1999). ISBN 0-967-33555-8.

[73] J. DALIBARD. *Collisional dynamics of ultra-cold atomic gases*. In M. IN-GUSCIO, S. STRINGARI, and C. E. WIEMAN, editors, *Proceedings of the International School of Physics - Enrico Fermi*, pages 321–349. IOS Press (1999). ISBN 0-967-33555-8.

[74] E. M. WRIGHT, D. F. WALLS, and J. C. GARRISON. *Collapses and revivals of Bose-Einstein condensates formed in small atomic samples*. Phys. Rev. Lett. **77**, 2158–2161 (1996).

[75] E. M. WRIGHT, T. WONG, M. J. COLLETT, S. M. TAN, and D. F. WALLS. *Collapses and revivals in the interference between two Bose-Einstein condensates formed in small atomic samples*. Phys. Rev. A **56**, 591–602 (1997).

[76] M. LEWENSTEIN and L. YOU. *Quantum phase diffusion of a Bose-Einstein condensate*. Phys. Rev. Lett. **77**, 3489–3493 (1996).

[77] A. IMAMOĞLU, M. LEWENSTEIN, and L. YOU. *Inhibition of coherence in trapped Bose-Einstein condensates*. Phys. Rev. Lett. **78**, 2511–2514 (1997).

[78] Y. CASTIN and J. DALIBARD. *Relative phase of two Bose-Einstein condensates*. Phys. Rev. A **55**, 4330–4337 (1997).

[79] J. A. DUNNINGHAM, M. J. COLLETT, and D. F. WALLS. *Quantum state of a trapped bose-einstein condensate*. Phys. Lett. A **245**, 49–54 (1998).

[80] W. ZHANG and D. F. WALLS. *Bosonic-degeneracy-induced quantum correlation in a nonlinear atomic beam splitter*. Phys. Rev. A **52**, 4696–4703 (1995).

[81] M. GREINER, O. MANDEL, T. W. HÄNSCH, and I. BLOCH. *Collapse and revival of the matter wave field of a Bose-Einstein condensate*. Nature **419**, 51–54 (2002).

[82] P. W. SHOR. *Polynomial-time algorithms for prime factorization and discrete logarithms on a quantum computer*. SIAM J. Comp. **26**, 1484–1509 (1997).

[83] G. K. BRENNEN, C. M. CAVES, P. S. JESSEN, and I. H. DEUTSCH. *Quantum logic gates in optical lattices*. Phys. Rev. Lett. **82**, 1060–1063 (1999).
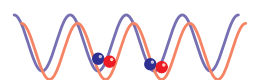
[84] H.-J. BRIEGEL, T. CALARCO, D. JAKSCH, J. I. CIRAC, and P. ZOLLER. *Quantum computing with neutral atoms*. J. Mod. Opt. **47**, 415–451 (2000).

[85] R. RAUSSENDORF and H. J. BRIEGEL. *A one-way quantum computer*. Phys. Rev. Lett. **86**, 5188–5191 (2001).

[86] G. K. BRENNEN, I. H. DEUTSCH, and C. J. WILLIAMS. *Quantum logic for trapped atoms via molecular hyperfine interactions*. Phys. Rev. A **65**, 022313–9 (2002).

[87] D. P. DIVINCENZO. *The physical implementation of quantum computation*. Fortschr. Phys. **48**, 771–783 (2000).

[88] D. A. LIDAR, I. L. CHUANG, and K. B. WHALEY. *Decoherence-free subspaces for quantum computation*. Phys. Rev. Lett. **81**, 2594–2597 (1998).

[89] R. SCHEUNEMANN, F. S. CATALIOTTI, T. W. HÄNSCH, and M. WEITZ. *Resolving and addressing atoms in individual sites of a CO_2-laser optical lattice*. Phys. Rev. A **62**, 051801–4 (2000).

[90] D. L. HAYCOCK, P. M. ALSING, I. H. DEUTSCH, J. GRONDALSKI, and P. S. JESSEN. *Mesoscopic quantum coherence in an optical lattice*. Phys. Rev. Lett. **85**, 3365–3368 (2000).

[91] N. F. RAMSEY. *Molecular Beams*. Oxford Univ. Pr., reprint edition (1990). ISBN 0-198-52021-2.

[92] E. L. HAHN. *Spin echos*. Phys. Rev. **80**, 580–594 (1950).

[93] D. JAKSCH. *Bose-Einstein Condensation and Applications*. PhD thesis, Leopold-Franzens-Universität Innsbruck (1999).

[94] V. A. KASHURNIKOV, N. V. PROKOF'EV, and B. V. SVISTUNOV. *Revealing the superfluid–Mott-insulator transition in an optical lattice*. Phys. Rev. A **66**, 031601–4 (2002).

[95] G. G. BATROUNI, V. ROUSSEAU, R. T. SCALETTAR, M. RIGOL, A. MURAMATSU, P. J. H. DENTENEER, and M. TROYER. *Mott domains of bosons confined on optical lattices*. Phys. Rev. Lett. **89**, 117203–4 (2002).

[96] W. DÜR, R. RAUSSENDORF, V. M. KENDON, and H.-J. BRIEGEL. *Quantum walks in optical lattices*. Phys. Rev. A **66**, 052319–8 (2002).

[97] D. STAUFFER and A. AHARONY. *Introduction to Percolation Theory*. Taylor & Francis Group, 2. edition (1992). ISBN 0-748-40027-3.

[98] W. HÄNSEL, J. REICHEL, P. HOMMELHOFF, and T. W. HÄNSCH. *Trapped-atom interferometer in a magnetic microtrap*. Phys. Rev. A **64**, 063607–6 (2001).

[99] D. A. STECK. *Rubidium 87 D line data*. Available online at http://steck.us/alkalidata/ (2003).

[100] D. R. LIDE, editor. *CRC Handbook of Chemistry and Physics*. CRC Press, Boca Raton, 85. edition (2000). ISBN 0-849-30485-7.

[101] M. P. BRADLEY, J. V. PORTO, S. RAINVILLE, J. K. THOMPSON, and D. E. PRITCHARD. *Penning trap measurements of the masses of ^{133}Cs, $^{87,85}Rb$, and ^{23}Na with uncertainties $\leq 0.2\,ppb$*. Phys. Rev. Lett. **83**, 4510–4513 (1999).

[102] E. ARIMONDO, M. INGUSCIO, and P. VIOLINO. *Experimental determinations of the hyperfine structure in the alkali atoms*. Rev. Mod. Phys. **49**, 31–75 (1977).

[103] J. YE, S. SCHWARTZ, P. JUNGNER, and J. L. HALL. *Hyperfine structure and absolute frequency of the $^{87}Rb\ 5P_{3/2}$ state*. Opt. Lett. **21**, 1280–1282 (1996).

[104] U. VOLZ and H. SCHMORANZER. *Precision lifetime measurements on alkali atoms and on helium by beam-gas-laser spectroscopy*. Physica Scripta **T65**, 48–56 (1996).

[105] J. L. ROBERTS, N. R. CLAUSSEN, J. P. BURKE, JR., C. H. GREENE, E. A. CORNELL, and C. E. WIEMAN. *Resonant magnetic field control of elastic scattering of cold ^{85}Rb*. Phys. Rev. Lett. **81**, 5109–5112 (1998).

[106] P. S. JULIENNE, F. H. MIES, E. TIESINGA, and C. J. WILLIAMS. *Collisional stability of double Bose condensates*. Phys. Rev. Lett. **78**, 1880–1883 (1997).

Index